DESIGNING AND ADVANCING CONTRAST AGENTS FOR ULTRASOUND-SWITCHABLE FLUORESCENCE IMAGING

By

YANG LIU

Presented to the Faculty of the Graduate School of

The University of Texas at Arlington in Partial Fulfillment

of the Requirements

for the Degree of

DOCTOR OF PHILOSOPHY

THE UNIVERSITY OF TEXAS AT ARLINGTON

December 2021

Abstract

DESIGNING AND ADVANCING CONTRAST AGENTS FOR ULTRASOUND-SWITCHABLE FLUORESCENCE IMAGING

Yang Liu, Ph.D.

The University of Texas at Arlington, 2021

Fluorescence imaging is a remarkable tool for molecular targeting and multicolor imaging, but it suffers from poor resolution in centimeters-deep tissues. The recently developed ultrasound-switchable fluorescence (USF) imaging has overcome this challenge and achieved *in vivo* imaging with the help of the indocyanine green (ICG)-encapsulated poly(N-isopropylacrylamide) (ICG-PNIPAM) contrast agent. As USF imaging advances, there is a great demand to expand the contrast agent bank so that applications can be achieved using different types of contrast agents. Also, there is a need to improve the current ICG-PNIPAM nanogel.

This study focused on improving the ICG-PNIPAM nanogel, formulating a novel contrast agent, and exploring dual-modality imaging. First, we controlled the size of the ICG-PNIPAM nanogel by adjusting the quantity of sodium dodecyl sulfate (SDS), and we successfully synthesized an ICG-PNIPAM nanogel from 55.6 nm to 515.1 nm. The ICG-PNIPAM nanogel in different sizes showed great stability and switching repeatability. Further *in vivo* USF imaging demonstrated that different-sized nanogel accumulated in organs such as the spleen and liver. We achieved both *ex vivo* and *in vivo* computed

tomography (CT) and USF dual-modality imaging with the gold nanoparticles and ICG-loaded PNIPAM nanogel.

A novel ICG-loaded liposomal microparticle was first formulated for USF imaging. Compared with ICG-PNIPAM nanogel, ICG-liposome had a narrow fully switched-ON temperature range, a near-infrared (NIR) emission peak at 836 nm, and great biocompatibility. Both *ex vivo* and *in vivo* USF imaging were successfully conducted and proved that ICG-liposome was another excellent USF contrast agent. Further, the bi-layer lipid membrane was constructed with additional lipid that had pegylated chains and folate targeting groups associated. The size of the liposome was reduced and controlled from 82.3 nm to 162.4 nm. A high increase in fluorescence intensity and a switch-ON temperature closer to body temperature were observed. In addition, the ICG-liposome nanoparticles had a high encapsulation efficiency of more than 80 % and a release efficiency of up to 48.01 % when assisted with ultrasound. A potential USF imaging-guided and ultrasound-assisted drug delivery application can be achieved.

In conclusion, this study not only improved the existing ICG-PNIPAM nanogel with size control but also formulated novel liposomal microparticles and nanoparticles for both *ex vivo* and *in vivo* USF imaging. In addition, we achieved CT and USF dual-modality imaging with gold nanoparticle (AuNP) and ICG-loaded PNIPAM nanogel. We strongly believe that with the improvements and innovations accomplished in this study, USF imaging will become a valuable tool in the field of biomedical imaging.

Acknowledgements

I would like to thank my supervisor, Dr. Baohong Yuan, for his mentorship and support during my Ph.D. study at the University of Texas at Arlington. He advised me not only on research projects but also on my future career path. I deeply thank him for offering me the opportunity to work in the biomedical engineering field and explore medical imaging research. I have learned a lot from him in imaging theories, instrumentation, and a positive research attitude. Thanks for introducing me to the ultrasound-switchable fluorescence imaging study. I was amazed by the potential of this technology for centimeter-deep tissue imaging. I want to thank him for providing an amazing platform for me to explore contrast agents, animal models, and imaging instruments. Thanks again for helping me become a successful researcher and person.

I would also like to extend my thanks to Dr. Kytai Truong Nguyen, Dr. Yi Hong, Dr. Hanli Liu, and Dr. Georgios Alexandrakis. Thanks for your support, insightful criticism, and suggestions during my professional development. I would like to individually thank Dr. Nguyen for allowing me to work in her lab for cell culturing and collaboration work with her students. Also, I want to thank Dr. Nguyen for her generous suggestions and support in my future career development. Also, I want to thank Dr. Hong for allowing me to conduct chemical synthesis in his lab and for his professional comments and suggestions on my published manuscripts. I would like to thank Dr. Liu for teaching me about the medical imaging process and helping me to better understand medical images. To Dr. Alexandrakis, thanks for teaching me basic principles of medical imaging and helping me build fundamental knowledge in the biomedical imaging field.

I am very grateful to work with my colleagues during my Ph.D. study. Dr. Shuai Yu and Dr. Tingfeng Yao helped me a lot with imaging instruments and imaging processing. I want to thank them both for training me and working with me to advance the ultrasound-switchable fluorescence imaging technology. I also want to thank Dr. Ruilin Liu and Dr. Wenbin Cai for supporting me in chemical synthesis and particle formulation. Also, I would like to thank Ms. Liqin Ren, as it has been a great pleasure to work with , and I am grateful for her support during my study.

I also want to thank Dr. Jayanth Kandukuri, Dr. Bahar Saremi, Dr. Cancan Xu, Dr. Qionghua Shen, Dr. Duong Le, Mr. Tam Phung Nguyen, Mr. Uday Kumar Chintapula, and Mr. Huikang Fu for their contributions and support during my Ph.D. study.

Last, I would like to thank my beloved spouse, Mrs. Chengyue Bu, and my parents, Mr. Tao Liu and Mrs. Jiangli Lang. Without your support and encouragement, I could hardly have made it this far in my education. I will always be grateful for the sacrifices you made and the suggestions you gave. It means a lot to me to go through all the challenges and successes of my Ph.D. study as a family. I feel so lucky to have all of you beside me, and I look forward to the next stage of my life with you.

This work was supported in part by funding from the CPRIT RP170564 (PI: Baohong Yuan) and the NIH/NIBIB 1R15EB030809-01 (PI: Bahong Yuan).

Table of Contents

List of Figures

List of Tables

Abbreviations

AAm: Acrylamide

ACA: 4-4’-Azobis(4-cyanopentanoic acid)

AIBN: Azobisisobutyronitrile

AuNP: Gold nanoparticle

BIS: N,N’-methylenebisacrylamide

CT: Computed tomography

DI: Deionized

DLS: dynamic light scattering

DMEM: Dulbecco's modified eagle's medium

DMSO: Dimethyl sulfoxide

EPR: Enhanced permeability and retention

FBS: Fetal bovine serum

FDA: Food and Drug Administration

HIFU: High intensity focused ultrasound

ICG: Indocyanine green

IV: Intravenous

LNPs: Liposome nanoparticles

MI: Mechanical index

NIPAM: N-Isopropylacrylamide

NIR: Near-infrared

PALS: Phase analysis light scattering

PDI: Polydispersity index

PNIPAM: Poly(N-isopropylacrylamide)

SA: Sodium ascorbate

SDS: Sodium dodecyl sulfate

SNR: Signal to noise ratio

TBAm: N-tert-butylacrylamide

TEM: Transmission electron microscopy

USF: Ultrasound-switchable fluorescence

β-CD: Beta-cyclodextrin

Chapter 1

Introduction and Background

Biomedical imaging helps diagnose diseases, track lesion cell progression, and study the cell structure and interaction between cells. They are important tools in both biomedical research and clinical applications. For example, researchers used molecular fluorescence imaging to target and track molecule movement inside the body to study cell uptake activity [1]. In addition, biomedical imaging helps with surgery and imaging-guided drug delivery applications [2–4].

1. Fluorescence Imaging

1.1 Principle

Fluorescence imaging has advanced dramatically in recent years. It has been widely used for functional imaging and colorful imaging to better differentiate structures. During fluorescence imaging (shown in Figure 1), we implemented an excitation light source at a specific wavelength to illuminate and excite fluorophores or contrast agents in a region of interest. The light was absorbed and an emitting light with a longer wavelength, and lower energy was generated. This emission light passed through filters to filter out excitation light and other noise before reaching the detector. Then, the signal was transformed into an electric signal and finally processed to form the fluorescence image. Fluorescence can be used to study cell activities, identify lesions, and monitor tumors. Due to its unique light-related image, a colorful image with labels of structures can be obtained. Recently, the assistance of fluorescence imaging in surgery has been widely applied to identify lesions and tumors. Fluorescence imaging can outline a clear boundary between normal tissue and

a lesion, allowing tissue damage to be minimized and unwanted tissues to be removed efficiently [5–7]. However, conventional fluorescence imaging suffers from poor resolution in centimeter-deep tissues due to light scattering caused by tissue.

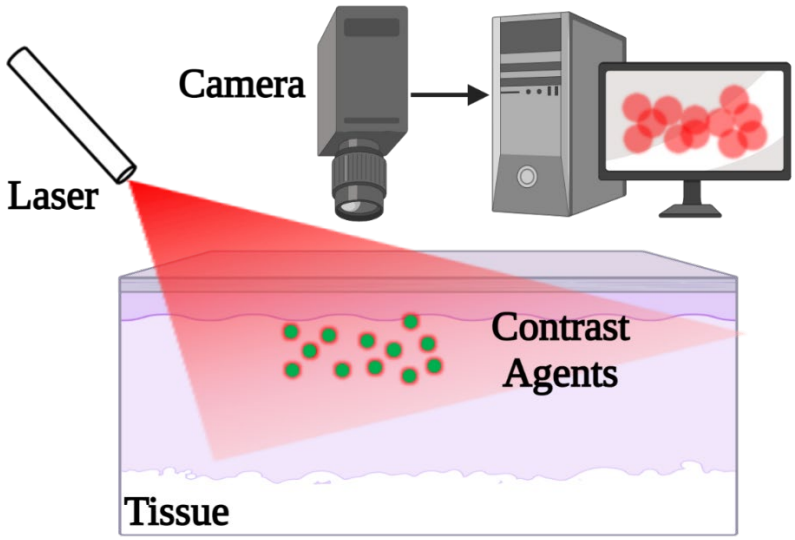

Figure 1. A fluorescence imaging diagram with contrast agents embedded in tissue. A laser light source was used to excite the contrast agent, and a camera was used to collect the emitted fluorescence light, which was finally processed on a computer to acquire the fluorescence image.

1.2 Contrast Agents

For conventional fluorescence microscopic technologies, fluorescent dyes, which are used in fluorescence imaging, range from visible to near-infrared (NIR) wavelengths. Visible dyes were applied for cell fluorescence imaging labeling, such as cyanine and ATTO series dyes. For relatively deep tissue imaging, NIR-I dyes, such as indocyanine green (ICG), were used. NIR-II dyes (~1000 – 1700 nm) can be used for microscopic imaging in even

deeper tissue because light scattering is significantly reduced. However, tissue absorption becomes high, which limits the imaging depth.

Except for fluorescent small molecules, fluorophores encapsulated or attached to particles were also formulated and used in fluorescence imaging. After modifying the composition and surface of particles, they can be used for active targeting [8], extending *in vivo* circulation time [9] and responding to the surrounding environment such as pH, temperature, and pressure [10–12]. Contrast agents formulated with various materials were also implemented, such as polymers, metals, and lipids. Different materials were designed for fluorescence imaging requests. For example, polymer-based contrast agents have outstanding structural stability and are suitable for long-term fluorescence imaging applications. Lipid-based contrast agents are usually biocompatible and suitable for *in vivo* fluorescence imaging.

1.3 Centimeter-deep Tissue Fluorescence Imaging

Tissue fluorescence imaging at a depth of a few centimeters is usually conducted with NIR-I and NIR-II dyes due to less tissue absorption and scattering, which can result in high spatial resolution in millimeters or centimeters of deep tissue. A recent study using an aggregation-induced emission fluorescence probe was reported to break the fluorescence imaging depth limitation of millimeter-deep tissue and achieve 1.5 cm of deep vascular imaging in the NIR-II range [13]. In addition, a Mn^{5+}-doped barium phosphate contrast agent showed not only fluorescence imaging capability in deep tissue but also had a temperature sensitive fluorescence peak, which decreases as temperature increases, in the

NIR-II window [14]. Because of these distinguishing characteristics, this contrast agent was able to achieve a 2.8 cm depth of tissue fluorescence imaging and potential temperature monitoring in deep tissue. A core/shell nanoparticle was developed in Chen's lab to achieve fluorescence imaging at 3.5 cm with a cuvette/tissue model [15]. A recent tissue phantom study also reported the fluorescence imaging of 1 mm particles at a depth of 8 cm with the Detection of Optically Luminescent Probes using Hyperspectral and diffuse Imaging in Near-infrared (DOLPHIN) imaging system [16].

2. Ultrasound-Switchable Fluorescence Imaging

2.1 Principle

Fluorescence imaging is a remarkable biomedical imaging tool. However, it suffers from poor resolution in centimeters-deep imaging due to light scattering in tissue. The ultrasound-switchable fluorescence (USF) imaging developed in our lab showed great potential to resolve the issue mentioned above (Figure 2). During USF imaging, a focused ultrasound beam scans through the imaging area and induces thermal energy to cause a temperature increase at the beam focus. Thermal-sensitive contrast agents shrink while the surrounding temperature rises. When the temperature reaches the lower critical solution temperature (LCST) point, contrast agents are switched "ON" and the emitted fluorescence intensity surges. Because the increase in fluorescence intensity is confined within the ultrasound focal volume, the spatial resolution of the USF imaging depends on the size of the thermal focal zone. In addition, because the increase in the fluorescence intensity comes only from contrast agents, the signal received can be easily differentiated from background noise so that the signal-to-noise ratio (SNR) and the sensitivity are refined.

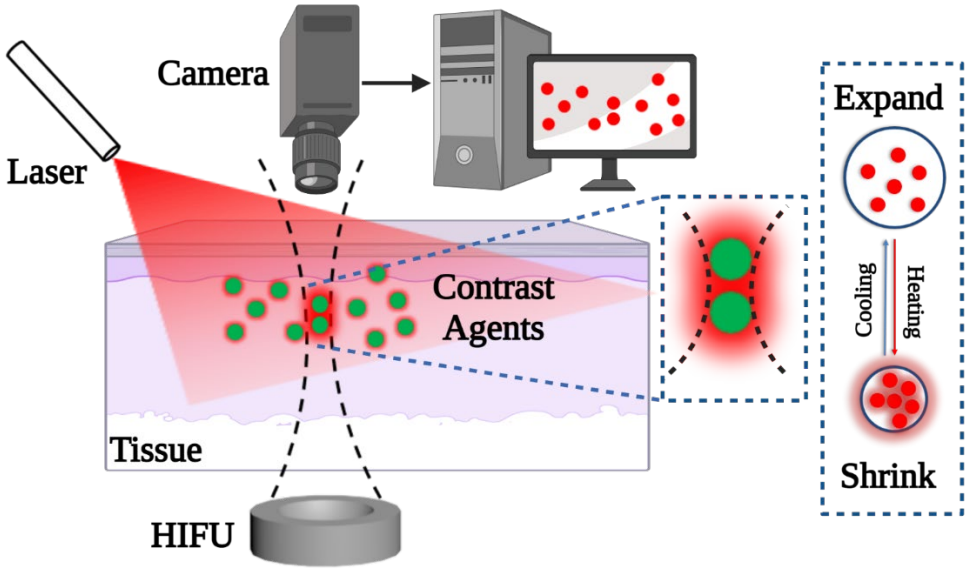

Figure 2. USF imaging system diagram. A laser was used to excite contrast agents. High intensity focused ultrasound (HIFU) transducer is used to heat up the region of interest and only contrast agents within the region emit stronger fluorescence light due to the size reduction of the contrast agents. A camera was used to collect emitted fluorescence light, and a computer was used to process the data and acquire the USF image.

2.2 Current Available USF Contrast Agents

As a temperature-sensitive USF imaging contrast agent, it should be flexible enough and can contract while the temperature increases and expand while the temperature decreases. The structure of the contrast agent should be stable enough during contracting and expanding to avoid destruction. In addition, the structure of the contrast agent needs to be intact when exposed to temperature increases and ultrasound mechanical force. We developed Pluronic micelle, which has a single layer membrane and fluorescence dyes encapsulated, for USF imaging. As the temperature increases, we observed a fluorescence

intensity fold change of more than 200 in a phantom model [17]. Two dyes, aza-BODIPY and zinc phthalocyanine, were encapsulated in Pluronic micelles made from F127, F98, F68, or F38 and characterized in fluorescence intensity and lifetime change with respect to the change of temperature [18]. We used a tube model to compare USF imaging of different combinations of dyes and micelles. However, after mixing Pluronic micelle with mouse blood, the fluorescence intensity would not increase while the temperature increased, and thus it cannot be used for USF imaging. Therefore, the protocol needs to be modified to stabilize the related particles for USF imaging in live tissue environments.

Another USF imaging contrast agent, poly (N-isopropylacrylamide) (PNIPAM) nanogel, exhibits exceptional stability for both storage and *in vivo* application. The first-generation PNIPAM nanogel was reported by Pei and showed great temperature responsiveness with change of fluorescence intensity, adjustable switch-ON temperature, and outstanding switching repeatability [19]. Improvements were made with the second-generation PNIPAM nanogel to extend the shelf life and reported a storage of 245 days while still being good to use for USF imaging [20]. We used a phantom model to prove and characterize the capability of PNIPAM nanogel for USF imaging. Later, the first-time *in vivo* USF imaging was conducted with the second-generation PNIPAM nanogel and the results showed an accumulation in the spleen [21]. To broaden the *in vivo* application of PNIPAM nanogel, there was a great demand to control its size and perform targeted USF imaging on different organs and tumors. Although PNIPAM nanogel achieved successful *in vivo* USF imaging, the cytotoxicity was a drawback [22].

2.3 Criteria to Evaluate USF Contrast Agents

A thorough characterization of the USF contrast agent was essential to assess the capability and features for USF imaging. First, understanding the background fluorescence intensity of a USF contrast agent is vital. A lower background fluorescence intensity was desired to achieve a high SNR. Second, a high fluorescence intensity increase after being fully switched ON at the region of interest is preferred to give a high USF signal. High fluorescence intensity increases, particularly in centimeter-deep tissue, can help not only detect the USF signal but also obtain a high SNR USF image. The switch-ON point with a temperature slightly above body temperature is wanted for *in vivo* USF imaging. It is ideal that after introducing contrast agents, they stay in an OFF state to minimize background noise. During USF imaging, contrast agents can be easily switched ON without causing high temperature increases to prevent tissue damage. Similarly, the temperature required to fully activate contrast agents should be kept as low as possible to avoid tissue damage. In addition, low heat and ultrasound power can reduce the damage to the contrast agent itself, preventing structure collapse. As mentioned previously, NIR dyes were favored for deep-tissue fluorescence imaging to avoid light absorption and scattering caused by tissue. Therefore, dyes with emission peaks in regions of NIR-I and NIR-II were desired. Another criterion to consider is the stability of the contrast agent, which includes shelf-life time, biostability, and storage conditions. Evaluation of circulation time, targeting or accumulating efficiency, and biocompatibility should be performed for *in vivo* USF imaging.

3. Specific Aims

The goals of this study are to improve the existing PNIPAM-based contrast agent for organs/tumor imaging through size control, as well as to develop novel liposome-based contrast agents for *in vivo* USF imaging and ultrasound assisted release. In addition, we conducted synthesis and characterization of gold nanoparticles and ICG-encapsulated PNIAPM nanogel for dual-modality imaging via computed tomography (CT) and USF.

The long-term goal of this study is to improve the performance of current USF contrast agents and develop new contrast agents for USF imaging while advancing *in vivo* USF imaging and exploring other potential applications.

To attain the objective and achieve the long-term goal, we researched the following specific aims.

3.1 Aim 1: Achieve Size-Control of ICG-PNIPAM Nanogels for USF Imaging of Different Organs and Tumors.

Current ICG-PNIPAM nanogels mainly accumulate in the spleen of mice. With the ability to change the size of ICG-PNIPAM nanogels, they have the potential to accumulate in organs or tumors. To achieve the goal, we adjusted the concentration of sodium dodecyl sulfate (SDS), an anionic surfactant, during synthesis and measured the size of ICG-PNIPAM nanogels. We imaged the metabolic pathway of PNIPAM nanogel with different sizes and conducted USF imaging on organs and tumors.

3.2 Aim 2: Synthesize 1st Generation of Liposome Microparticles for Biocompatible and Near-infrared USF Imaging.

This aim synthesized liposomes with ICG dye encapsulated, and we studied the capability for USF imaging. We evaluated the change in fluorescence intensity with respect to the change of temperature using a home-built cuvette system. We used a spectrometer to measure the spectrum and determined the cytotoxicity using a 3-(4,5-dimethylthiazol-2-yl)-2,5-diphenyltetrazolium bromide (MTT) assay. We conducted USF imaging in a tube model, tissue model, *ex vivo*, and *in vivo*.

3.3 Aim 3: 2nd Generation of Liposome Nanoparticles Decorated with PEGylated Chains and Folate Targeting Groups for USF Imaging and Ultrasound Assisted Release.

We controlled the size of liposomes via an extrusion method and used lipids such as DSPE-PEG2000-folate and DPPC to form a bi-layer membrane. The synthesized liposomes had PEGylated chains on the surface to improve their *in vivo* stability. Folate groups at the end of PEGylated chains had the potential to target folate receptors on the surface of tumor cells. We evaluated the USF imaging capability for various sizes of liposomes and conducted a depth-study in a phantom model. We evaluated the loading efficiency of ICG dyes and conducted an ultrasound-assisted release to assess the release efficiency of liposomes.

3.4 Aim 4: Gold Nanoparticles and ICG-loaded PNIPAM Nanogel for CT and USF Dual-modality Imaging.

We followed the Turkevich method to synthesize a gold nanoparticle (AuNP) solution and then concentrated the AuNP solution. The AuNPs and ICG-loaded PNIPAM nanogel were then synthesized and characterized. We conducted e*x vivo* CT and USF imaging, followed by a local injection of nanogel at the thigh in mice. Because AuNPs were loaded into the PNIPAM nanogel, CT and USF images can be co-registered and compared.

Chapter 2

Size-Control of ICG-PNIPAM Nanogels for USF Imaging

1. Introduction

Recently, our lab developed a technology, USF imaging, to overcome the poor resolution issue when imaging in centimeters-deep tissue via fluorescence [23]. A short ultrasound pulse is applied to heat the region of interest and only contrast agent within this region is switched ON, while surrounding contrast agents remain in OFF status. The switched-ON contrast agents provide USF signals. The spatial resolution of USF depends on the size of ultrasound focus (both lateral and axial focal sizes) and is independent of the imaging depth. PNIPAM-based nanogel has a history of being used as one of the contrast agents for USF. The first-generation of PNIPAM nanogel was developed to show its feasibility as a USF contrast agent [19]. In addition, the switch-ON threshold was proven to be adjustable by changing the quantity of hydrophilic monomers acrylamide (AAm) or hydrophobic monomer of N-tert-butylacrylamide (TBAm). This feature is important for future *ex vivo* and *in vivo* experiments. However, it has some limitations, such as short shelf life. The second-generation of PNIPAM nanogel was then developed by Yu with an improved storage stability of more than 6 months [20]. Later, a milestone was reached using the second-generation of PNIPAM nanogel for both *ex vivo* and *in vivo* experiments [21]. The results showed that most of PNIPAM nanogels accumulate in spleen after 3 hours of circulation, and USF imaging was successfully conducted to show the *in vivo* imaging capability. Furthermore, USF imaging of a breast tumor with a local injected PNIPAM nanogel was conducted and proved the USF imaging capability of PNIPAM nanogel in a tumor micro-environment. Nevertheless, previous studies lack detailed physiological

characterization of the PNIPAM nanogel. Also, it is vital to explore USF imaging with various sizes of PNIPAM nanogel because different applications might require different-sized PNIPAM nanogels.

This study conducted a detailed physiological characterization of the PNIPAM nanogel. We measured the hydrodynamic size via dynamic light scattering (DLS) and verified the physical size and shape using transmission electron microscopy (TEM). We also studied the effect of the physiological environment on the performance of PNIPAM nanogel. In addition, we controlled the size of the PNIPAM nanogel from 55 nm to 500 nm by adjusting the quantity of SDS used during synthesis. We analyzed the effect of size on the PNIPAM nanogel using a fluorescence intensity profile. We then applied various sizes of PNIPAM nanogel for different applications, such as *in vivo* USF imaging of the liver and cancer.

2. Materials and Methods

2.1 PNIPAM Nanogel Synthesis

Synthesis of the PNIPAM nanoparticle followed a previous published method with modifications [20]. 1.166 g of N-Isopropylacrylamide (NIPAM) (monomer, 97 %), 0.118 g of AAm (adjust LCST, ⩾99 %), and 12.05 mg of N, N'-methylenebisacrylamide (BIS) (cross-linker, ⩾99.5 %) were dissolved with 45 mL of deionized (DI) water in a Schleck reaction tube. Various amounts (10 mg, 20 mg, 40 mg, 100 mg, 200 mg, and 300 mg) of SDS (surfactant, ⩾98.5 %) were added to the tube to synthesize different sizes of nanoparticles. The mixture was purged with nitrogen (99 %, Airgas, USA) for 1 hr with stirring at 450 rpm. Then, the ICG (3.54 mg) was quickly poured into the tube, and a rubber

stopper was used to seal the tube. A vacuum/purge cycle was conducted five times to ensure a nitrogen environment. The sample was first vacuumed for 2 minutes with stirring and then purged with nitrogen. Next, the reaction tube was placed into an oil bath, which had a temperature of 70 ˚C, and was heated with stirring for 30 min. The 4-4'-Azobis(4-cyanopentanoic acid) (ACA) solution, which was prepared by dissolving 70 mg of ACA (initiator, ⩾98 %) into 5 mL of water (pH 10.5), was injected into the reaction tube. The reaction was reacted for 19 hours at 70 ˚C with a stirring speed of 400 rpm. The obtained PNIPAM nanoparticle solution was then dialyzed with a dialysis tube (10 kDa, Spectrum Chemical Mfg. Corp., USA) for 3 days. PNIPAM nanogel samples are identified using the format: PNIPAM-XmgSDS. "X" represents the quantity of SDS. For example, PNIPAM nanogel synthesized with 20 mg SDS is identified as PNIPAM-20mgSDS. Freeze-drying was followed and the desired concentration of PNIPAM was prepared. Samples were stored at 4 ˚C in dark. All chemicals were purchased from Sigma-Aldrich.

2.2 Size Characterization and Zeta Potential Measurement

The DLS (NanoBrook 90PlusPALS, Brookhaven Instruments, USA) was utilized to measure the median hydrodynamic size of PNIPAM nanoparticles. The PNIPAM solution was diluted 30 times with DI water in a 3.5 mL quartz cuvette to avoid aggregation before measuring. The measurements were conducted at room temperature and repeated at least three times.

The zeta potential of PNIPAM nanogel was measured by diluting the nanogel 30 times with DI water and loading it into a 3.5 mL gold electrode cuvette. Then, the phase analysis

light scattering (PALS) (NanoBrook 90Plus PALS, Brookhaven Instruments, USA) was used to conduct zeta potential measurements at room temperature. Each measurement was repeated five times.

TEM (H-9500, Hitachi, Japan) was used to measure the physical size and visualize the shape of PNIPAM nanogel. First, the PNIPAM nanogel was diluted 50 times to avoid aggregation during imaging. A 200-mesh copper grid was fixed using forceps. A 10 μL PNIPAM nanogel was dropped on the grid and left overnight to allow complete solvent evaporation. Then, 10 μL of 0.5 % uranyl acetate was dropped on the grid to negatively stain the sample. After 10 minutes, the sample was placed in the TEM for imaging.

2.3 Spectrum

The excitation and emission spectra of PNIPAM nanogel were characterized using a spectrometer (Fluoromax-Plus-C, Horiba, Japan). PNIPAM nanogel was diluted 10 times to avoid saturation. A 300 μL quartz cuvette (Hellma, Germany) was used to hold a 200 μL PNIPAM sample. The cuvette was placed inside a holder with stirring and temperature control at 25 ˚C. The emission spectrum was scanned from 575 nm to 850 nm using an excitation light of 500 nm. A 550 nm long-pass filter (Semrock, USA) was used to avoid leakage of excitation light. Also, the excitation spectrum was scanned from 500 nm to 800 nm.

2.4 Fluorescence Intensity Study and Switch-ON/OFF Tests

An in-house built cuvette system was applied to examine the fluorescence intensity profile, which was the relationship between the fluorescence intensity emitted from the PNIPAM nanogel with respect to the change in temperature. A 3 mL PNIPAM nanogel solution was loaded into a 3.5 mL quartz cuvette and placed in a temperature-controlled holder (Quantum Northwest, Inc., USA) with a stir. An 808 nm excitation laser (MGL-II-808-2W, Dragon lasers, China) was used to excite the sample. The emitted light from PNIPAM nanogel passed through an 830 long-pass filter (Semrock, USA) before being collected by a modular USB spectrometer (USB2000+, Ocean Inlight, USA). The temperature measurement ranges from 30 ˚C to 55 ˚C with an increment of 0.1 ˚C. A temperature probe was inserted into the cuvette to monitor the sample temperature. The fluorescence intensity at various temperature points was recorded.

The switch-ON/OFF test was conducted using the same in-house built cuvette system. Briefly, after loading the sample into the cuvette, the temperature controller was set at 30 ˚C. When the sample temperature reached the targeting point, the fluorescence intensity for switch OFF was recorded. Then, the temperature was quickly raised to 55 ˚C to fully switch ON the PNIPAM nanogel. The fluorescence intensity was recorded after reaching the targeting point. A total of five cycles of switching ON/OFF were conducted to test the stability of PNIPAM nanogel.

2.5 Stability Tests in Physiology Mimicked Environment

Before conducting *ex vivo* and *in vivo* experiments, it is necessary to verify if the PNIPAM nanogel is stable when exposed to different physiological environments. To simulate the

in vivo microenvironment with different pH values and protein contentions, solutions with different pH values (5.39, 6.18, 7.40, and 9.60) and bovine serum albumin (BSA) concentrations (0, 3, 6, 10, 20 mg/mL) were used. The previously mentioned in-house built cuvette system was used, and PNIPAM nanogel was mixed with different solutions (1:10 v/v) to examine the change in fluorescence intensity profile.

2.6 Cell Culture and Tumor Model

Two cancer cell lines were cultured, which included the brain cancer cell (U87, ATCC, USA) and pancreatic cancer cell (BxPC-3, ATCC, USA). Both cell lines were cultured in Dulbecco's modified eagle's medium (DMEM, ATCC, USA). After the cell concentration reached 3×10^6 cells/mL, 100 µL of cancer cells were injected into each nude mouse (NU/J, female, Jackson Laboratory) subcutaneously at the thigh to construct the tumor model. See Appendix A for detailed cell culture procedures.

2.7 In vivo USF Imaging Using Various-sized PNIPAM Nanogel

Various-sized PNIPAM nanogels were injected into mouse models (BALB/c mouse, female, 7 weeks) via an intravenous (IV) injection. The detailed USF *in vivo* imaging methods were described in published articles by Yu and Yao [21,24]. A 3-dimentional scan was conducted on either the spleen or liver after confirming the accumulation peak time of PNIPAM nanogel at a certain organ.

3. Results

3.1 Size, Zeta Potential, and Spectrum

As shown in Figure 3, the sizes of PNIPAM nanogels synthesized with various amounts of SDS were characterized and summarized in Figure 3. As shown in Figure 3a, the hydrodynamic size of PNIPAM decreased as the quantity of SDS increased. The insert figures were TEM images acquired of PNIPAM nanogels synthesized using 20, 40, 100, and 200 mg of SDS. It is clear to state that the hydrodynamic size range of PNIPAM is from 55.6 nm to 515.1 nm. The table below summarizes the detailed hydrodynamic size with respect to the quantity of SDS and polydispersity index (PDI) for different-sized PNIPAM nanogels. The PDI measures the heterogeneity of a sample based on size. A particle solution, such as lipid-based carriers, with a PDI < 0.3 was considered acceptable in drug delivery applications [25]. The TEM images of PNIPAM nanogels synthesized with 20, 40, 100, and 200 mg SDS were displayed in Figure 3b. The particle size of PNIPAM-20mgSDS has a heterogeneous size distribution as shown in the figure, and PNIPAM-100mgSDS has a more homogeneous size distribution. Furthermore, the majority of the PNIPAM nanogel was confirmed to be round, while a minor amount of PNIPAM nanogel was shown to be ellipse.

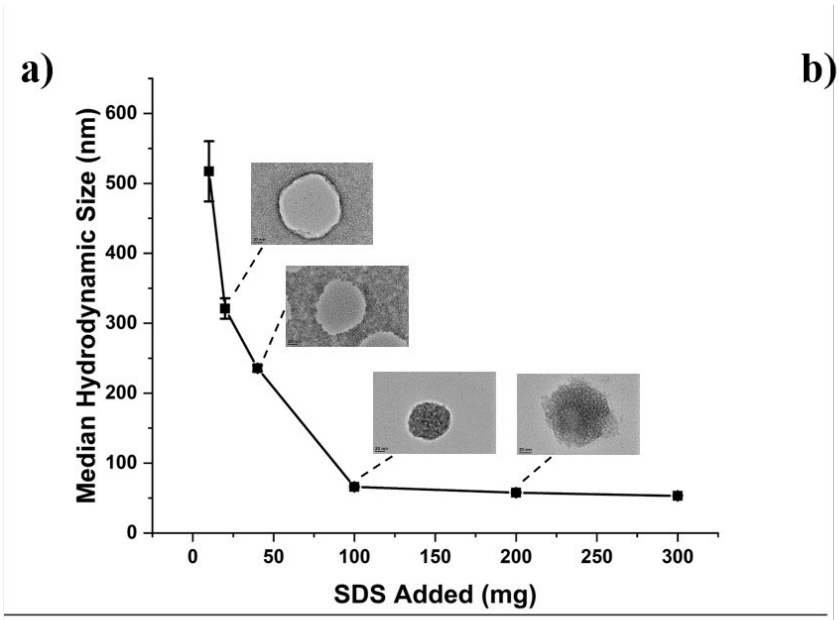

SDS Quantity (mg)	10	20	40	100	200	300
Hydrodynamic Size (nm)	515.1	335.1	235.1	66.1	58.0	55.6
Standard Deviation (nm)	268.3	188.8	54.9	34.8	28.0	30.3
Polydispersity Index	0.319	0.370	0.068	0.326	0.277	0.347

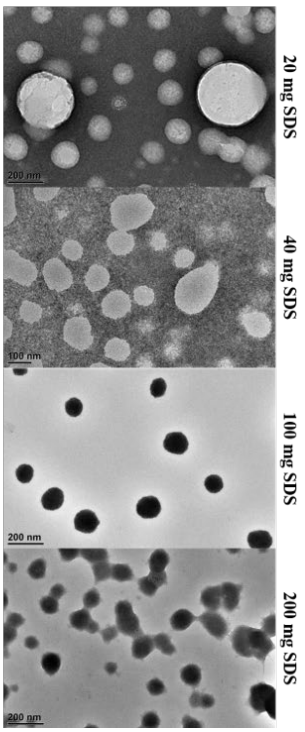

Figure 3. Size characterization of PNIPAM nanogel. a) Correlation between hydrodynamic size of PNIPAM nanogel and the quantity of SDS. Detailed information on hydrodynamic size, standard deviation of hydrodynamic size, and polydispersity of PNIPAM nanogel synthesized with various SDS quantities were summarized in the table. The number of replicates is n > 3. Insert figures represent the TEM images of a single PNIPAM nanogel synthesized with 20, 40, 100, and 200 mg of SDS. b) TEM images of PNIPAM nanogels synthesized with 20, 40, 100, and 200 mg of SDS.

Figure 4a summarizes the zeta potential of PNIPAM gels synthesized with 20, 40, 100, and 200 mg of SDS as 6.98 ± 1.34, -1.14 ± 0.84, -1.51 ± 0.67, and -3.53 ± 1.02 mV, respectively. The net charge of the PNIPAM nanogel was slightly affected by the SDS quantity. As the amount of SDS increased, the PNIPAM nanogel tended to be more negatively charged or

neutral. Figure 4b and 2c shows the excitation spectra and emission spectrum, respectively. The excitation peak of PNIPAM nanogel was at 671 nm with a detection peak at 850 nm. The emission peak of PNIPAM nanogel was at 605 nm measured with a 500 nm excitation light. The size of PNIPAM nanogel has seldom impact on the emission spectra. On the other hand, the excitation spectra of PNIPAM nanogel with larger size (e.g. 200 - 300 nm) had a broader excitation spectra peak from 671 nm to around 725 nm compared to the excitation spectra of PNIPAM nanogel in smaller size (e.g. 50 - 70 nm).

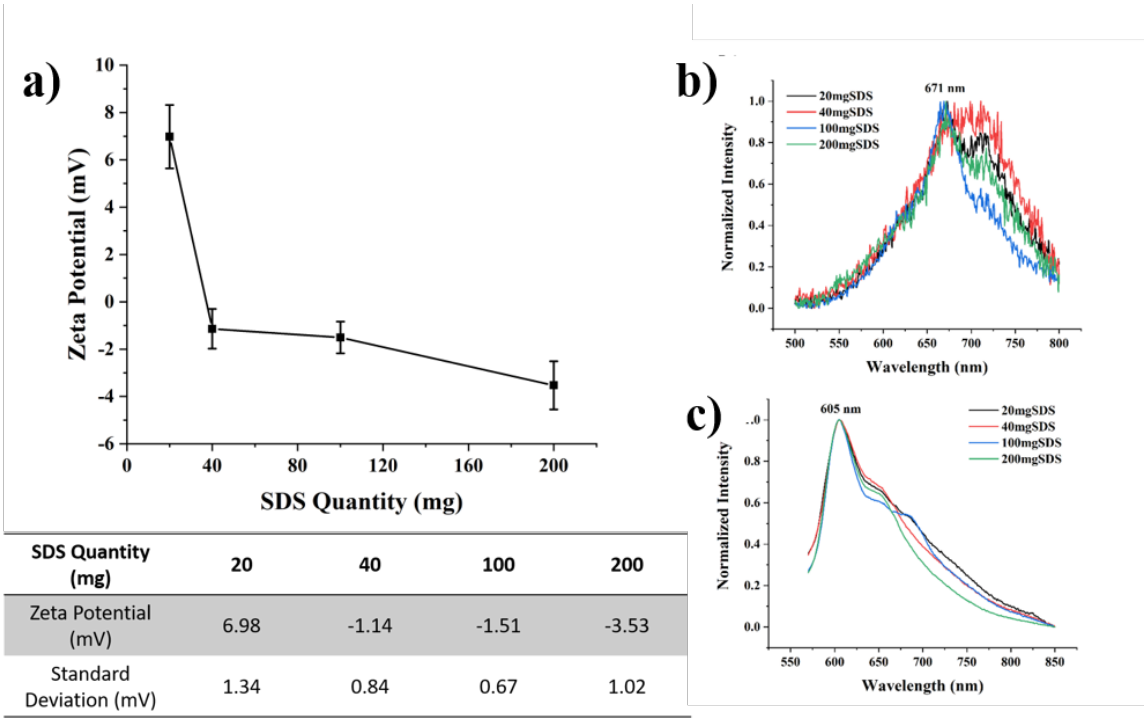

SDS Quantity (mg)	20	40	100	200
Zeta Potential (mV)	6.98	-1.14	-1.51	-3.53
Standard Deviation (mV)	1.34	0.84	0.67	1.02

Figure 4. a) Summary of zeta potential measurements for PNIPAM nanogels synthesized with different quantities of SDS. The number of replicas was n = 3. Normalized b) excitation and c) emission spectra of PNIPAM nanogel synthesized with various amounts of SDS. An excitation laser of 500 nm was used to measure the emission spectra, and emission light of 850 nm was used to determine the excitation spectra.

3.2 Fluorescence Intensity Profile

The relationship between the fluorescence intensity and temperature, or fluorescence profile, of PNIPAM nanogel in various sizes was studied, and the results are shown in Figure 5a. The normalized data was summarized in Figure 5b, and the table below analyzed key factors of the PNIPAM nanogel as a USF contrast agent. First, we can easily conclude that the fluorescence intensity increased while the temperature increased and the size of the PNIPAM nanogel affected the fluorescence profile. PNIPAM-100mgSDS had the highest background fluorescence intensity, and PNIPAM-40mgSDS had the lowest background fluorescence intensity. There was no clear trend in background fluorescence intensity with respect to the size. Furthermore, for the PNIPAM-200mgSDS sample, the fluorescence intensity increased by 74.1 % after fully switching ON. According to Figure 5b, we can see that the switch-ON temperature shifted to the right when the quantity of SDS increased. PNIPAM-100mgSDS and PNIPAM-200mgSDS were favored for *in vivo* applications because the switch-ON temperature points were above and close to body temperature. Therefore, after being introduced into the body, the PNIPAM nanogel was fully switched OFF and can be easily switched ON during USF imaging. Also, the PNIPAM nanogel size did not have an obvious impact on the temperature range of fully switching ON the PNIPAM nanogel.

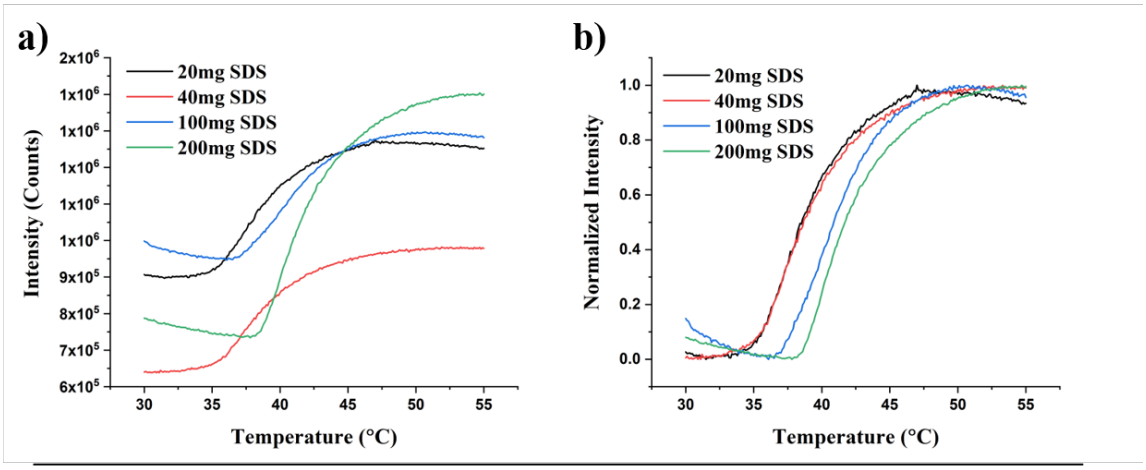

SDS Quantity (mg)	20	40	100	200
Background fluorescence (Counts)	906,770	640,100	998,440	787,780
Fluorescence increase (Counts/%)	342,380/37.8	316,040/49.4	285,060/28.6	583,920/74.1
Switch ON temperature (˚C)	34.9	34.7	36.5	38.2
Fully Switch ON temperature range (˚C)	11.0	11.4	11.5	11.8

Figure 5. a) The correlation between fluorescence intensity and temperature for ICG-PNIPAM nanogels synthesized with various quantity of SDS. b) Normalized data. Detailed comparison was summarized in the table, including the background fluorescence intensity, the fluorescence intensity increase after fully switching ON the PNIPAM nanogel, the switch-ON temperature point, and the fully switched ON temperature range.

3.3 Switch-ON/OFF Test and Physiological Stability

Two stability tests were conducted to examine the performance stability and *in vivo* stability of the PNIPAM nanogel. Figure 6a, b, c, and d show the results of the switch-ON/OFF test for PNIPAM nanogel synthesized with 20, 40, 100, and 200 mg of SDS, respectively. After five cycles of ON/OFF, we found that all sizes of PNIPAM nanogel were stable and could be switched ON/OFF repetitively. Figure 7 depicts the normalized

fluorescence profile of various-sized PNIPAM nanogel in different BSA concentrations and pH values. As the fluorescence profile did not change for various-sized PNIPAM nanogels in aqueous solution with diverse BSA concentrations or pH values, we can conclude that different-sized PNIPAM nanogels were stable when exposed to different concentrations of BSA and dispersed in aqueous solution with different pH values.

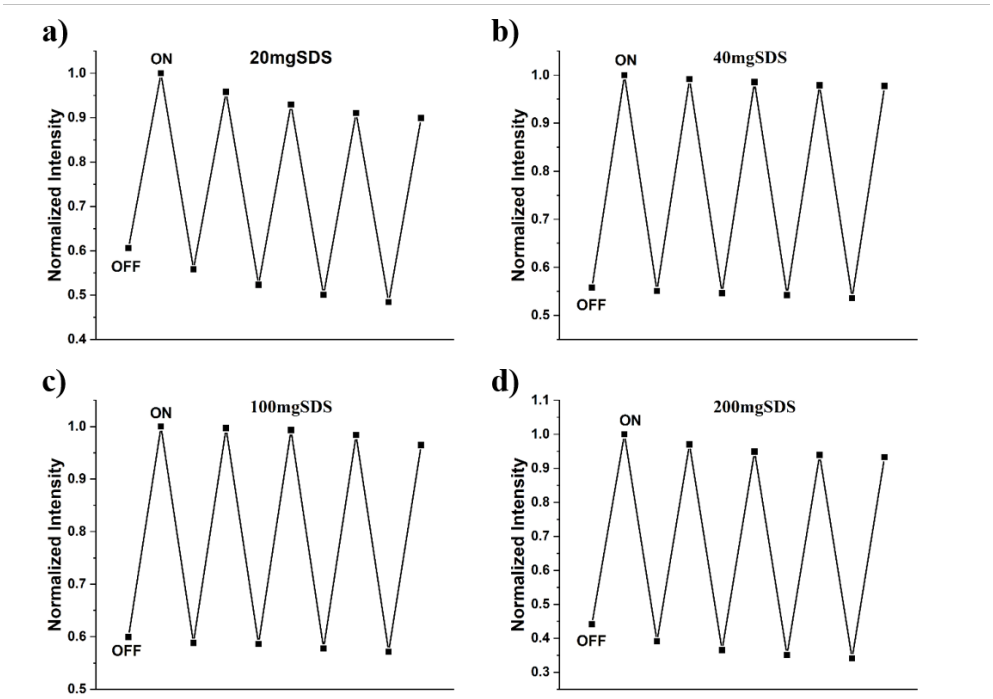

Figure 6. The switch-ON/OFF test of PNIPAM nanogel with a) 20 mg, b) 40 mg, c) 100 mg, and d) 200 mg of SDS. The ICG-PNIPAM was at "OFF" state when temperature at 30 ˚C and at "ON" state when temperature increased to 50 ˚C. A total of five cycles were conducted.

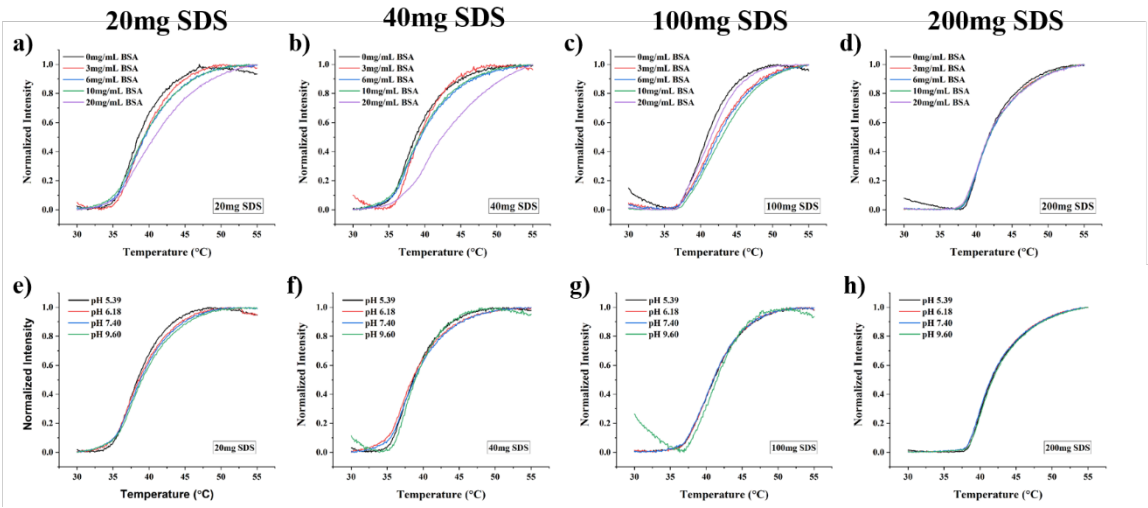

Figure 7. a-d) The stability of PNIPAM nanogel in various concentrations of BSA (0, 3, 6, 10, 20 mg/mL). PNIPAM nanogel synthesized with 20 mg, 40 mg, 100 mg, and, 200 mg of SDS were tested. e-h) The stability of PNIPAM nanogel at various pH levels (5.39, 6.18, 7.40, 9.60). PNIPAM nanogel synthesized with 20 mg, 40 mg, 100 mg, and 200 mg of SDS were tested.

3.4 In vivo USF Imaging of Different-sized PNIPAM Nanogel

The ability to control the size of the PNIPAM nanogel is vital. Different-sized PNIPAM nanogels can be used for different applications. For example, PNIPAM-20mgSDS has been shown to accumulate significantly in the spleen following IV administration [21]. After 3 hours of circulation, the fluorescence intensity in the spleen reached its peak, which indicated the highest concentration of PNIPAM nanogel. A successful *in vivo* 3-D USF image was acquired in the spleen afterwards. After embedding the spleen in porcine heart tissue, *ex vivo* USF imaging was conducted to confirm that the USF signal came from the spleen. The shape of the spleen was clearly observed. The PNIPAM-200mgSDS was also introduced into mice to conduct *in vivo* USF imaging [24]. After IV injection, the

fluorescence signal in the liver increased and reached its peak after 3 hours of circulation, which indicated an accumulation of PNIPAM nanogel in the liver. Thus, *in vivo* USF imaging was conducted in the liver, and a 3-D USF image was acquired.

4. Discussion

4.1 USF Contrast Agent Criteria

Based on the principle of USF imaging, the requirements and criteria for the USF contrast agent are discussed as follows. The contrast agent for USF imaging consists of two parts: the first is the carrier or shell structure, and the second is dyes entrapped or loaded in the carrier.

For the carrier, there are two requirements that need to be met. First, the carrier needs to be thermosensitive, and the structure of the carrier needs to be flexible so that when temperature increases, the size of the carrier decreases and vice versa. Second, the structure of the carrier needs to be stable enough so that it will not collapse after being exposed to a large temperature increase (e.g. > 10 ˚C increase), a high intensity focused ultrasound mechanical force (e.g. mechanical index (MI) > 5), and an *in vivo* biological environment (e.g. contact with proteins, exposure to different pH values, and phagocytosis).

The dye needs to be polar sensitive so that the fluorescence intensity increases when the surrounding microenvironment becomes less polarized and decreases when the surrounding microenvironment becomes more polarized. For example, when the water in the carrier is expelled, the fluorescence intensity of the dye increases and vice versa.

Second, the dye needs to be relatively stable when exposed to light, heat, and ultrasound. The dye should not be photo-bleached quickly so that there is enough time to conduct USF imaging.

After meeting the above-mentioned requirements, both carriers and dyes can become candidates for USF contrast agents. Some key factors, which can be used to predict and evaluate the effectiveness of contrast agents for deep-tissue USF imaging, are summarized in Table 1. First, a low background fluorescence intensity was favored since it helps to minimize background noise and result in a high SNR. However, sometimes we need to use fluorescence imaging to roughly locate the region of interest or track the biodistribution and metabolism pathway of the contrast agent. A higher background fluorescence intensity can give us better fluorescence imaging. Second, the fluorescence increases after fully switching ON, which is one of the most important factors in determining the USF imaging effectiveness of a contrast agent. A high fluorescence intensity is desired to obtain a stronger USF signal and a higher SNR. Also, fluorescence increases after fully switching ON is a key factor in determining the limitation of USF imaging depth. Higher increases mean deeper USF imaging capability. Third, the temperature threshold to switch ON, which is vital and needs to be associated with the USF imaging application. For example, if *in vivo* USF imaging needs to be conducted, a switch-ON temperature point close to the body temperature is desired since the contrast agent will remain at an OFF state and can be easily switched ON with a very small temperature increase to avoid tissue damage caused by temperature increase. Fourth, the temperature transition bandwidth between ON and OFF is also important for *in vivo* applications since a contrast agent can be easily switched

ON with a small temperature increase to avoid tissue damage. Next, the emission spectrum of the contrast agent is desired to be in the NIR range to reduce tissue absorption and increase imaging depth. The storage time and condition also need to be considered. A contrast agent with years-long storage time at room temperature is desired since the contrast agent can be accessed, transported, and kept easily. Another important factor to keep in mind while using the contrast agent for *in vivo* USF imaging is toxicity. A biocompatible or even a U.S. Food and Drug Administration (FDA) approved contrast agent is wanted to avoid toxicity to cells, tissue damage, and organ failure. In addition, the *in vivo* circulation time needs to be considered, especially when working with targeting USF imaging. A longer circulation time allows the contrast agent to have enough time to accumulate in the targeted site to conduct USF imaging.

Table 1. Summary of key factors for USF contrast agent.

Criteria	Desired	Avoid
Background fluorescence	Low	High
Fluorescence increase	High	Low
Switch ON point	Close to body temperature	Far from body temperature
Fully switch ON temperature range	Narrow	Wide
Emission spectra	Near-infarad	Visible light
Storage time/condition	Long/room temperature	Short/freezing
Toxicity	Biocompatible	Toxic
in vivo circulation time	Long	Short

4.2 The Size, Zeta Potential, and Spectrum Properties of PNIPAM Nanogel

The size of PNIPAM nanogel can be precisely controlled by adjusting the quantity of SDS from a scale of 55.6 nm to 551.1 nm. This result agreed with the conclusion made by Mirja

that they were able to show that different concentrations of SDS can result in a size change from around 80 nm to 400 nm for PNIPAM nanogel [26]. According to the TEM image, the majority of PNIPAM nanogels were shown as a round sphere shape. In addition, by observing the PNIPAM nanogel solution, we found that the viscosity of the solution increased when the SDS quantity decreased. There is a trend of zeta potential for different-sized PNIPAM nanogels. As the size increases, the net surface charge of the nanogel becomes more positive. This slight positive charge is beneficial for keeping the nanoparticle from aggregation. Smaller-sized PNIPAM nanogel tends to have a slightly negative or neutral net surface charge. This is not favored since aggregation might occur easily and affect the USF imaging capability. We have observed that ICG-PNIPAM nanogel with 20 mg SDS can be stored up to two years. The emission peak was determined to be 605 nm. Oxidation of ICG dye might be the cause since ICG dye in aqueous solution has an emission peak of around 810 nm [27].

4.3 The Effect of Size on the Fluorescence Intensity of PNIPAM Nanogel

The fluorescence background intensity varies with the size of the PNIPAM nanogel, but there is no obvious trend. The reason for the fluctuation is currently unknown. Both PNIPAM nanogels synthesized with 40 and 200 mg SDS have a relatively low background fluorescence value, and this is beneficial to increasing the SNR. In addition, PNIPAM-200mgSDS has the highest fluorescence intensity increase of 74.1%, and this is an advantage since it has the potential for deeper USF imaging and higher SNR. Also, PNIPAM-200mgSDS has a switch-ON temperature point at 38.2 ˚C, which is slightly above body temperature and suitable for *in vivo* USF imaging. The fully switched ON

temperature ranges for all sizes of PNIPAM nanogel are wide and need improvement to minimize the risk of tissue damage [28]. Above all, we have confirmed that PNIPAM nanogel in various sizes still has a reasonable fluorescence profile and can be used for USF imaging. PNIPAM-200mgSDS is regarded as the most suitable candidate for *in vivo* imaging due to its outstanding fluorescence intensity increase, relatively low background fluorescence, and switch-ON point right above body temperature.

4.4 Stability of PNIPAM Nanogel with Various Sizes

We found that PNIPAM nanogels in different sizes are very stable when exposed to different concentrations of BSA and various pH values. The results indicate that PNIPAM nanogel is a great candidate to be used for *in vivo* USF imaging. It can be stable when in contact with proteins and still be able to conduct USF imaging at different locations in the body where different pH values are expected (e.g., extracellular of tumors usually have an acidic microenvironment [29].)

4.5 Future Applications

The capability of controlling the size of PNIPAM nanogel is critical since different sizes of PNIPAM nanogel can be used for different applications. The large-sized PNIPAM nanogel has the potential to be developed into biomarkers where the movement of contrast agent needs to be minimized because it is more difficult to diffuse than the smaller ones. Tumor targeted USF imaging is also desired because it will enable future research in tumor identification, tracking, and treatment. This small-sized PNIPAM nanogel has a great opportunity to achieve this goal. A recent study has shown a preliminary result that

PNIPAM nanogel can target and accumulate in pancreatic tumors, which may enable USF imaging. This passive targeting is known as the enhanced permeability and retention (EPR) effect. Smaller (<200 nm) nanoparticles may be more efficient at reaching a specific site via the EPR effect [30].

5. Conclusion

In this chapter, we presented a method to control the size of PNIPAM nanogel from around 55 nm to 515 nm. Detailed characterization was conducted shown that by increasing the concentration of SDS, the PNIPAM nanogel size decreased. Also, we found that increasing the SDS quantity led to a slight decrease in the net surface charge of PNIPAM nanogel. In addition, the PNIPAM-200mgSDS is considered the best candidate for *in vivo* deep-tissue USF imaging due to its relatively low background fluorescence, high fluorescence increases after fully switching ON, and a switch-ON temperature point at right above body temperature. All these features can result in a high SNR and minimize potential tissue damage. Further stability tests with ON/OFF cycle, BSA, and pH proved that size does not affect the stability of PNIPAM nanogel. Collaborating work has shown the potential of using different sizes of PNIPAM nanogel to target various organs to conduct USF imaging. Previous successful *in vivo* USF imaging has been achieved in the spleen and liver with PNIPAM-20mgSDS and PNIPAM-200mgSDS, respectively. Both studies showed a reasonable organ accumulation time of 3 hours and a nanogel clean-out time of more than 24 hours. This gives us enough time to finishing the 3-D USF scan. This study not only characterized the PNIPAM nanogel in detail and provided more insight about the properties

of PNIPAM nanogel, but also expanded the applications of PNIPAM nanogel to organ targeted USF imaging and future tumor targeted USF imaging.

Chapter 3

1st Generation of Liposomes (micron-sized particles) for Biocompatible and Near-Infrared USF Imaging.

1. Introduction

Fluorescence imaging is one of the major non-invasive imaging strategies, attracting immense interest in medical imaging applications [31–34]. However, fluorescence imaging suffers from poor spatial resolution in centimeters-deep tissues due to tissue scattering [35]. In our lab, we developed the USF imaging technique to achieve deep-tissue imaging [19,20,36].

While USF imaging has achieved promising results, the current contrast agents have several shortcomings. First, chemicals used during PNIPAM synthesis, such as NIPAM, are known to be toxic to living cells [37]. This may raise safety concerns when ICG-PNIPAM is used for *in vivo* USF studies. Second, compared to the ICG dye aqueous solution, the excitation peak of the ICG-PNIPAM shifted from 788 nm to 660 nm and the emission peak changed from 809 nm to 690 nm [20]. The aza-BODIPY dye used in the micelle contrast agent has a similar excitation peak at 683 nm and an emission peak at 717 nm [38]. For deep-tissue USF imaging, an NIR contrast agent is desired to increase the photon penetration depth and minimize tissue auto-fluorescence [39]. Last, current Pluronic micelle based contrast agents are not suitable for an *in vivo* USF study because they are unstable in biological tissues (such as blood or tissue interstitial fluids) [40]. Thus, significant efforts are required to develop new contrast agents with good bio-stability and biocompatibility.

In this work, we introduce a newly developed ICG-liposome contrast agent to overcome the above limitations and broaden the selection of contrast agents for diverse USF imaging applications. The ICG-liposome was synthesized via an evaporation method to encapsulate the NIR ICG dye into 1,2-dipalmitoyl-sn-glycero-3-phosphocholine (DPPC) based liposomes. The ICG-liposome was further characterized with a home-built cuvette system to examine the correlation between the fluorescence intensity and the temperature. This profile was later used to determine the lower critical solution temperature (LCST) and the storage stability over time. The bio-stability and imaging capability of the ICG-liposome were verified through USF imaging in a tube model, a tissue model, and a tumor model. The in vitro cytotoxicity was evaluated with the mouse 3T3 fibroblast cell line. Subsequently, we studied the metabolism and biodistribution of the ICG-liposome in mice, and both *ex vivo* and *in vivo* USF imaging were conducted.

2. Materials and Methods

2.1 ICG-liposome Synthesis

The ICG solution, which was the source of the fluorescence, was prepared by dissolving the ICG dye (Chem-Impex Int'L Inc., USA) into a mixture of chloroform (99.9% pure) and anhydrous ethanol (4:1 v/v) at a final concentration of 0.28 mg ml-1. As shown in Figure 8, 5.5 mg of DPPC (Avanti, USA) was dissolved in 2 ml chloroform and 200 μl of the prepared ICG solution was added. Next, the mixture was evaporated in a rotor evaporator (BUCHI Corp., USA) at 120 rpm, -85 kPa, and 55 ˚C for at least 1 hour to form the lipid film on the wall of the round flask. Afterward, 1.8 ml hydration water, prepared by mixing

5 % glycerol (99.8% pure) with 95 % PBS (pH 7.4), was added and mixed for 1 hour at 42 ˚C to hydrate the lipid film and form liposomes. The obtained ICG-liposome was further vortexed for 1 min with an amalgamator (DB338, Medical Instrument Co., Ltd, China) and then diluted to 3 ml with PBS and stored at 4 ˚C. Chloroform, anhydrous ethanol, glycerol, and PBS were purchased from Fisher Scientific International, Inc., USA.

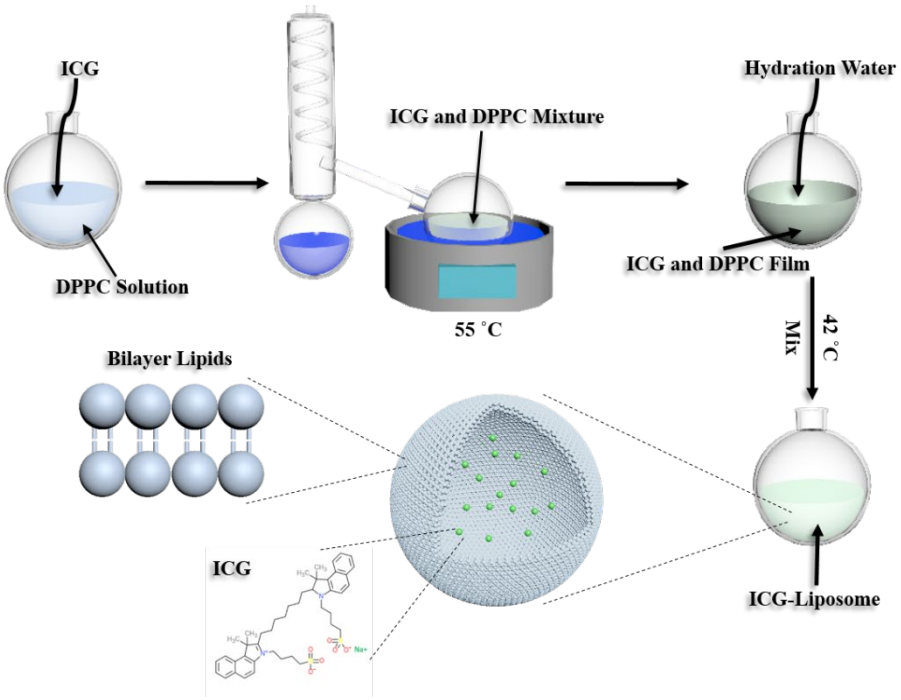

Figure 8. Schematic diagram of ICG-liposome synthesis.

2.2 ICG-liposome Characterization

To study the fluorescence intensity changes in response to the temperature changes, an in-house built system was implemented [20]. Briefly, a 3 ml sample was transferred into a quartz cuvette (Hellma, Germany) and then immersed in a water bath. A temperature controller (PTC10, Stanford Research System, USA) monitored and controlled the water bath temperature. A nitrogen laser (GL3300, Horiba, Japan) generated the excitation light

to excite the sample at 775 nm and the emission light passed through an 830 nm long-pass filter (Semrock, USA) before being received by a photomultiplier tube (PMT, H7422-20, Hamamatsu, Japan). In addition, the cuvette system was employed to assess sample stability over-time. The hydrodynamic size was characterized with a DLS (NanoBrook 90PlusPALS, Brookhaven Instruments, USA) at various temperature points. The excitation and emission spectra were measured with a spectrometer (Fluoromax-Plus-C, Horiba, Japan). During an excitation spectrum scan, an 825 nm long-pass emission filter (Edmund Optics, USA) was used while an 840 nm wavelength peak was selected for emission light detection. An excitation light of 530 nm and a 550 nm long-pass emission filter (Edmund Optics, USA) were applied during an emission spectrum scan.

2.3 USF Imaging – Tube Model, Tissue Model, and Tumor Model

An in-house built frequency-based USF imaging system, as proposed in previous published work [21], was utilized to conduct USF imaging with the ICG-liposome. First, we used a tube model to determine the effect of blood on the performance of the ICG-liposome. Briefly, a silicone tube (inner diameter: 0.31 mm; outer diameter: 0.64 mm; ST 60-011-01, Helix Medical, USA) was inserted through a 1 cm thick porcine muscle tissue at a 0.5 cm depth and then placed it in a water tank with a temperature maintained at 38 ˚C. The ICG-liposome was mixed with the PBS buffer (1:1 v/v) or the mouse blood (BioIVT, USA) (1:1 v/v) and then injected the mixture into the tube. During a USF scan, a laser light (4.6 mW cm-2) illuminated the tube model and a HIFU transducer (2.5 MHz, H-108, Sonic Concepts Inc., USA) was used to induce a temperature rising and switched on the ICG-liposome. The power of the HIFU was 0.31 W (Equation 1), and the scan area was 5.080 mm x 5.080

mm with step sizes of 0.127 mm and 1.270 mm in the X and Y directions, respectively. The emission light was filtered through two 830 nm long-pass filters and one 830 nm absorption filter before collection by a PMT detector. Second, the effect of tissue on the performance of the ICG-liposome was studied using a porcine muscle tissue model. For the purpose of co-registration, the ICG-liposome was mixed with a CT contrast agent (ExiTronTM nano 12000, Miltenyi Biotec, Germany) at a ratio of 3:1 in volume. Then, the 40 µl mixture was injected into a 1.2 cm thick porcine muscle tissue. The USF imaging setup was similar to the previously described configuration, only with a lower laser intensity (53 µW cm-2) and a higher HIFU power (4.01 W). The scan volume was 8.636 mm × 8.636 mm × 10.160 mm with a lateral step size of 0.508 mm and an axial step size of 2.032 mm. The CT scan was completed with a commercial micro-CT (Skyscan 1178, Bruker, Belgium). Next, to investigate the capability of conducting the USF imaging with the ICG-liposome in a tumor micro-environment, a tumor model was adopted. A female nude mouse (athymic nude mice, Jackson Lab, USA) was implanted U-87 brain cancer cells (ATCC, USA) at its thigh to construct the tumor model. The ICG-liposome and CT contrast agent mixture (60 µl, 2:1 v/v) was locally injected at the tumor site. Then, USF scan was performed with a laser light intensity of 13 µW cm-2 and a HIFU power of 4.96 W. The scan volume was 6.096 mm × 6.096 mm × 8.890 mm with a lateral step size of 0.508 mm and an axial step size of 1.778 mm. After the USF scan, the mouse was sacrificed and a micro-CT was used to scan and construct a CT image. The anesthesia machine (Supera Anesthesia Innovations, USA) was employed during the USF scan applied a 1.8 % isoflurane (Miller Veterinary Supply, USA) at 0.8 L min-1. The imaging reconstruction and co-registration were conducted according to a previously published method [21].

$$P = \frac{8849.32 \times E \times V^2}{G}$$ **Equation1**

P: Ultrasound power transmitted into the tissue, W.

E: 2.5 MHz transducer efficiency, usually at 0.7.

V: Transducer driving voltage, V.

G: Gain of the amplifier, 48.5 dB.

2.4 Metabolism and Biodistribution

A female mouse (17.98 g, BALB/c, Jackson Lab, USA) was administered with 75 μl ICG-liposome via IV injection. The metabolic process was recorded for 80 min with an EM-CCD camera (ProEM®-HS:1024BX3, Princeton Instruments, USA), equipped with four 830 nm long-pass filters (Semrock Inc., USA) and an 830 nm absorptive filter (Newport Corporation, USA) over a camera lens (35 mm fixed-focal-length Lens, Edmund Optics Inc., United States). The excitation light used an 808 nm laser (Dragon Lasers, China) with a 785/62-25 nm band-pass filter (Semrock Inc., USA). After 80 min, the mouse was sacrificed and major organs were dissected out for biodistribution imaging under the EM-CCD camera. Apart from that, another female BALB/c mouse (19.63 g) was injected with the ICG-liposome and sacrificed after 10 min for biodistribution imaging.

2.5 Cell Viability

A cell proliferation assay kit (Promega, USA) was used to assess the cytotoxicity of the ICG-liposome. Briefly, mouse 3T3 fibroblast cells (ATCC, USA) were cultured in a 98-well plate (Falcon, Corning, USA) and incubated with five concentrations of DPPC (95,

185, 345, 605, and 832 μM). Each concentration was repeated five times. A positive control group with no ICG-liposome and a negative control group with no cells but with ICG-liposome were also considered. Three time periods (24, 48, and 72 hours) were studied.

2.6 USF Imaging-ex vivo and in vivo

The body hair of a female BALB/c mouse (18.39 g) was removed and 100 μl ICG-liposome was injected via IV infusion. After 20 min, the mouse was sacrificed and dissected. A partial right lobe of the liver was removed and embedded in 1 cm thick porcine muscle tissue. Next, the porcine muscle tissue was secured in a water bath with the temperature maintained at 38 ˚C (PTC10, Stanford Research Systems, USA). The *ex vivo* USF scans started with an excitation light of 176 μW cm-2 at 808 nm and a HIFU power of 7.74 W. The scan volume was 7.112 mm × 7.112 mm × 6.350 mm with a lateral step size of 0.508 mm and an axial step size of 1.270 mm. The *in vivo* USF imaging was conducted with a shaven female BALB/c mouse (26.36 g). A USF scan was proceeded after 20 min of IV injection of 200 μl ICG-liposome. The mouse was placed in a container, which was positioned at the surface of a water bath, faced up and anesthetized with 1.8 % isoflurane at a flow rate of 0.8 L min-1. We utilized the same laser setup with a HIFU power of 9.71 W. The scan volume was 15.240 mm × 15.240 mm × 6.350 mm with a lateral step size of 1.524 mm and an axial step size of 1.270 mm.

2.7 Statistical Analysis

Statistical analysis was conducted with the R software (Version 3.5.3). An analysis of variance (ANOVA) test was conducted in Figure 14, and a p-value of less than 0.05 was

considered a significant difference between the two data groups. Normalization was performed for the data in Figure 9b-c and Figure 14 before data analysis. A standard deviation was utilized for replicated data.

2.8 Ethical Statement

All animal studies follow the protocol of the University of Texas at Arlington's Institutional Animal Care and Use Committee (IACUC).

3. Results

3.1 The ICG-liposome characterization

A profile of the fluorescence intensity changes with respect to the temperature increasing is shown in Figure 9a. Interestingly, the ICG-liposome was observed to have two LCSTs, at 32 ˚C and 42 ˚C. The fluorescence intensity changes were 8.6 folds from 32 ˚C to 38 ˚C and 2.0 folds from 42 ˚C to 45 ˚C. To understand the mechanism of the fluorescence intensity change, the ICG-liposome hydrodynamic size was measured. The mean hydrodynamic size changed from 6.49 μm ± 0.31 μm to 0.91 μm ± 0.06 μm as the temperature rose from 42 ˚C to 45 ˚C. In addition, the fluorescence microscope results also confirmed that the size of the ICG-liposome was around 7 μm (Appendix C). Further size measurements were conducted with the transmission electron microscope and showed an extended size range from 136 nm to 10.11 μm (Appendix C). Figure 9b shows the relationship between the normalized fluorescence intensity and the temperature measured at different days of storage. It indicates the shape of the curve was stable, which means the two LCSTs were stable and had not shifted in 141 days. Figure 9c shows that the

background fluorescence intensity, which was the fluorescence intensity measured at 24 ˚C, was elevated as the storage time increased (the data were acquired at 24 ˚C). As shown in Figure 9d, the first LCST fluorescence intensity fold change was also affected by the storage time. A clear trend is shown that the fluorescence intensity fold decreased when the preserving time was extended. Figure 9e shows the fold change of fluorescence intensity at the second LCST. Similarly, as the storage time was prolonged, the fluorescence intensity fold change declined.

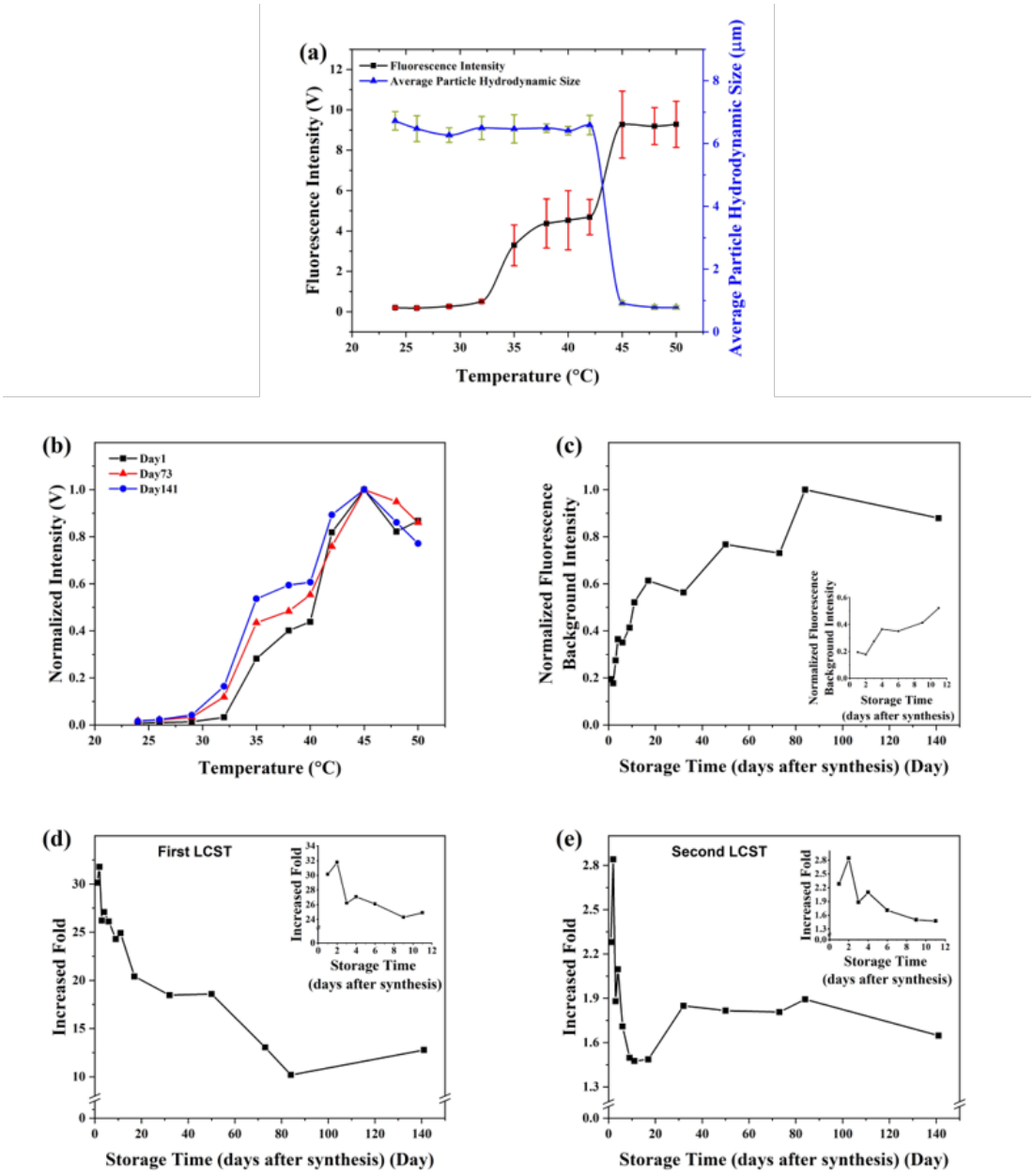

Figure 9. Fluorescence and hydrodynamic size measurements of the ICG-liposome. a) The correlation between fluorescence intensity and temperature was labeled with a black line. The change of the hydrodynamic size with respect to the temperature was labeled with a blue line. The number of replicates was n > 5. b) The change in fluorescence intensity profiles from day 1 to day 141. c) The change of background fluorescence intensity over-

time at 24 ˚C. The fold changes of fluorescence intensity at the d) first LCST and e) the second LCST over-time. The inserts illustrate a magnified view of the first 12 days.

As shown in Figure 10, the excitation peaks of the ICG aqueous solution and the ICG-liposome were at 788 nm and 786 nm, respectively. A closer inspection of the figure shows that after loading the ICG into the liposome, the emission peak shifted from 809 nm to 836 nm. This slight red shift was favorable for separating the emission photons from the excitation photons.

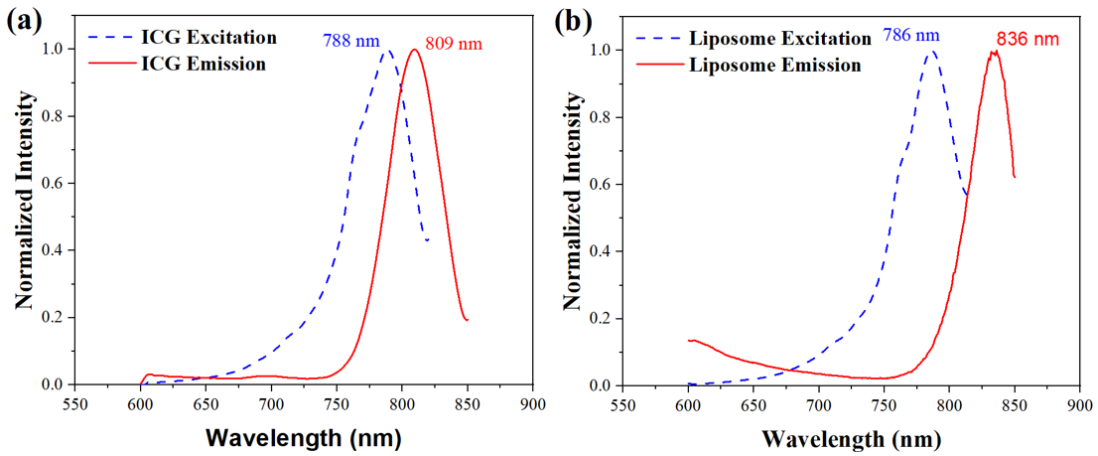

Figure 10. Excitation and emission spectra of a) the aqueous ICG solution and b) the ICG-liposome.

3.2 USF Scans in A Tube Model, A Tissue Model, and A Tumor Model

After understanding the thermal responsive attribute of the ICG-liposome and its spectra, we further tested the feasibility of using the ICG-liposome in various environments for USF imaging. A tube model was prepared with a silicon tube inserted into a porcine muscle tissue with a thickness of 1 cm (Figure 11a). The ICG-liposome mixed with mouse blood

or phosphate buffer saline (PBS) was injected into the tube before conducting USF scans. Figure 11b and Figure 11c, respectively, present two-dimensional (2-D) USF images of a silicone tube filled with the ICG-liposome mixed with mouse blood and PBS. The ICG-liposome mixed with mouse blood shows a relatively strong USF signal compared with the USF signal of the ICG-liposome mixed with PBS. Additionally, the ICG-liposome had an SNR of 30.95 ± 5.85 dB and 27.17 ± 1.70 dB at depths of 1 cm and 1.5 cm, respectively (Figure 12). A silicone tube (inner diameter: 0.31 mm; outer diameter: 0.64 mm; ST 60-011-01, Helix Medical, USA) was embedded in a clear silicon phantom and porcine muscle tissue was placed on top (as shown in Figure 12a and 12b). The ICG-liposome was injected into the tube before USF scan. An 808 nm excitation light with an intensity of 32.58 mW cm-2 illuminated on the sample and 0.46 W USF was applied. The USF image of the 1 cm thick porcine tissue is shown in Figure 12d and the SNR is 30.95 ± 5.85 dB. The width of the imaging band was 1.04 ± 0.15 mm at a threshold of 0.25. The USF image of the 1.5 cm thick porcine tissue is shown in Figure 12f and the SNR is 27.17 ± 1.70 dB. The width of the imaging band was 1.03 ± 0.12 mm at a threshold of 0.25. This result confirmed the ability of using the ICG-liposome for centimeter-deep tissue USF imaging.

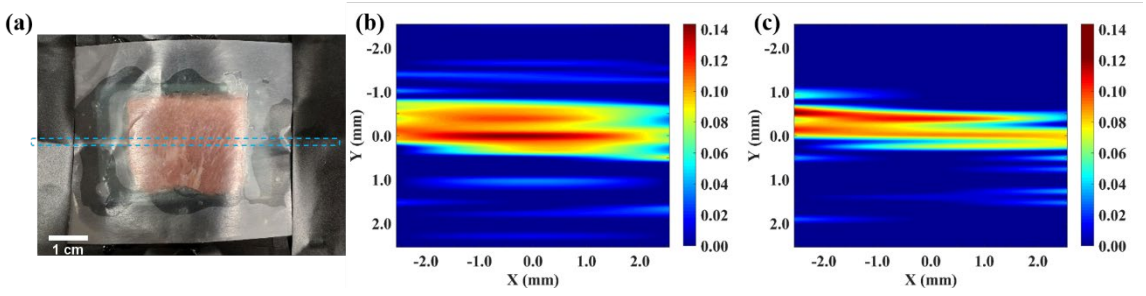

Figure 11. The tube model. a) A silicon tube (outlined in blue dash line) embedded in a porcine muscle tissue. USF images of the ICG-liposome mixed with b) mouse blood and c) PBS in a silicone tube.

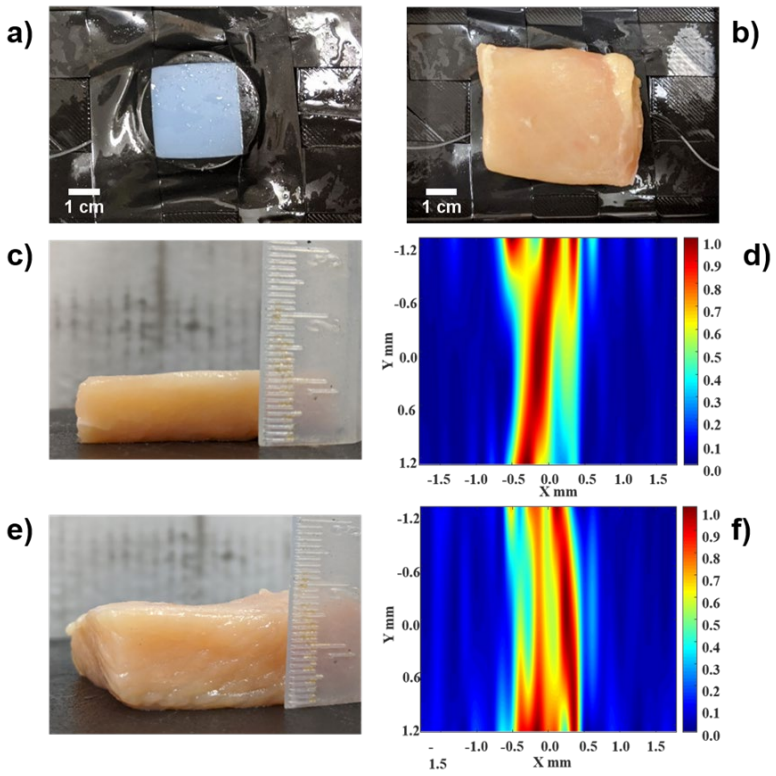

Figure 12. USF imaging of the ICG-liposome at various depths. a) A silicone tube was embedded in a clear silicone phantom. b) A porcine muscle tissue was placed on top of the silicone phantom. c) The thickness of porcine muscle tissue is 1 cm, and the USF image at 1 cm is shown in d. e) The thickness of porcine muscle tissue is 1.5 cm, and the USF image at 1 cm is shown in f.

Next, we explored whether the ICG-liposome could be used to conduct USF imaging in a tissue environment. To perform a co-registration between the USF and CT images, we

mixed the ICG-liposome with a CT contrast agent (3:1 v/v). Figure 13a-c display a 3-D USF image, a USF and CT overlaid image, and a CT image, respectively. The XY-plane slices from Figure 13b at different depths are shown in the appendix. (Appendix D). According to the figures shown below, the USF image presented a lateral space distribution comparable to that of the CT image. However, the axial space distribution of the USF image was wider than that of the CT image. In addition, we assumed that the ICG-liposome and the CT contrast agent were mixed well and might have similar space distribution within the porcine muscle tissue. In practice, they may not follow exactly the same distribution pattern. An *in vivo* tumor mouse model was implemented to study the USF imaging feasibility and capability of the ICG-liposome inside a tumor micro-environment. One of the reasons we chose the U87 tumor cell was that it grew fast inside the mouse. Also, U87 tumor model can provide us a large volume to study the deep-tissue USF imaging. Similar to the previous experiment, the ICG-liposome was mixed with the CT contrast agent (2:1 v/v). Figure 13d-f show 3-D images of the USF image, the USF and CT overlaid image, and the CT image at a 45-degree view. The XY-plane slices of the overlaid USF and CT image (Figure 13e) at various depths are listed in the Appendix D. Clearly, 3-D USF images were successfully acquired in live tumorous mouse tissue. An identical observation was made that the USF image spreads more along the axial direction than along the lateral direction.

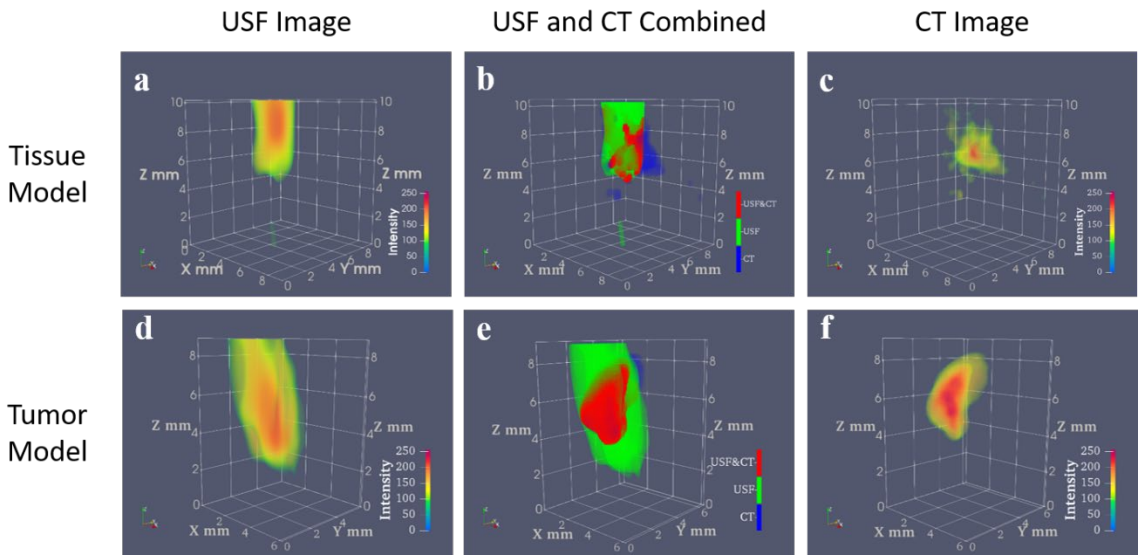

Figure 13. The comparison between the USF image and the CT image in both the tissue and the tumor model. a) and d) USF image, b) and e) USF and CT overlaid image, and c) and f) CT image in a porcine muscle tissue.

3.3 Biocompatibility and Biodistribution Measurements

After verifying the feasibility of implementing the ICG-liposome for USF imaging with mouse blood, porcine muscle tissue, and a tumor model, we proceeded to study the cytotoxicity of the ICG-liposome. Figure 14 summarizes the statistical analysis of the MTT test, which confirmed that there was no statistically significant ($p > 0.05$) difference between the control and the experimental groups if the DPPC concentration was kept under 345 μM within 24, 48, and 72 hours of incubation. As the DPPC concentration increased to 605 μM or above, a statistically significant difference emerged between the experimental groups and the control group ($p < 0.05$). In addition, the cell viability decreased to less than 80%, indicating minor cytotoxicity.

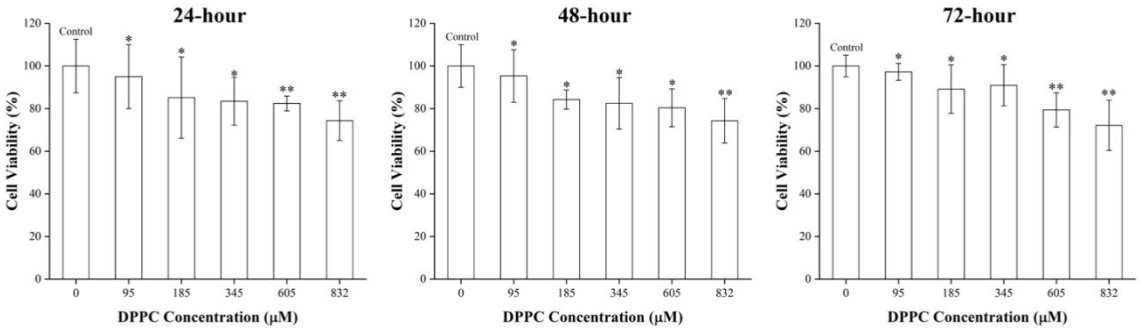

Figure 14. Mouse 3T3 fibroblasts cell viability test with the ICG-liposome at 24-hour, 48-hour, and 72-hour intervals. The number of replicas was n = 5. A one-way analysis of variance (ANOVA) analysis was conducted. (*The p-value is greater than 0.05 with respect to the control group; **the p-value is less than 0.05 with respect to the control group.).

The biodistribution and the metabolic pathway of the ICG-liposome were studied (Figure 15a-c). The ICG-liposome primarily accumulated in the lung, liver, and small intestine after 10 min of an IV injection into a tail vein (75 μl). At 80 min, the ICG-liposome accumulated primarily in the liver and the small intestine. The metabolic pathway is shown in Figure 15d. The majority of the ICG-liposome clearly reached the liver first and then slowly decomposed and traveled to the small intestine. The highest fluorescence signal was obtained at 20 min. Therefore, the mouse was sacrificed at 20 min for the following *ex vivo* and *in vivo* studies.

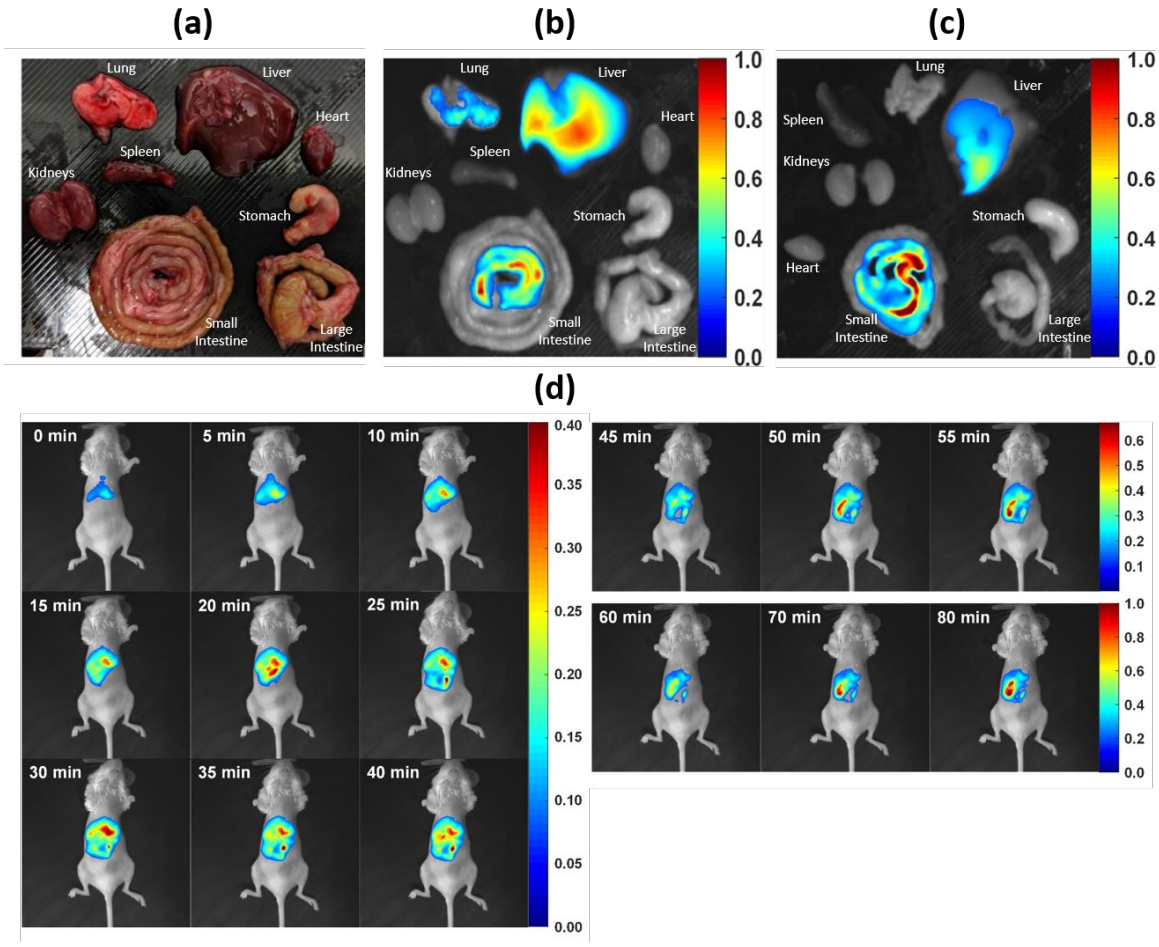

Figure 15. Biodistribution and metabolic pathway of the ICG-liposome. a) Color image of major organs. The fluorescence image of major organs b) after 10 min and c) after 80 min of an IV injection of the ICG-liposome. d) Metabolic pathway of the ICG-liposome.

3.4 Ex vivo and in vivo USF Imaging

We conducted an *ex vivo* USF scan based on the knowledge we acquired previously, and the result is shown in Figure 16. The partial right lobe of the liver was dissected from the mouse 20 min after an IV injection via a tail vein. The liver was approximately 0.9 cm wide (Figure 16a). To simulate the *in vivo* environment, the liver was embedded in porcine muscle tissue, which had a thickness of 1 cm, at 0.5 cm depth (Figure 16b). The 3-D USF

image is shown in Figure 16c, and the XY-plane slicing images are shown in Figure 16d1-d6.

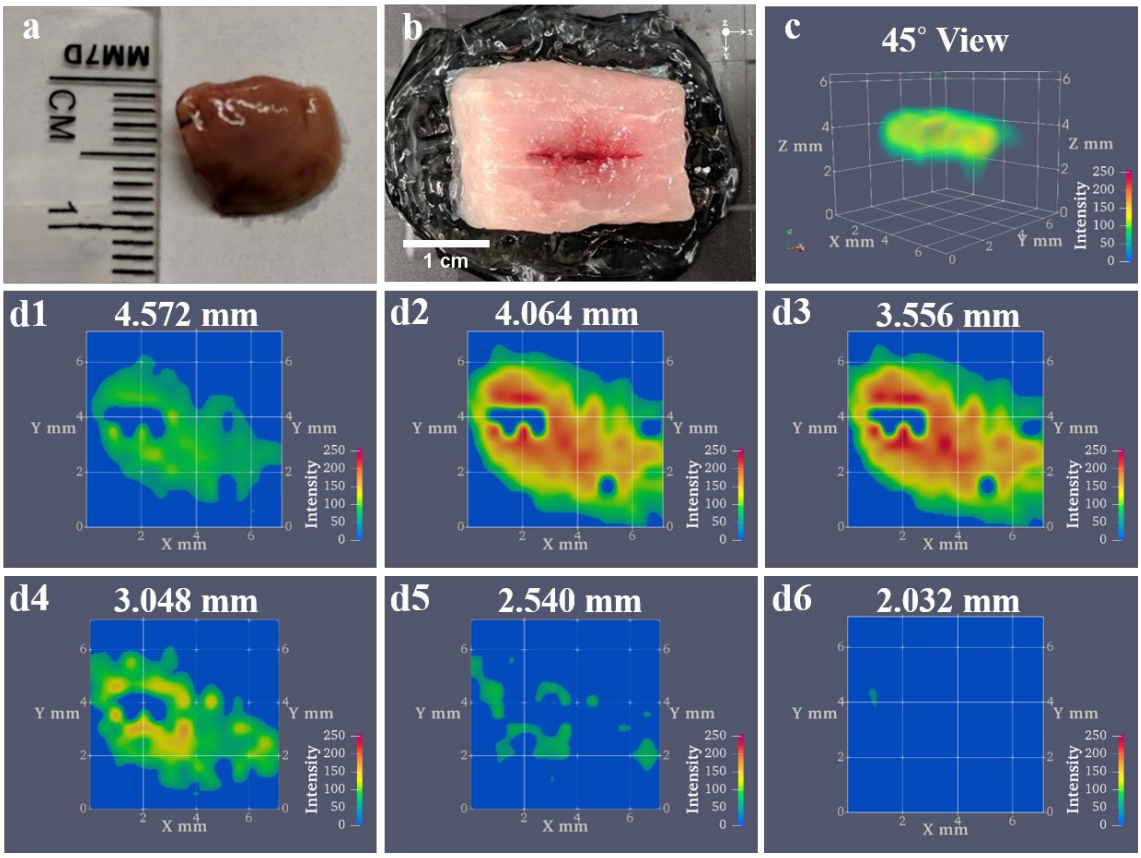

Figure 16. USF *ex vivo* imaging. a) Color image of the partial right lobe of the liver. b) Liver was placed in a porcine muscle tissue at about 0.5 cm depth. c) A 45-degree view of the 3-D USF image of the embedded liver. d1-d6) The XY-plane slicing images at different depths.

The *in vivo* 3-D USF image was successfully obtained with the ICG-liposome. Figure 17a presents a 45-degree view of a 3-D *in vivo* USF image, a scan of the whole chest of a mouse with a volume of 15.240 mm × 15.240 mm × 6.350 mm was conducted. The XY-plane

slicing images are shown in Figure 17c1-c6. The mouse was laid on its back, and we could easily observe that most of the USF signals came from the right lobe of the liver. This agreed with the *ex vivo* study where the ICG-liposome in the right lobe liver retained the thermoresponsive characteristics.

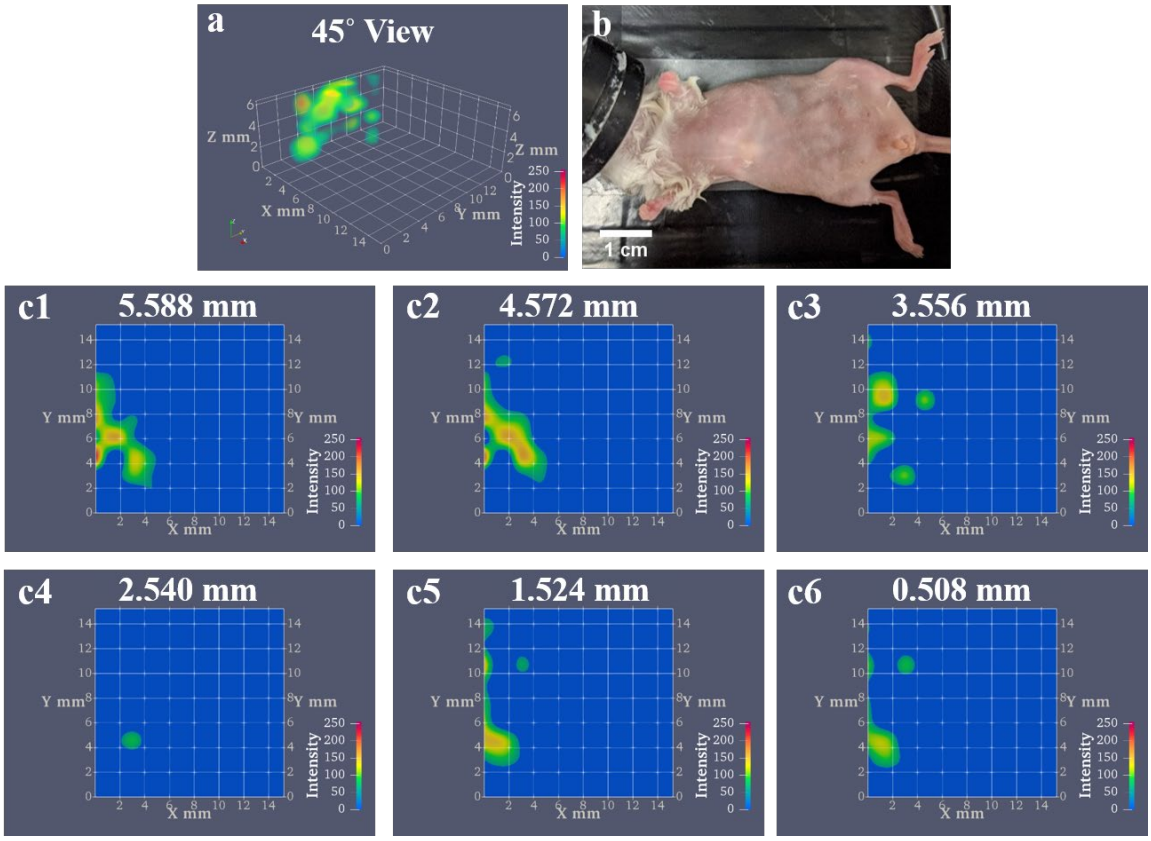

Figure 17. USF *in vivo* imaging. a) A 45-degree view of the 3-D *in vivo* USF image. b) Color image of a shaven mouse for the USF scan. c1-c6) The XY-plane slicing images at different depths.

4. Discussion

The newly developed ICG-liposome broadens the selection of USF contrast agents with unique advantages, and its outstanding performance makes it an exceptional candidate for USF imaging. The ICG-liposome has a narrow transition temperature range of 3 ˚C at the second LCST, a red-shifted emission peak at 836 nm, a low cytotoxicity property, and *in vivo* stability.

The ICG-liposome has several excellent characteristics that make it particularly suitable for USF imaging. Its two LCSTs allow it to be potentially used at temperatures near 32 ˚C and body temperature, separately, for USF applications. During both *ex vivo* and *in vivo* USF scans, we focused on using the second LCST, which was close to the mouse's body temperature. Based on the data shown in Figure 9, the second LCST is caused by the shrinking of the ICG-liposome because the hydrodynamic size decreased when the fluorescence intensity increased. In addition, the transition temperature range at the second LCST is 3 ˚C, allowing a quick response to the temperature change and low ultrasound energy input. Compared to the PNIPAM nanoparticles [20], the ICG-liposome is more suitable for deep-tissue *in vivo* USF imaging, where tissue auto-fluorescence is the major contributor to the total background fluorescence, since the absolute intensity difference caused by the second LCST is much higher than the absolute intensity difference of the PNIPAM nanoparticles. On the other hand, PNIPAM nanoparticles are more suitable for *in vivo* superficial USF imaging, where the contrast agent background fluorescence is the major contributor to the total background fluorescence, compared to the ICG-liposome, since the background fluorescence of the ICG-liposome will easily saturate the detector

and weaker laser illumination is necessary. Indeed, the first LCST of the ICG-liposome will increase the noise during imaging, and the fold change of the second LCST is small. It is a good research direction to remove the first LCST and increase the fold change of the second LCST so that the ICG-liposome is more suitable for *in vivo* study. The results of the stability study indicate that the increasing folds of both the first and second LCSTs decreased as the storage time increased. For optimum performance, it is suggested to use the ICG-liposome within the first week after the contrast agent is made. Additionally, the background fluorescence intensity increased as the storage time increased, which might be caused by a slow release of ICG dye caused by the breaking of the liposome structure. The emission peak of the ICG-liposome was found to be red-shifted by 27 nm when compared with the emission peak of the ICG aqueous solution. This feature is desirable because the interference with the auto-fluorescence is even minimized and the absorption by biological tissue is further reduced [41].

The excellent bio-stability of the ICG-liposome was confirmed with USF imaging in the tube model, tissue model, and tumor model. After mixing the ICG-liposome with mouse blood in a tube model, the USF signal became stronger, possibly because of the protein-liposome interaction, which decreases the link strength between lipids so that the degree of contraction increased as the temperature rose, resulting in a higher fluorescence intensity [42]. Overall, the ICG-liposome was stable to be used for the USF scan after mixing with the mouse blood. The co-registration between the USF and CT images indicates that the USF image is spread more in an axial direction than in a lateral direction. This is partially due to the non-uniform focal size of the ultrasound beam [21]. The accomplishments of

USF imaging with the ICG-liposome in both mouse blood and porcine muscle tissue support the next *ex vivo* and *in vivo* USF imaging via IV injection. Additionally, USF scans of the ICG-liposome in a tumor model is achieved, making the ICG-liposome possible to be used in an *in vivo* tumor targeting USF imaging in the future.

Another important advantage of the ICG-liposome is its safety and biocompatibility. Both DPPC and ICG are chemicals approved by the U.S. FDA for use in drug delivery and fluorescence imaging fields [43,44]. As shown in Figure 14, the in vitro cell viability assay verifies that the ICG-liposome with a dosage equal to 345 μM or less has negligible cytotoxicity. After administrating the ICG-liposome through an IV injection, the majority of contrast agents accumulated in the liver and the small intestine, because large particles tend to be absorbed by macrophages and decomposed in the liver [45,46]. Both the liver and the small intestine were tested in a water bath with a temperature controller, and the thermal responsive property of the ICG-liposome inside the liver was conserved (Appendix E). By contrast, although the small intestine had a fluorescence signal, it had no thermal responsive property. The fluorescence signal from the small intestine may have stemmed from the free ICG dye [47]. Therefore, the liver was selected as the target for the *ex vivo* and *in vivo* USF imaging.

Finally, we successfully implemented the ICG-liposome in both *ex vivo* and *in vivo* USF imaging. Although the biodistribution results in Figure 15 (acquired via 2-D planar images) indicate that the whole liver emitted fluorescence, according to both the *ex vivo* and the *in*

vivo USF scans, the thermal responsive characteristic was only present in the right lobe of the liver.

Future experiments will attempt to reduce the size of the ICG-liposome to a nano-scale. Because nanoparticles have larger surface areas and smaller sizes, there are more opportunities to functionalize the surface of the ICG-liposome, and it is more likely to bypass biological barriers. Micro-particles are more appropriate for local injection since they tend to remain near the location where they are injected, while nanoparticles are more suitable for blood vessel circulation when imaging specific targets [48]. Thus, a smaller-sized ICG-liposome is preferred for intravenous delivery to accomplish *in vivo* targeting USF imaging in the future. In addition, the LCST of the ICG-liposome can be improved and adjusted to a point slightly above the body temperature so that heat introduced to the local region can be reduced during USF imaging.

5. Conclusion

An NIR and biocompatible contrast agent, ICG-liposome, was developed and investigated for USF imaging. The results revealed that the ICG-liposome had a narrow transition temperature range at the second LCST, making it suitable for *in vivo* USF imaging. In addition, the NIR emission peak of the ICG-liposome was at 836 nm, so that the auto-fluorescence interference and the tissue absorption were minimized. The low cytotoxicity was verified via in vitro cell viability tests. Further examinations with USF scans revealed the outstanding bio-stability of the ICG-liposome in blood, porcine muscle tissue, and tumor environments. Both *ex vivo* and *in vivo* USF imaging of the liver were successfully

conducted with the ICG-liposome and 3-D USF images were acquired. The advantages of the ICG-liposome make it a promising contrast agent for applications in various fluorescence imaging fields, such as *in vivo* organ imaging, deep-tissue biomarkers, and tumor imaging. We believe that the ICG-liposome based USF imaging technique will be a valuable tool for biomedical imaging.

Chapter 4

2nd Generation of Liposomes (Nano-sized particles) for USF imaging and Ultrasound Assisted Release

1. Introduction

In the previous chapter, we developed the ICG-encapsulated liposome using biocompatible lipids during synthesis. We also observed a higher fluorescence intensity changes compared to that of the PNIPAM nanoparticles, and we conducted a successful *in vivo* USF imaging [36,49]. However, the size of the liposome was around 6.5 μm, which was too large and limited its usage if *in vivo* accumulation was desired via bypassing biological barriers.

Liposomes have been widely used as drug carriers due to their outstanding advantages, which include biocompatibility, self-assemble capability, feasibility to load both polar and non-polar drugs, and easy surface modification for molecular targeting and conjugation to functional groups. For example, doxorubicin (DOX)-encapsulated liposomes were used for targeted drug delivery [50–52]. However, lack of drug release control has been considered as one of the issues [53]. Ultrasound mediated drug release of liposomes is one of the potential solutions to overcome this barrier [54,55]. Furthermore, studies with liposomal structure modification via PEGylation on the surface showed an increased efficiency of liposomes broken via ultrasound [56]. Combining imaging with liposome drug release provides a controllable drug delivery option, and recent research has successfully used fluorescence imaging to confirm the accumulation of liposomes in a tumor before conducting a temperature-triggered drug release [57].

A combination of USF imaging and ultrasound-controlled release using ICG-encapsulated liposome nanoparticles (LNPs) is explored in this chapter. We synthesized various sizes of liposomes and decorated the surface of liposomes with PEGylated chains and folate to enhance physiological stability and potential future folate-targeting. We examined the relationship between the emitted fluorescence intensity and temperature with an in-house built cuvette system and measured both spectrum and size with a spectrometer and a DLS particle analyzer, respectively. We studied the USF imaging feasibility and imaging depth with a silicone tube phantom model. Finally, we determined the ICG releases with various HIFU powers and exposure times.

2. Materials and Methods

2.1 Liposome Nanoparticles Synthesis

The schematic diagram of synthesizing ICG-encapsulated LNPs is shown in Figure 18. In a 25 mL round-bottom flask, 5 mg 1,2-dipalmitoyl-sn-glycero-3-phosphocholine (DPPC) and 0.22 mg 1,2-distearoyl-sn-glycero-3-phosphoethanolamine-N-[folate(polyethylene glycol)-2000] (DSPE-PEG2000-Folate) were dissolved in 2 mL chloroform (98 %, Fisher Scientific International, Inc., USA). A rotor evaporator (R300, BUCHI, Corp., USA) was used to completely remove chloroform at 55 ˚C, -85 kPa, and 120 rpm in 30 min. A thin layer of lipid film was formed on the wall of the flask. Then, 0.8 mL pre-warmed ICG (≥ 96 % HPLC, Fisher Scientific International, Inc., USA) aqueous solution (0.07 mg/mL) was added into the flask and swirled in the water bath at 55 ˚C for 30 seconds, followed with rotor evaporating to hydrolyze lipids at 42 ˚C and 120 rpm for 60 min. Next, the size

of the liposomes was controlled via an extrusion method. The desired polycarbonate filter disk size (30 nm, 50 nm, 100 nm, or 200 nm) was loaded into the mini-extruder (Avanti Polar Lipids Inc., USA) with two filter supports. The filter disk was pre-wetted with DI water before extruding. The liposome solution was aspirated into a gas-tight 1 mL syringe and inserted into the mini-extruder. Another empty syringe was also placed at the other end of the mini-extruder. The assembled mini-extruder apparatus was placed in a pre-heated (50 ˚C) heating block and waited for 10 min to equilibrate the liposome solution. Afterwards, the liposome solution was filtered 19 times. When filtering with both 30 nm and 50 nm filter disks, a pre-filtering using the 100 nm filter disk was required. Next, the obtained LNPs solution was dialyzed against DI water at 4 ˚C for 24 h to remove free lipids and ICG dye. The DI water was added to the LNPs solution after dialysis to a final volume of 3.5 mL. Finally, the LNPs were stored in a sealed container at 4 ˚C and used within 2 days. Both DPPC and DSPE-PEG200-Folate were purchased from Avanti Polar Lipids, Inc., USA.

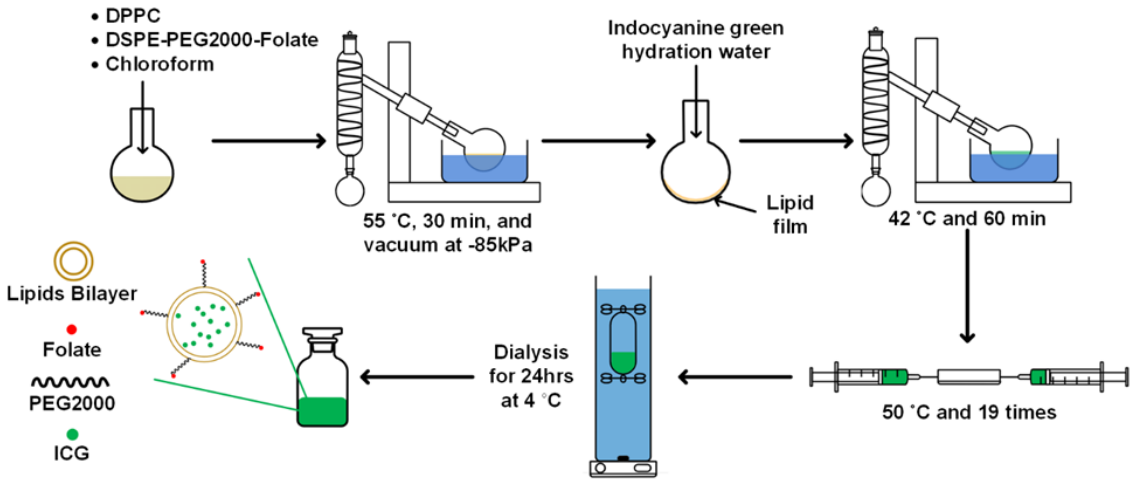

Figure 18. The schematic diagram of synthesizing PEGylated and ICG-encapsulated liposome nanoparticles.

2.2 Liposome Characterization

The effectiveness of liposomes as a USF imaging contrast agent was evaluated via an in-house built cuvette system [36]. Briefly, 3 mL liposomes were pipetted into a 3.5 mL quartz cuvette (Hellma, Germany), which was placed inside a temperature-controlled holder (Quantum Northwest, Inc., USA). An 808 nm laser (MGL-II-808-2W, Dragon Lasers, China) was utilized as an excitation light to excite liposomes. The emission light from liposomes passed through an 830 nm long-pass (LP) filter (Semrock, USA) before being collected by a modular USB spectrometer (USB2000+, Ocean Inlight, USA). The emitted fluorescence intensity change with respect to the change in temperature was recorded with a temperature increment of 0.1 ˚C. In addition, the physiological stability of liposomes was evaluated with the effects of ionic strength and pH using the cuvette system. The potassium chloride (KCl) solution with different concentrations (0, 25, 50, 100, 150, 200 mM) or an aqueous solution with various pH (5.2, 6.3, 7.4, and 9.2) were mixed with LNPs in a 5:1 ratio (v/v), accordingly. To further study the physiological stability of the LNPs, the mouse blood serum (BioIVT, USA) was mixed with the LNPs (1:1 v/v) and the fluorescence intensity change with respect to the change in temperature was measured using the cuvette system.

The hydrodynamic sizes of liposomes were measured with the DLS particle analyzer (NanoBrook 90PlusPALS, Brookhaven Instruments, USA). The incident angle of the 659

nm laser was 90˚. Samples were diluted with DI water until the count rate reaches 300-700 kcps and the temperature was set at 30 ˚C. Later, samples were heated to 50 ˚C with an increment of 2 ˚C. A temperature equilibrium time of 10 min was used to ensure temperature inside the cuvette reached the desired temperature. A total of 3 replicates were conducted. The excitation and emission spectra of LNPs were characterized via a spectrometer (Fluoromax-Plus-C, Horiba, Japan) using a 300 μL quartz cuvette (Hellma, Germany) with stir at 25 ˚C. The excitation spectrum was scanned from 650 – 810 nm with an 830 nm LP emission filter and an emission recording wavelength at 850 nm. The emission spectrum was acquired using a 530 nm excitation light with a 550 nm LP emission filter (Semrock, USA) and recorded from 650 – 850 nm. A total of three replicates were conducted.

2.3 USF Imaging: Tube Model and Depth-study

The setup of the frequency-domain USF imaging system was demonstrated in previous published work [19]. The effectiveness of the LNPs for USF imaging was evaluated using a tube phantom model. Briefly, a silicone tube (ST 60-011-01, Helix Medical, USA) with an inner diameter of 0.31 mm and an outer diameter of 0.64 mm was fixed at the bottom of a silicone phantom, which had a thickness of 0.8 cm. Then, the tube was immersed in a 37 ˚C water tank to mimic the body temperature. The USF imaging was conducted with various-sized LNPs mixed with either DI water or mouse blood serum (1:1 v/v). The mixture was injected into the tube and waited for 10 min to equilibrate the temperature. A 2.5 MHz HIFU transducer (H-108, Sonic Concepts Inc., USA) was mounted at the bottom of the water tank and focused on the silicone tube. The HIFU transducer was used to elevate

the temperature and switch ON the LNPs within the focal volume. The estimated HIFU power used during USF imaging was 0.19 W and the MI was 0.97. The scan area was 5.08 mm × 5.08 mm and the step sizes were 2.54 mm and 0.254 mm in the X and Y directions, respectively. A 785 nm laser (MDL-III-785-2W, CNI, China) was utilized as the excitation light (121 μW/cm2) and filtered through a 785/62 nm band-pass filter (Semrock, USA). The excitation light intensity was measured with the power and energy meter (PM100D, Thorlabs, Germany). The emission light was collected using a fiber bundle and passed through one 830 nm absorption filter (Semrock, USA) and two 830 nm LP filters before being collected by a photomultiplier tube (H7422-20, Hamamatsu, Japan). A total of three replicates were conducted.

A depth-study was conducted with the tube model with different thicknesses (1.0 cm and 2.5 cm) of chicken breast tissue stacked on top of the phantom. Similarly, various-sized LNPs were injected into the tube and conducted USF imaging with the same scan area and step sizes. The HIFU power was 0.77 W (MI: 1.93) and the laser intensity was 544 μW/cm2 and 7.6 mW/cm2 for USF imaging at 1.0 cm and 2.5 cm thicknesses, respectively. A total of three replicates were conducted.

2.4 Release Test and Encapsulation Efficiency

The HIFU triggered release test was conducted by adding 500 μL ICG-encapsulated LNPs into a cylindrical vessel with the bottom sealed with parafilm and the top enclosed with a rubber stopper. Then, the vessel was immersed in a 37 ˚C water bath. A 2.5 MHz HIFU transducer was fixed at the bottom of the water tank and focused on the LNPs solution. A

pulsed cycle (pulse repetition period: 15s, pulse on: 400 ms) was generated using a function generator (33500B, Agilent, USA) and amplified by a 50 dB-gain radio frequency power amplifier (A075, E&I, USA). Three different HIFU powers of 0.19 W (MI: 0.97, P1), 1.74 W (MI: 2.90, P2), and 4.82 W (MI: 4.83, P3) were implemented to break LNPs. A two-dimensional scan was conducted using a three-axis motorized translational stage (XSlide™ and VXM™, Velmex Inc., USA). The scanning area was 5.08 mm x 5.08 mm with a step size of 0.508 mm in both X and Y directions. After scanning, the LNPs solution was transferred into a 1.5 mL microcentrifuge tube and centrifuged at 10,000 ×g for 45 min at 4 ˚C. The intact LNPs were sedimented at the bottom and the released ICG was dispersed in the solution, which was then transferred into a 300 μL quartz cuvette and the fluorescence intensity was measured using the Fluoromax-Plus-C spectrometer. In addition, to study the effects of HIFU exposure time on breaking LNPs, the scan using HIFU power of 4.82 W was repeated for 5 times (P4). To exclude the effect of temperature on LNPs' destruction and pre-existing free ICG influence, a negative control, which was not exposed with HIFU, was kept at 37 ˚C with a corresponding scanning time. More, the LNPs were completely broken with a sonic dismembrator (FB505, Fisher Scientific, USA) using 20 % power and 30 % duty cycle for 3 minutes in an ice bath. The measured fluorescence intensity of the completely broken LNPs was the positive control (100 % release). For all release tests, the ultrasound triggered content release percent was quantified using Equation 2.

$$\text{HIFU Triggered Release \%} = \frac{\text{S}-\text{NC}}{\text{PC}-\text{NC}} \times 100\% \qquad \textbf{Equation 2}$$

S: fluorescence intensity of sample, counts

NC: fluorescence intensity of negative control, counts

PC: fluorescence intensity of positive control, counts

The ICG encapsulation efficiency was calculated via Equation 3. First, the unencapsulated ICG was separated from the LNPs via centrifugation. Then, a spectrometer was utilized to acquire the fluorescence intensity of the unencapsulated ICG. Meanwhile, an ICG aqueous solution, which had the same concentration used during LNPs synthesis (0.016 mg/mL), was prepared and the fluorescence intensity was measured.

$$\text{Encapsulation Efficiency } \% = \left(1 - \frac{\text{Unencapsulated ICG}}{\text{ICG solutoin}}\right) \times 100\% \qquad \textbf{Equation 3}$$

The number of replicates for both HIFU triggered release and encapsulation efficiency were 5.

3. Results

The ICG-encapsulated and thermosensitive liposomes were synthesized via the hydration method, and the size of the liposomes was controlled via an extrusion approach. To evaluate the USF imaging feasibility of the LNPs, the fluorescence intensity profile was studied. Factors such as background fluorescence intensity, lower critical solution temperature (LCST), fluorescence intensity on-to-off ratio, absolute fluorescence intensity change, and transition temperature range are critical to assessing the contrast agent. The profile of fluorescence intensity change with respect to the change in temperature is shown in Figure 19a and 19b for both filtered and unfiltered liposomes. It is clear to state that the fluorescence intensity gradually increases first, followed by a sharp upsurge within the transition temperature range, which was related to the size decrease of liposomes (Figure

20), and finally levels off. The shapes of the fluorescence intensity profiles were similar, although the sizes of liposomes were different. A linear relationship between the hydrodynamic size measured with the DLS and the filter size used during extrusion is indicated in Figure 19c. After extrusion with 30, 50, 100, and 200 nm filters, the resultant LNPs had hydrodynamic sizes of 82.3, 94.0, 117.7, and 162.4 nm, respectively. According to Figure 19d, smaller liposomes tended to have stronger background fluorescence. Figure 19e shows that the filtered LNPs had lower LCSTs at around 38.8 ˚C while the unfiltered liposomes had an LCST at 40.4 ˚C. The on-to-off ratio with respect to the size of liposomes is presented in Figure 19f, and no obvious difference was observed between various-sized liposomes. The absolute fluorescence intensity difference between switching ON and OFF is one of the key factors that determines the potential USF imaging depth of contrast agents. An obvious decrease in absolute fluorescence intensity difference is recognized as the size of liposomes increases (Figure 19g). Figure 19h reveals that small liposomes had a higher transition temperature range compared to large liposomes.

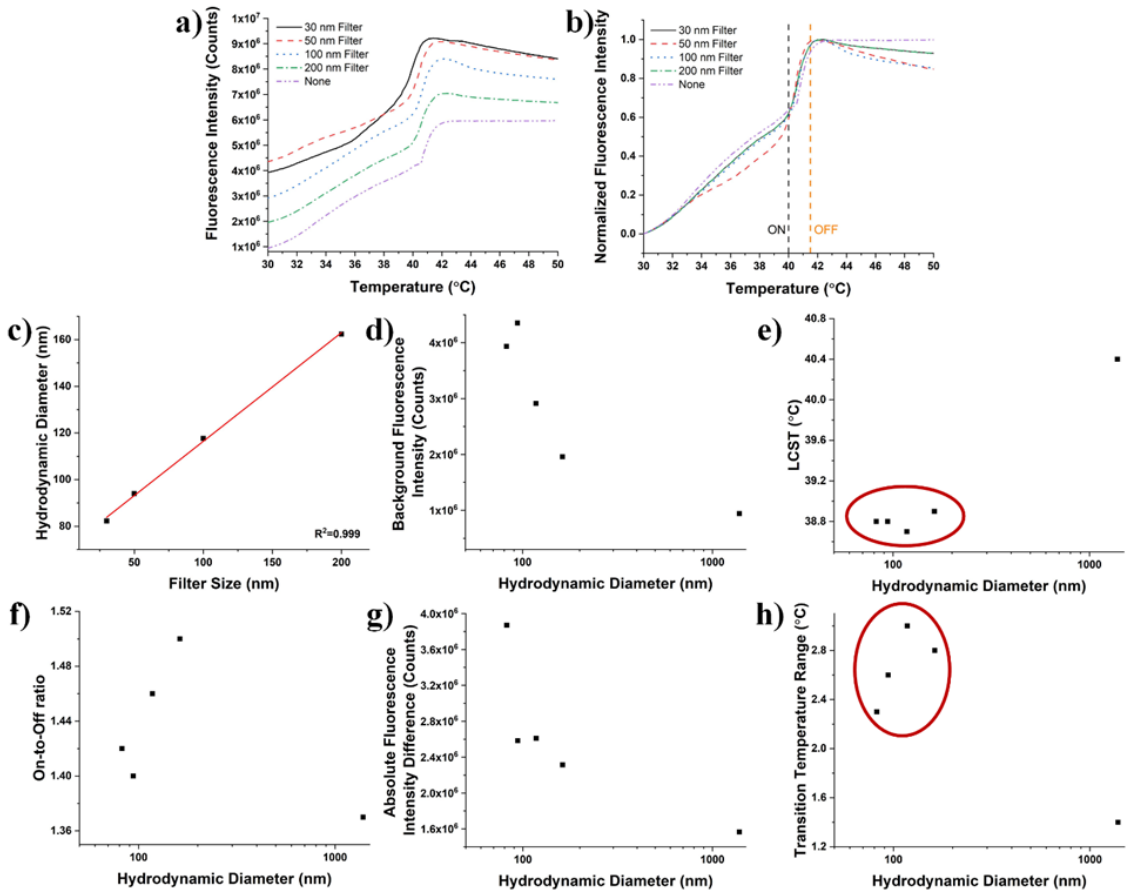

Figure 19. The fluorescence intensity profile of ICG-encapsulated and temperature-sensitive liposomes. a) The profile of the emitted fluorescence intensity changes responding to the change of temperature for all-sized liposomes. b) Normalized fluorescence intensity changes with respect to the change of temperature. c) The relationship between the hydrodynamic size of liposomes and filter size utilized during extrusion. d) The background fluorescence intensity of various-sized liposomes. e) The LCST of liposomes with different sizes. f) The correlation between the on-to-off ratio and the size of liposomes. g) The absolute fluorescence intensity difference between switched on/off for various-sized liposomes. h) The differences in the transition temperature range of different-sized liposomes.

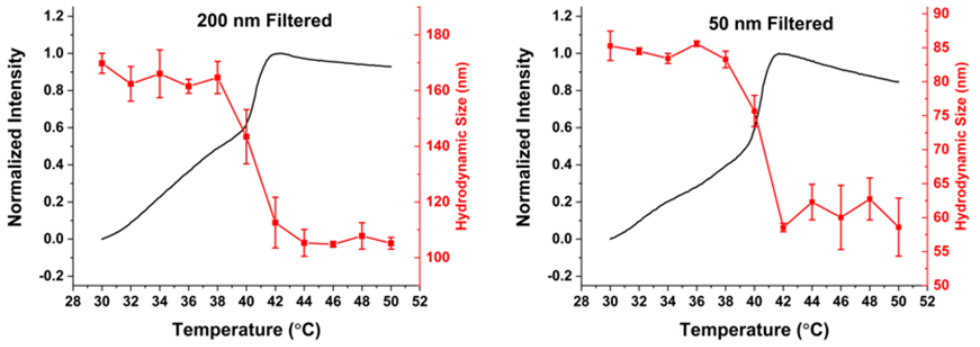

Figure 20. The relationship between the fluorescence intensity of 200 nm and 50 nm filtered LNPs and the temperature (Black line). Temperature dependent size change (red line). A total of replicates n = 3.

Since ICG dye is very easily oxidized, examining the spectrum of synthesized liposomes is necessary to understand the status of the encapsulated ICG dye. The excitation and emission spectra of LNPs were shown in Figure 21 b and c, respectively. Apparently, the size of LNPs does not affect the spectra. In addition, compared to the spectra of ICG aqueous solution (Figure 21a), a slight red shift can be noted for the emission peak of LNPs from 809 nm to 831 nm.

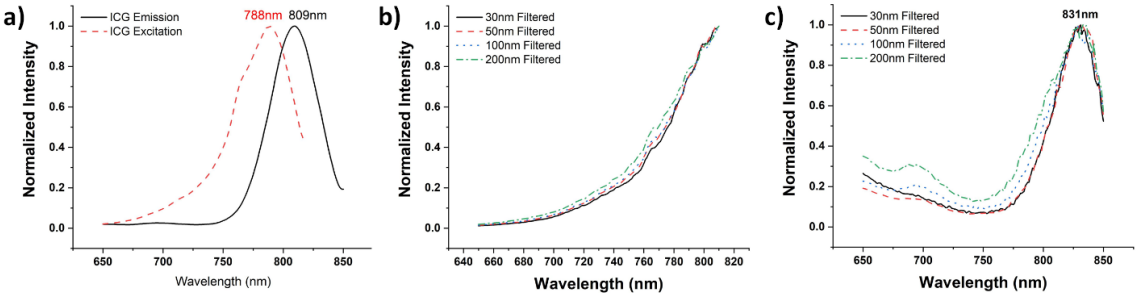

Figure 21. a) Excitation and emission spectra of ICG aqueous solution. b) Excitation spectrum and c) emission spectrum for various-sized LNPs.

It is vital to have a stable USF contrast agent for both *ex vivo* and *in vivo* applications. The KCl aqueous solution was utilized to mimic the physiological ionic strength with various concentrations. As shown in Figure 22a, 22b, 22c, and 22d, the shape of the fluorescence intensity profile remains unchanged in different concentrations of KCl compared to that of the liposome solution in 0 mM KCl, which indicates that LNPs were stable in solution with different ionic strengths. In addition, the pH level varies in different human body fluids and tissues [58]. Therefore, it is essential to study the stability of LNPs in solutions with different pH values. Figure 22e, 22f, 22g, and 22h demonstrate that LNPs were stable within a pH range from 5.2 to 9.2.

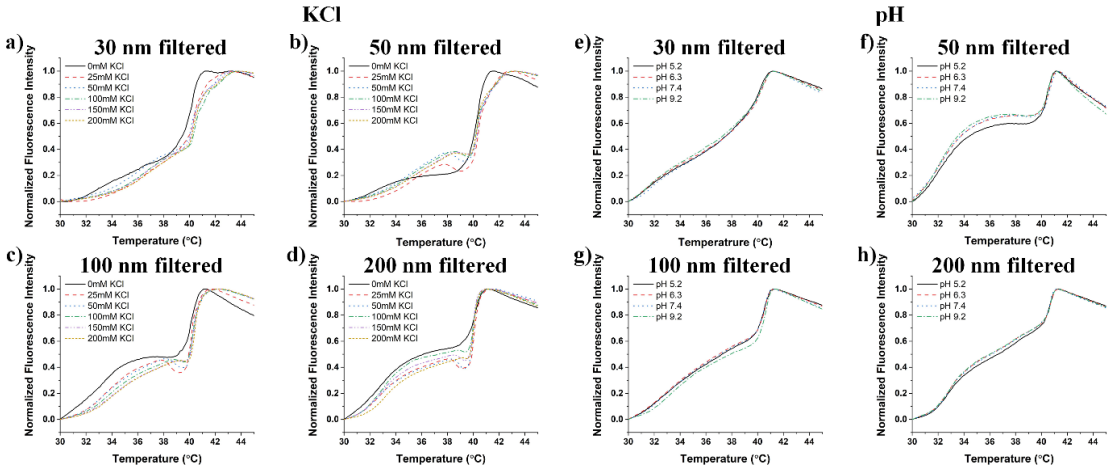

Figure 22. The effect of ionic strength (KCl) on the stability of a) 30 nm, b) 50 nm, c) 100 nm, and d) 200 nm filtered LNPS. The effects of pH on the stability of e) 30 nm, f) 50 nm, g) 100nm, and h) 200 nm filtered LNPs. Number of replicates n = 3.

To further understand the USF imaging performance of LNPs in physiological conditions, LNPs were mixed with blood serum to conduct both the cuvette test and USF imaging with

a tube phantom model. The cuvette system measured results in Figure 23 show that after mixing with blood serum, the LCST slightly shifted to the left at around 37 ˚C and the absolute fluorescence intensity difference between switch-ON/OFF increased. After mixing the LNPs with water, the USF imaging results indicated 30 nm and 100 nm filtered LNPs had a stronger intensity compared to that of 50 nm and 200 nm filtered LNPs. After mixing the LNPs with blood serum, 30 nm LNPs were shown to have the highest USF signal intensity.

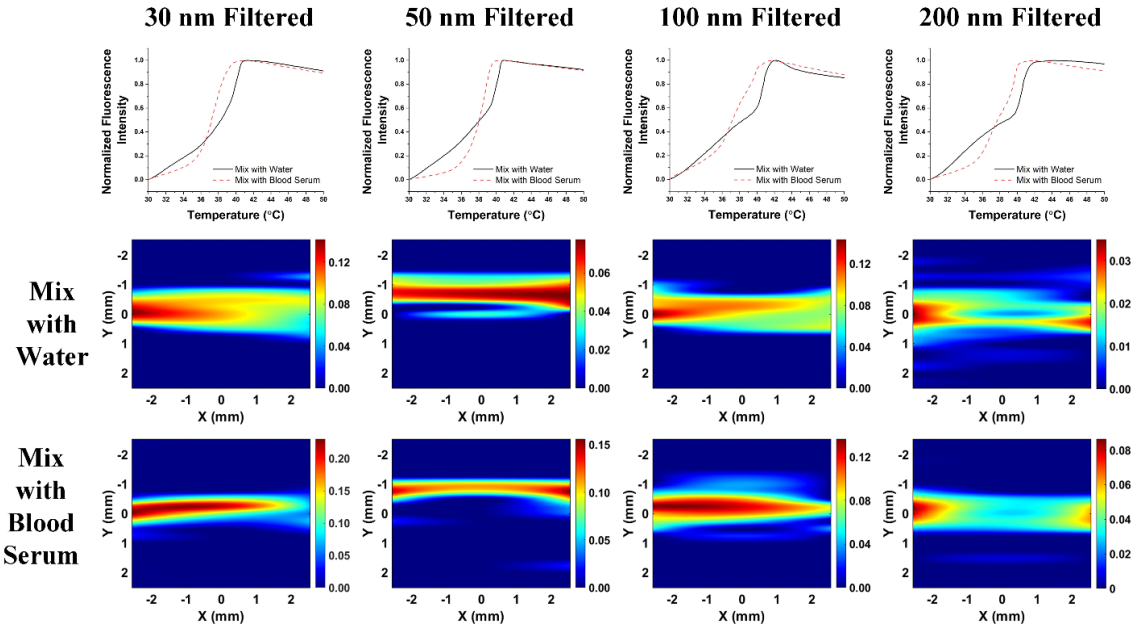

Figure 23. The fluorescence intensity profile was measured with the in-house built cuvette system and USF imaging for different-sized LNPs mixed with either water or blood serum inside a silicone tube embedded phantom model. Number of replicates n = 3.

Based on cuvette results reported in Figure 19 and USF imaging results presented in Figure 23, different-sized liposomes resulted with various USF imaging signal strengths. A depth-

study was conducted to compare USF imaging signal strength at both 1.0 cm and 2.5 cm for filtered LNPs and unfiltered liposomes. Figure 24a and 24b exhibit images of 1.0 cm and 2.5 cm thick chicken breast tissues stacked on a silicone tube embedded phantom, respectively. Figure 24c indicates that 30 nm LNPs had the highest USF signal strength, while un-filtered liposomes had the lowest USF signal strength. After increasing the thickness from 1.0 cm to 2.5 cm, we can barely see the USF signal from the un-filtered liposomes but still recognize USF signals from all LNPs. Again, 30 nm LNPs were confirmed to have the strongest USF signal strength at 2.5 cm.

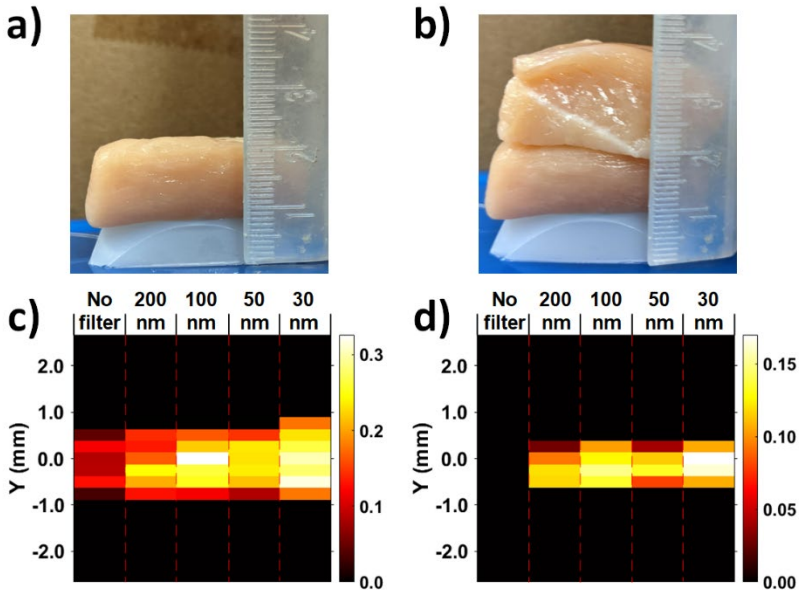

Figure 24. Depth-study of various-sized liposomes for USF imaging. The image of a 0.8 cm thick tube phantom was stacked with a) 1.0 cm and b) 2.5 cm thick chicken breast tissue. USF imaging of various-sized liposomes at c) 1.0 cm and d) 2.5 cm. Number of replicates n =3.

The combination of USF imaging with ultrasound-controlled content release opens possibilities for applications such as monitoring the accumulation of liposomes in the centimeter-deep tissue using USF imaging and breaking liposomes to release encapsulated drugs with the help of HIFU when desired. Therefore, the study of encapsulation efficiency and HIFU triggered release with various HIFU powers is in demand. As presented in Figure 25a, larger-sized LNPs (100 nm and 200 nm filtered) had a higher encapsulation efficiency of more than 80 %, while the smaller-sized LNPs (30 nm and 50 nm filtered) possessed an encapsulation efficiency of 60 %. For HIFU triggered release tests, four HIFU power conditions were tested. Condition P1 mimicked the HIFU power used during USF imaging. According to Figure 25b, 7.38 ± 1.85 % release was observed for 50 nm filtered LNPs in condition P1 and the ICG release for 200 nm filtered LNPs can be neglected. After increasing HIFU powers, we can clearly see the ICG release increased to 13.47 ± 2.36 % (condition P2) and 24.56 ± 5.92 % (condition P3) for 50 nm filtered LNPs and 4.53 ± 2.69 % (condition P2) and 5.09 ± 1.07 % (condition P3) for 200 nm filtered LNPs. The results state that by increasing the HIFU power, we can achieve higher ICG release. Furthermore, instead of increasing the power of HIFU, extend the HIFU exposure time to 5 times more and keep the HIFU power the same as condition P3 can also increase the ICG release dramatically (condition P4). The ICG release reached 48.01 ± 11.76 % and 9.17 ± 3.85 % for 30 nm and 200 nm filtered LNPs, respectively. In general, 50 nm filtered LNPs had a higher release than the 200 nm filtered LNPs.

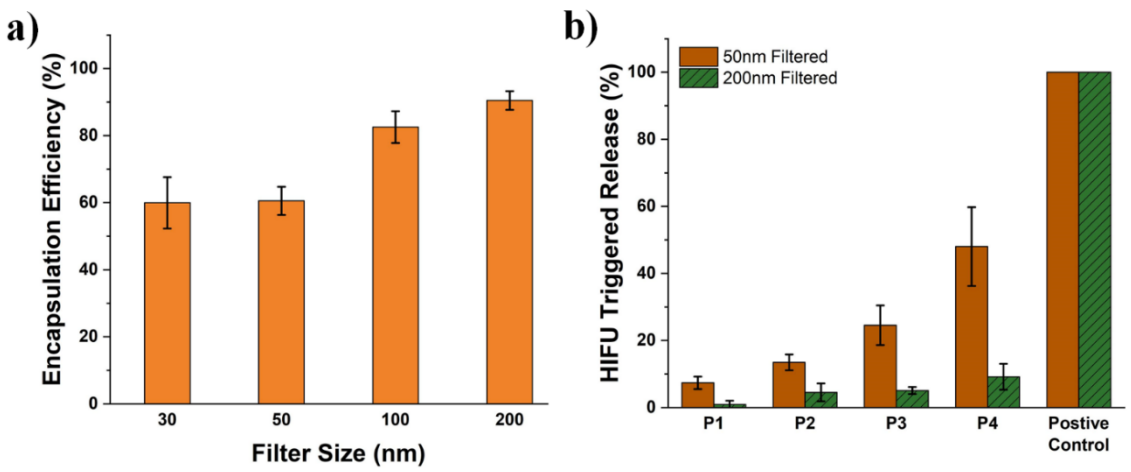

Figure 25. a) ICG encapsulation efficiency of various-sized LNPs. b) HIFU induced ICG release for 50 nm and 200 nm filtered LNPs. HIFU power conditions used during the release test included P1: 0.19 W (MI 0.97), P2: 1.74 W (2.90), P3: 4.82 W (MI 4.83), and P4: 4.82 W (MI 4.83; repeated 5 times).

4. Discussion

The contrast agents used for USF imaging have constraints on both dyes and vesicles. First, the dye should be polarity sensitive while having a high quantum yield in a low polarity environment and a low quantum yield in a high polarity environment [17]. Next, the vesicle used to encapsulate the dye needs to be temperature sensitive so that the vesicle will shrink when the temperature increases and create a relatively low-polarity environment to increase the fluorescence intensity of the dye. In addition, as the vesicle is flexible enough to change size with respect to the change in temperature, the vesicle should also be stable enough so that increasing temperature, exposing it to ultrasound mechanical force, and exposing it to the physiological environment will not break it. Unilamellar LNPs have numerous advantages over multilamellar liposomes, including the ability to cross biological barriers

such as the blood-brain-barrier [59] and excellent enhanced permeability and retention effect for passive accumulation in tumor cells [60]. In addition, LNPs within 20 – 200 nm exhibit better cellular targeting efficiency and LNPs are also favored for vaccine application since only liposomes in the nanometer range can reach lymph nodes and directly contact B cells [61]. These properties of LNPs provide potential applications such as targeted USF imaging in both brain and tumor. Therefore, LNPs were synthesized, and the eligibility for USF imaging was also assessed. Despite the fact that LNPs have extensive advantages compared with micro-sized liposomes, LNPs are considered more vulnerable due to their single bi-layer structure. The polyethylene glycol chain can be decorated on the surface of LNPs to improve stability by preventing self-aggregation and prolonging circulation time [62,63].

The formulated LNPs had a higher absolute fluorescence intensity change between switching ON and OFF compared to those of unfiltered liposomes. This indicates that LNPs tend to have a stronger USF signal strength and are therefore suitable for deeper USF imaging, which was confirmed by the depth-study. Although unfiltered liposomes were eligible for USF imaging at 1 cm with reasonable signal strength, LNPs had greater USF signal strength and can be used for USF imaging at 2.5 cm. Additionally, LNPs had an LCST of around 38.8 ˚C, which was closer to the body temperature than the LCST (40.4 ˚C) of unfiltered liposomes. This is beneficial for potential *in vivo* USF imaging since less HIFU energy is required to switch ON the contrast agent, making it safer to implement. The background fluorescence intensity of LNPs was found to be higher than that of unfiltered liposomes. This could be useful when fluorescence imaging is needed first to

roughly localize the region of interest. In addition, the emission peak of LNPs shifted from 809 nm to 831 nm, which is desired since the tissue absorption and autofluorescence interference are minimized.

The ability to monitor the accumulation and release status of liposomes in the centimeter-deep tissue is valuable. The combination of USF imaging with ultrasound-controlled release offered an opportunity to achieve this goal. LNPs were shown to be stable enough and eligible for USF imaging in a tube model after mixing with blood serum, using a HIFU power of 0.19 W (MI 0.97). This HIFU power only caused a 7.38 % and a 0.89 % release of ICG for 200 and 50 nm LNPs, respectively. Higher release quantities could be attained by either increasing the HIFU power or the HIFU exposure time. Thus, implementing USF imaging to monitor the accumulation of LNPs and initiate release by adjusting HIFU intensity and exposure time is feasible. In addition, the size effect on the release percentage and loading efficiency was observed. A trade-off was expected as larger-sized LNPs (200 nm filtered) had a higher encapsulation efficiency but a lower release percentage and vice versa for smaller-sized LNPs (50 nm filtered). Thus, larger-sized LNPs were more suitable for content that required the slow release, but the high encapsulating quantity and smaller-sized LNPs were applicable for content that required quick and sudden release in low quantity.

This study confirmed the feasibility of combining USF imaging with ultrasound-controlled release using LNPs. The developed LNPs have strong USF signals for deep tissue USF imaging, LCSTs close to body temperature, and a NIR emission spectrum. However, the

stability and shelf-life were reduced compared to unfiltered liposomes. Sugars, such as sucrose and isomaltose, could be added to the liposome solution for possible better preserving practices [64]. This study also led to numerous potential future research projects, such as *in vivo* folate-targeted USF imaging and ultrasound-controlled drug release for tumor imaging and treatment.

5. Conclusion

The thermosensitive and PEGylated liposomes encapsulated with ICG were first implemented for USF imaging and various sizes of LNPs were characterized. Compared to micro-sized liposomes, LNPs had an LCST shifted to around 38 ˚C and the transition band width increased to more than 2.5 ˚C. The fluorescence intensity profile indicates that smaller LNPs had higher fluorescence and a stronger absolute fluorescence intensity change after switching ON. LNPs also showed outstanding physiological stability in solution with various ionic strengths and pH values, and USF imaging was successfully conducted with the mixture of LNPs and blood serum. In addition, a depth-study showed USF imaging could be conducted with both micro and nano-sized liposomes at 1.0 cm, but USF imaging at 2.5 cm could only be conducted with nano-sized liposomes. Moreover, the feasibility of combining USF imaging with ultrasound-controlled release was verified in this study. While negligible release was noticed during USF imaging with a HIFU power of 0.19 W (MI: 0.97), increasing the HIFU power and extending the exposure time could lead to an obvious increase in release. Above all, this research suggests that the LNPs could be used for high-resolution USF imaging-guided and ultrasound-controlled drug release in centimeter-deep tissue.

Chapter 5

Gold Nanoparticles and ICG-loaded PNIPAM Nanogels for Computed Tomography and Ultrasound-Switchable Fluorescence Dual Modality Imaging.

1. Introduction

Fluorescence imaging has been widely used in both research studies and clinical applications. Recently, researchers developed a cubic-phase erbium-based rare-earth nanoparticle for *in vivo* molecular imaging and immunotherapy [65]. The emission light in the NIR range allows them to have a high-resolution image. Except using fluorescence imaging for research, it has also been widely used for imaging guided surgery [7,66]. Since ICG dye is an FDA approved contrast agent to be used for *in vivo* applications, fluorescence guided surgery using ICG is studied to increase survival rate, less tissue damage, and improve safety [67].

The CT imaging scan is one of the useful diagnostic imaging tools to create a detailed 3-D image of internal organs, bones, and soft tissues. The usage of CT for tumor identification, tracking, and monitoring was favored due to its fast, painless, and accurate imaging. The use of contrast agents during CT scan improved target-to-background contrast and specification. Iodine-based CT contrast agents were widely used to enhance CT images and were usually injected via a vein. The other commonly used contrast agent is Barium-sulfate, which is usually taken by mouth. Recently, using AuNPs as a contrast agent for CT scans has attracted lots of attention due to its high X-ray attenuation, simple surface chemistry, and easy surface decoration [68–71].

This chapter synthesized an AuNPs and ICG-loaded PNIPAM (AuNP-ICG-PNIPAM) nanogel for CT and USF dual-modality imaging. We conducted nanogel characterizations include size measurement using DLS and TEM, zeta potential, effect of temperature on fluorescence emission, temperature-dependent size measurement, stability tests, and spectra. The results showed that the nanogel has a size of around 200 nm and the encapsulated AuNP has a size of around 10 nm. The fluorescence profile confirmed that the emitted fluorescence intensity increases with an increase in temperature, and the switch-ON position was at 37.5 ˚C. We conducted an *ex vivo* study with a tissue model to verify the CT contrast, followed with CT and USF imaging in a silicone tube model to verify the imaging capability. Finally, we injected the AuNP-ICG-PNIPAM into the thigh of a mouse and successfully conducted CT and USF imaging.

2. Materials and Methods

2.1 Synthesis of AuNP and ICG-loaded PNIPAM Nanogel

In Figure 26, the schematic diagram of the process of synthesizing the AuNP-ICG-PNIPAM nanogel was presented.

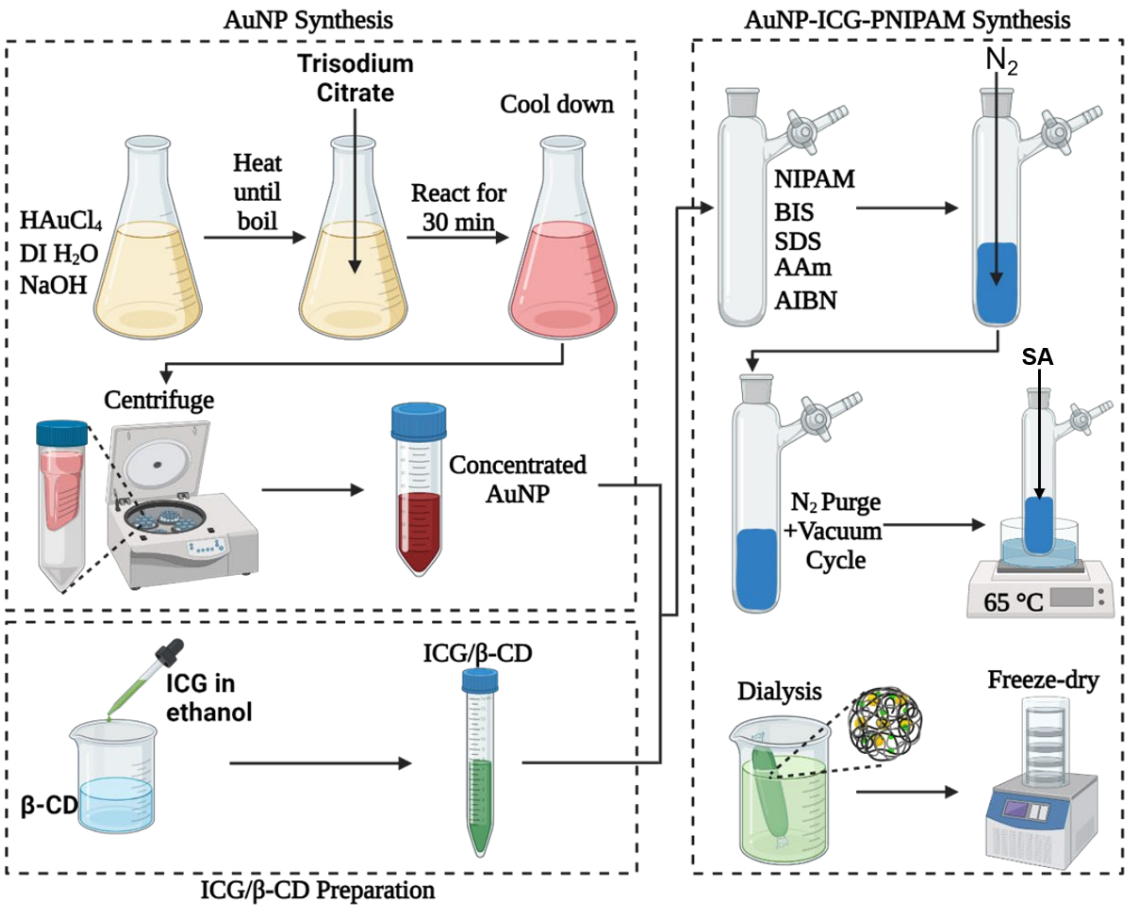

Figure 26. The schematic diagram of AuNP-ICG-PNIPAM nanogel synthesis. Three major steps, including the AuNP synthesis, ICG/β-CD preparation, and AuNP-ICG-PNIPAM nanogel synthesis, were demonstrated.

2.1.1 AuNP synthesis

The synthesis of AuNP is based on the Turkevich method with some modifications [72]. In brief, 90 mL of DI water was added to a 250 mL Erlenmeyer flask. Then, 7.7 mL of sodium hydroxide aqueous solution (7.7 mM) was added to the flask to adjust the pH. Next, 2.5 mL of gold (III) chloride trihydrate solution (2.5 mM) was transferred to the flask. The flask with the mixture was then placed on a hotplate and heated at 250 ˚C until boiling,

with a stir at 800 rpm. A reflux was placed on top to avoid the escape of water vapor. 2.851 mL of trisodium citrate solution (50 mg/mL) was then injected into the flask quickly. Trisodium citrate can not only reduce Au^{3+} to gold nanoparticles but also act as a stabilizing agent to avoid aggregation. After adding the trisodium citrate, the color of the solution in the flask changed from golden yellow to wine red. The reaction took place for 30 minutes and then cooled down to room temperature. Synthesis was repeated 3 times to acquire a total volume of about 300 mL of gold nanoparticle solution. Next, gold nanoparticle solution was transferred to four 50 mL ultra-centrifugal filter tubes (MWCO 10kDa) and centrifugation was conducted using a refrigerated centrifuge (Multifuge X1, Thermo Scientific, USA) with a rotor (Fiberlite F15, Thermo Scientific, USA) for 10 min at 1,500 ×g and 4 ˚C. The centrifugation process was repeated until the final volume of AuNP reached 50 mL. Finally, the AuNP solution was stored at 4 ˚C.

2.1.2 AuNP and ICG-loaded PNIPAM nanogel synthesis

Synthesis of PNIPAM nanogel followed the procedures mentioned in our previous study with some modifications [73]. The beta-cyclodextrin (β-CD)/ICG complex was synthesized first. 4.5 mg of ICG was dissolved in 3 mL anhydrous ethanol with the help of bath sonication for 5 minutes. At the same time, 17 mg β-CD was dissolved in 10 mL of DI water. Then, the ICG solution was added into the β-CD solution dropwise with a stir. The mixture was mixed for six hours. A reaction tube was filled with 1.5 g NIPAM (monomer), 0.15g AAm (adjusting Switch-ON temperature point), 22 mg BIS (linker), 150 mg SDS (surfactant), 40 mL of concentrated AuNP solution, 13 mL of β-CD/ICG mixture with 2 mL of washing DI water, and 50 mg of azobisisobutyronitrile (AIBN, initiator). The

mixture was stirred for 30 minutes to allow the complete dissolution of reagents. Then, the solution was purged with nitrogen for 1 hour while stirring. Afterward, a rubber stopper was used to seal the tube, followed by 3 cycles of vacuum and nitrogen purge to ensure a nitrogen-rich environment within the reaction tube. Next, the reaction tube was immersed in a pre-heated oil bath (65 ˚C) and reacted for 1.5 hours. During this period, 0.15 g sodium ascorbate (SA) was dissolved in 2 mL DI water. After 1.5 hours reaction, SA solution with 1 mL additional washing DI water was injected into the reaction tube using a 5 mL syringe and a 27-gauge needle. The total reaction time was 13 hours and dialysis against DI water was took place for 3 days. Dialysis water was changed every day. Freeze-dry was conducted for long-term storage and 150 mg/ml AuNP-ICG-PNIPAM was prepared in DI water for the following experiments.

All chemicals used in sections 2.1.1 and 2.1.2 were purchased from Fisher Scientific.

2.2 AuNP-ICG-PNIPAM Nanogel Characterizations

2.2.1 DLS and zeta potential

The hydrodynamic size of both AuNP and AuNP-ICG-PNIPAM nanogel was measured using the DLS (NanoBrook 90PlusPALS, Brookhaven Instruments, USA). For AuNP, the solution was diluted 10 times with DI water to avoid aggregation during measurement, and a 3.5 mL quartz cuvette was used to hold the sample. After that, the AuNP sample was placed in the DLS and allowed to settle for 10 minutes before being measured. Measurement was repeated five times to acquire the average hydrodynamic size of AuNP. Similarly, 1 mg/mL of AuNP-ICG-NIPAM solution was transferred into a 3.5 mL quartz

cuvette. The measurements were conducted at room temperature and repeated at least three times. The AuNP-ICG-PNIPAM nanogel size change with respect to the change in temperature was also measured with the DLS. The temperature was measured from 30 ˚C to 54 ˚C with an increment of 2 ˚C. The temperature was held for 10 min at each temperature point to allow equilibration before measuring.

The zeta potential was measured by transferring 1 mg/mL AuNP-ICG-PNIPAM nanogel into a 3.5 mL gold electrode quartz cuvette. Then, the PALS (NanoBrook 90Plus PALS, Brookhaven Instruments, USA) was used to conduct zeta potential measurements at room temperature. Measurement was repeated five times.

2.2.2 TEM

A TEM (H-9500, Hitachi, Japan) was used to measure the physical size and visualize the shape of AuNP and AuNP-ICG-PNIPAM nanogel. The AuNP solution for TEM was prepared by first diluting it 100x with DI water. A 200-mesh copper grid was fixed using forceps. A 10 µL AuNP solution was dropped on the grid and left overnight to allow complete solvent evaporation. Then, the sample was loaded into the TEM for imaging. Similarly, the PNIPAM nanogel was diluted by 30 times to avoid aggregation during imaging. A 10 µL PNIPAM nanogel was dropped on the grid and left overnight to allow complete solvent evaporation. Then, 5 µL of 0.5 % uranyl acetate was dropped on the grid to negatively stain the sample. After 2 hours to dry the sample, it was then placed in the TEM for imaging.

2.2.3 Absorption and emission spectra

The absorption spectra of both AuNP and AuNP-ICG-PNIPAM nanogel were characterized using a microplate reader (Tecan, Switzerland). 30x diluted AuNP solution and 4 mg/mL AuNP-ICG-PNIPAM were prepared. 200 μL sample was transferred into a 96-well plate for the absorption test. The spectrometer (Fluoromax-Plus-C, Horiba, Japan) was used to measure the emission spectrum of AuNP-ICG-PNIPAM. A 300 μL quartz cuvette (Hellma, Germany) was used to hold a 200 μL AuNP-ICG-PNIPAM sample (4 mg/mL). The cuvette was placed inside a holder with stirring and the temperature was set at 25 ˚C. The emission spectrum was scanned from 600 nm to 850 nm using an excitation light of 500 nm and an integration time of 0.1 s. A 550 nm long-pass filter (Semrock, USA) was used to avoid leakage of excitation light.

2.2.4 Fluorescence profile

An in-house built cuvette system was used to examine the relationship between the fluorescence intensity emitted from the AuNP-ICG-PNIPAM nanogel with respect to the change in temperature (fluorescence profile). The 3 mL AuNP-ICG-PNIPAM nanogel solution was diluted 10x before loading into a 3.5 mL quartz cuvette and placed in a temperature-controlled holder (Quantum Northwest, Inc., USA) with stirring. An 808 nm excitation laser (MGL-II-808-2W, Dragon lasers, China) was used to excite the sample. The emitted light from AuNP-ICG-PNIPAM nanogel was collected by a modular USB spectrometer (USB2000+, Ocean Inlight, USA) after passing through an 830 long-pass filter (Semrock, USA). The temperature measurement range was from 30 ˚C to 50 ˚C with an increment of 0.1 ˚C. A temperature probe was immersed in the sample to measure and

record the sample temperature. At the same time, fluorescence intensity values at various temperature points were recorded.

2.2.5 Stability test

The switch-ON/OFF cycle test was implemented using the in-house built cuvette system to determine the stability of the AuNP-ICG-PNIPAM. The temperature was set at 30 ˚C (switch OFF) at the beginning, and fluorescence intensity was recorded. Then the temperature was quickly increased to 50 ˚C (switch ON) and the fluorescence intensity was measured again. A total of 10 cycles were conducted to examine the stability of the AuNP-ICG-PNIPAM nanogel.

2.3 Ex vivo Imaging

2.3.1 CT imaging of AuNP

The CT imaging of AuNP was conducted to examine the capability of using it as a CT contrast agent. The micro-CT (Bruker, USA) was used during the experiment. First, AuNP was placed into a 1.5 mL centrifuge tube and CT imaging was conducted with the AuNP and porcine tongue tissue (1 cm thick). Acquired images were processed with NRecon to reconstruct the image and CTvox to acquire the 3-D CT image. In CTvox, the threshold can be adjusted to remove noise. In addition, AuNP and water were injected and sealed into two silicone tubes (0.76 mm inner diameter and1.65 mm outer diameter, HelixMark, USA), separately. Both tubes were embedded in one piece of porcine tongue tissue. A CT image was acquired with the micro-CT and the data was processed using NRecon and CTvox.

2.3.2 CT and USF imaging of AuNP-ICG-PNIPAM

The AuNP-ICG-PNIPAM solution was injected into a silicone tube (0.76 mm ID, 1.65 mm OD), which had a length of 1.1 cm. Two ends of the tube were sealed with glue to avoid leaking. A negative control with water injected into the tube was also implemented. Both tubes contained either AuNP-ICG-PNIPAM or water was embedded in 1.5 cm thick porcine tongue tissue. CT imaging was conducted using the micro-CT.

After embedding the tube in the porcine tissue, USF imaging was conducted using an in-house built frequency-based USF system. The porcine tissue was placed in a customized box with the bottom sealed with parafilm. The box was placed in a water tank filled with water and the temperature was controlled by a temperature controller (Stanford Research System, USA) at 37 ˚C. A laser light (27.87 mW/cm^2) was illuminated from the bottom of the tissue to excite the AuNP=ICG-PNIPAM. A 2.5 MHz HIFU transducer (Sonic Concepts Inc., USA) was placed at the bottom of water tank and focused on the silicone tube, which was embedded in the porcine tissue, to induce heat and switch ON the nanogel. a HIFU power of 0.20 W (MI = 0.97) was used during a 2-D scan with a scan area of 7.112 mm × 7.112 mm and a step size of 0.356 mm in the Y direction and 1.778 mm in the X direction. The burst period is 20 s with a 0.4 s burst. The emitted fluorescence was collected by a fiber bundle located on top of the tissue and passed through two 830 nm long-pass filters and one 830 nm absorption filter before reaching the PMT detector (Hamamatsu, Japan).

2.4 In vivo CT and USF Imaging

The animal protocols were approved by the University of Texas at Arlington's Animal Care and Use Committee. Three BALB/c mice (female, Jackson Lab, USA) were utilized to study the *in vivo* imaging capability of AuNP-ICG-PNIPAM nanogel. First, the mouse was shaved, and the thigh was exposed. A CT scan was conducted with the mouse as a negative control. Then, 50 μL nanogel was directly injected into the thigh muscle, and the mouse was imaged with CT again. Afterward, the mouse was transported to a customized bed. The bottom of the bed was sealed with parafilm and placed in a water bath with a temperature kept at 37 ˚C. A 3-D USF scan was conducted with a scan dimension of 8.128 mm × 8.128 mm × 6.350 mm in the X, Y, and Z directions, respectively. The step sizes were 1.016 mm × 1.016 mm × 1.270 mm in the X, Y, and Z directions, respectively. A HIFU with 2.50 W (MI = 3.38) power and a 0.4 s burst with a 20 s burst period was used to switch ON the nanogel. An excitation light with an intensity of 19.23 mW/cm^2 was utilized to excite the nanogel. Three replicates were conducted to verify the success in vivo CT and USF dual modality imaging. The imaging reconstruction and co-registration were conducted according to a previously published method [21].

The mouse was anesthetized with the anesthesia machine (Supera Anesthesia Innovations, USA) during both CT and USF imaging. During CT imaging, 3.0 % isoflurane (Miller Veterinary Supply, USA) and a flow rate of 1 L/min were implemented. During USF imaging, 1.8 % isoflurane and a flow rate of 0.8 L/min were used.

3. Results

3.1 Characterizations of AuNP-ICG-PNIPAM Nanogel

The hydrodynamic size of AuNP was characterized using a DLS. The result in Figure 27a1 shows that AuNP has a mean diameter of 24.2 ± 0.2 nm with a polydispersity of 0.147 ± 0.026. Further characterization with TEM revealed a round-shaped size and a homogenous size distribution as shown in Figure 27a2. The hydrodynamic size of AuNP-ICG-PNIPAM was also measured using the DLS. At 30 ˚C, the nanogel has a hydrodynamic size of 122.5 ± 20.8 nm and the hydrodynamic size decreased to 51.7 ± 2.6 nm when the temperature reached 46 ˚C. The nanogel has a relative homogenous size distribution of 0.171 ± 0.081 at 30 ˚C. As shown in Figure 27b1, the size of the nanogel started to decrease after 36 ˚C. In addition, the emitted fluorescence intensity change with respect to the change in temperature was shown in Figure 27b1. It is clear that the fluorescence intensity increased around 37 ˚C and leveled off around 45 ˚C. This fluorescence intensity change corresponded to the size change of the AuNP-ICG-PNIPAM nanogel. Figure 27b2 shows a single AuNP-ICG-PNIPAM nanogel, which had AuNPs entrapped inside or attached to the surface. The zeta potential of the AuNP-ICG-PNIPAM at 30 ˚C showed that the nanogel had a relative net neutral charge on the surface with a value of 1.64 ± 0.75 mV. The absorption spectra for AuNP, ICG-PNIPAM, and AuNP-ICG-PNIPAM were shown in Figure 27d and measured from 500 nm to 800 nm. AuNP (shown in the black solid line) had an absorption peak of 520 nm. The absorption peak of ICG-PNIPAM (shown in the red dash line) was located at 770 nm. The AuNP-ICG-PNIPAM nanogel was shown to have two absorption peaks at 520 nm and 770 nm (shown in the purple dotted line). The

emission spectrum of AuNP-ICG-PNIPAM nanogel was scanned from 550 nm to 850 nm. Two emission peaks were detected, which were at 604 nm and 800 nm.

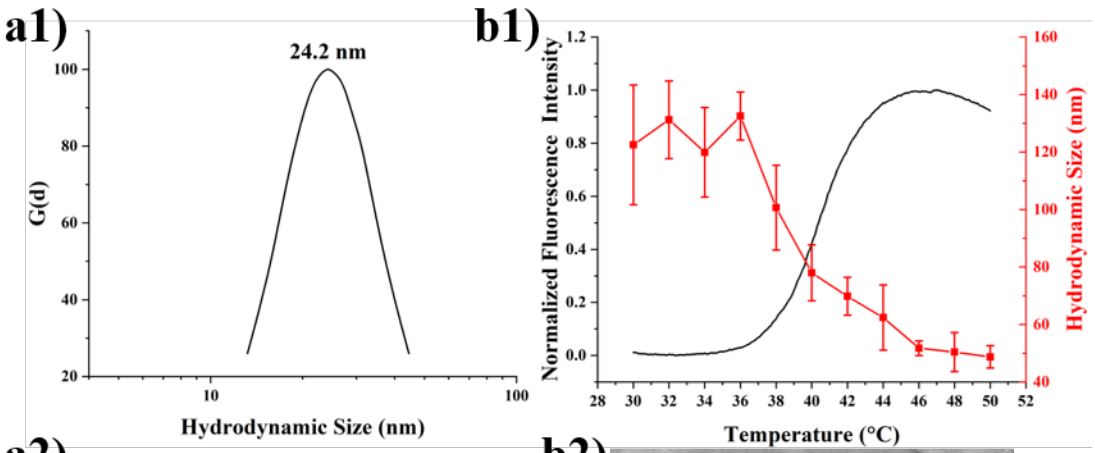

c)

	AuNP	AuNP-ICG-PNIPAM
Hydrodynamic Size at 30 ˚C (nm)	24.2 ± 0.2 nm	122.5 ± 20.8 nm
Hydrodynamic Size at 46 ˚C (nm)	-	51.7 ± 2.6 nm
Polydispersity Index	0.147 ± 0.026	0.171 ± 0.081
Zeta Potential (mV)	-	1.64 ± 0.75

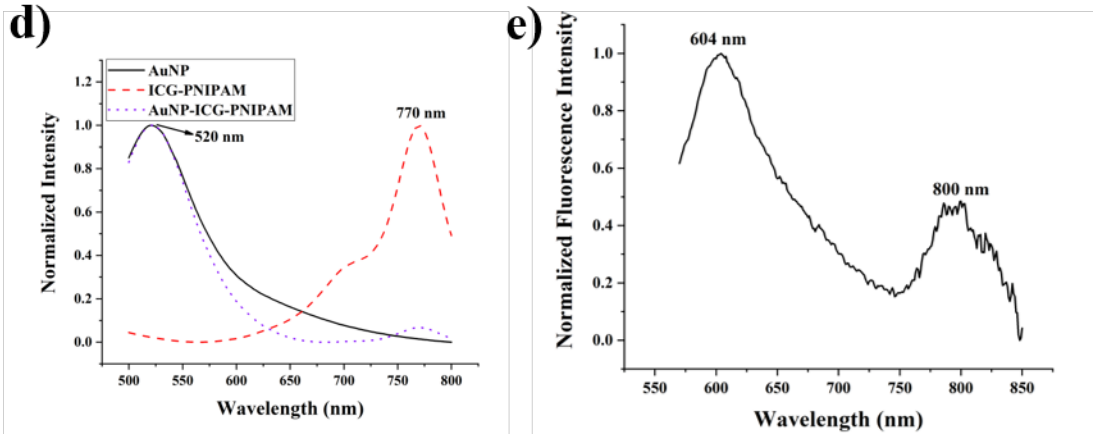

Figure 27. Characterizations of AuNP and AuNP-ICG-PNIPAM nanogel. The size of AuNP was measured with a1) DLS (replicates n = 5) and a2) TEM with a scale bar of 20 nm. b1) The hydrodynamic size change and emitted fluorescence intensity change of AuNP-ICG-PNIPAM with respect to the change of temperature (replicates n = 5). b2) TEM image of a single AuNP-ICG-PNIPAM nanogel, which encapsulated AuNP with a scale bar of 100 nm. c) Summary of size, polydispersity, and zeta potential for both AuNP and AuNP-ICG-PNIPAM. Zeta potential values were measured with replicates n = 5. d) Absorption spectrum of AuNP (black solid line), ICG-PNIPAM (red dash line), and AuNP-ICG-PNIPAM (purple dotted line). e) The emission spectrum of AuNP-ICG-PNIPAM.

3.2 Stability

As shown in Figure 28, AuNP-ICG-PNIPAM nanogel was tested with the switch-ON/OFF test to determine its stability for USF imaging. A total of 5 cycles were conducted, and the result showed the nanogel was stable after five cycles of switching ON and OFF.

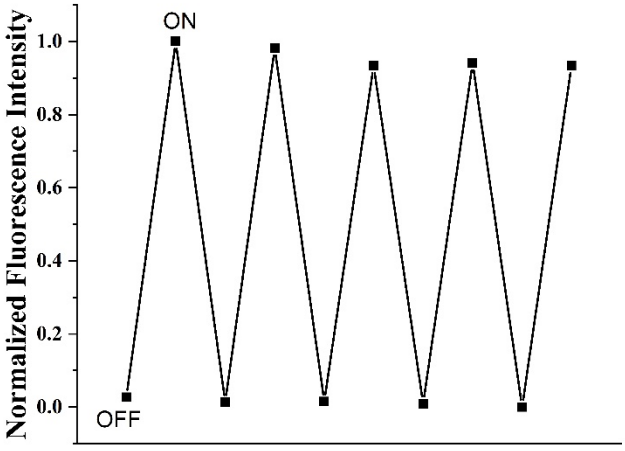

Figure 28. The switch-ON/OFF cycle test of AuNP-ICG-PNIPAM. A total of 5 cycles were conducted.

3.3 Ex vivo CT and USF Imaging

To test if AuNP has enough CT contrast to tissue, the AuNP solution was placed in a 1.5 mL centrifuge tube and CT imaging was conducted with porcine tissue. As shown in Figure 29a, as the CT intensity threshold increased, we could barely identify the porcine tissue. At the same time, we were still able to visualize the AuNP solution. The average gray-scale intensity was evaluated based on the third image in Figure 29a using ImageJ. Porcine tissue had an average gray-scale intensity of 2.34 ± 9.99 and AuNP had an average gray-scale intensity of 183.67 ± 45.25. Furthermore, similar experiments were conducted with AuNP-ICG-PNIPAM. After filling one silicone tube with water (labeled in blue dash line) and the other one with AuNP-ICG-PNIPAM nanogel (labeled in green dash line), both were embedded inside porcine tissue (Figure 29b). CT imaging was used to see if the AuNP-ICG-PNIPAM nanogel contrasted with the tissue. After increasing the CT image threshold, we can barely see the porcine tissue. Meanwhile, the shape of the silicone tube can be visualized. The tube filled with water shows as hollow, and the silicone tube filled with AuNP-ICG-PNIPAM shows as solid in the middle. The side view of the CT image shown in Figure 29c1 and c2 further confirmed that the tube filled with water was hollow in the middle, while the tube filled with AuNP-ICG-PNIPAM nanogel was solid. Figure 29d shows the dimension of the porcine tissue with a thickness of 1.5 cm. Two silicone tubes were embedded in the center of the tissue during both CT and USF imaging. Figure 29e shows the dimensions of the silicone tube with a length of 1.1 cm and an outer diameter of

0.165 cm. A 2-D USF imaging scan of the silicone tube filled with AuNP-ICG-PNIPAM was shown in Figure 29f. The dash line outlined the size of the silicone tube, and we can clearly see the shape of the tube in the USF image.

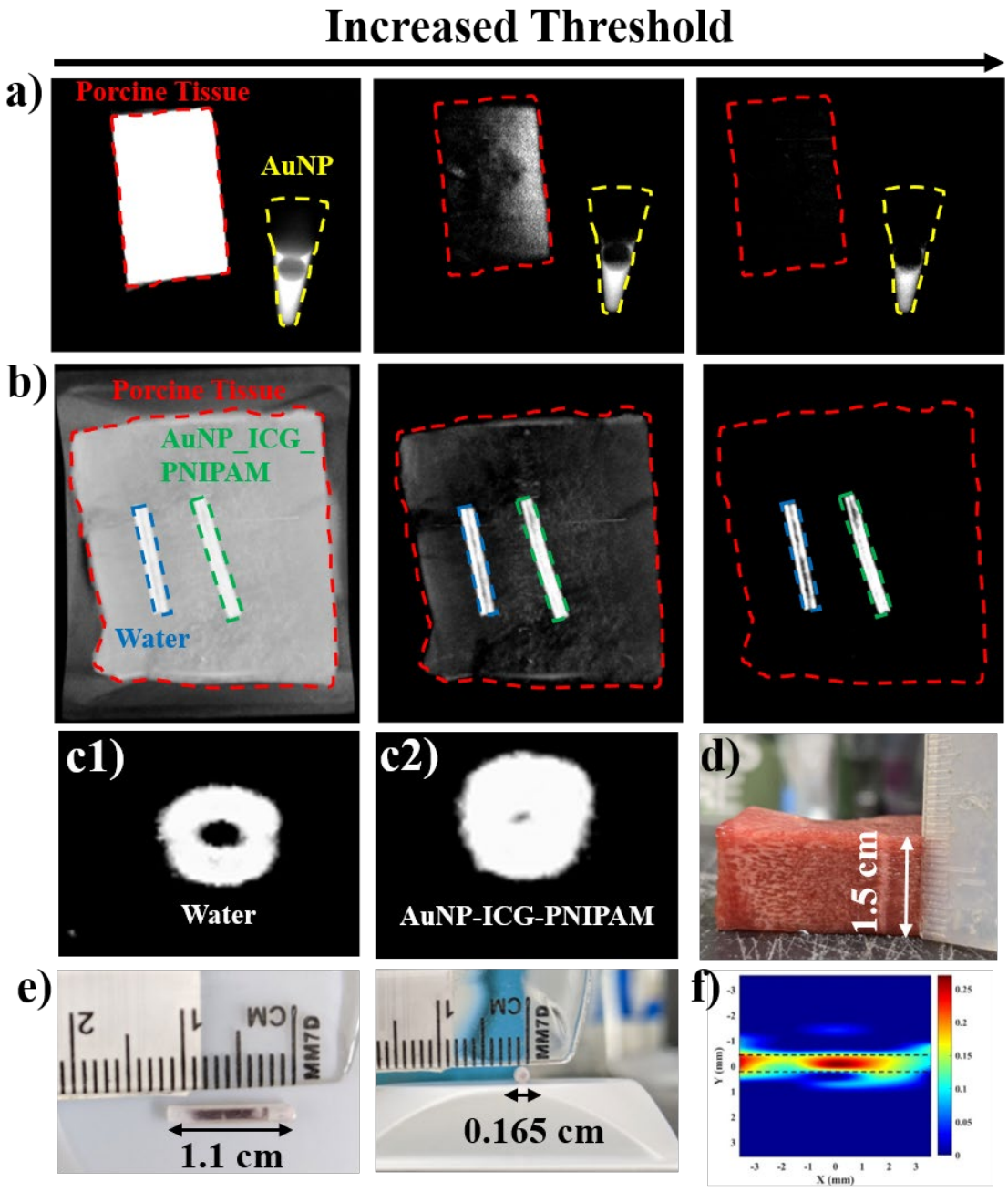

Figure 29. *Ex vivo* of both CT and USF imaging. a) CT imaging of porcine tissue (left) and a centrifuge tube containing AuNP solution (right). The image threshold was increased

from left to right to remove background noise and show CT contrast between tissue and AuNP. A red dash line outlined the shape of porcine tissue, and a yellow dash line outlined the shape of the 1.5 mL centrifuge tube. b) a silicone tube filled with water (labeled in blue dash line) and a silicone tube filled with AuNP-ICG-PNIPAM nanogel (labeled in green dash line) was embedded in porcine tissue (outlined in red dash line). The image threshold was increased from left to right to remove background noise and show CT contrast between tissue and AuNP-ICG-PNIPAM nanogel. The side view of the CT image sides for c1) silicone tube filled with water and c2) silicone tube filled with AuNP-ICG-PNIPAM nanogel were shown. d) image of porcine tissue with a thickness of 1.5 cm. e) the dimension of the silicone tube with a length of 1.1 cm and outer diameter of 0.165 cm. f) 2-D USF imaging scan of the silicone tube, which was filled with AuNP-ICG-PNIPAM nanogel and embedded in the porcine tissue.

3.4 In vivo CT and USF Imaging

Both *in vivo* CT imaging and USF imaging results were shown in Figure 30. A 3-D USF image was shown in Figure 30a1, which had a dimension of 8.128 mm × 8.128 mm × 6.350 mm in the X, Y, and Z directions, respectively. The imaging step size was 1.016 mm in the X and Y directions, and 1.270 mm in the Z direction. The volume of the USF image was 50.10 mm^3. The 3-D CT scan was recorded in Figure 30a2. The CT image had the same dimension and step size as the USF image. The total volume of the CT image was 103.63 mm^3. Figure 30b1 shows the image of a BALB/c mouse with a half-shaved body. The blue dot on the thigh represented the local injection site. A 3-D co-registration image of USF and CT images is shown in Figure 30b2. The USF image, CT image, and

overlapped USF and CT were represented in green, blue, and red, respectively. The overlapped volume was 31.25 mm^3, which meant 62.38 % of the USF image volume was overlaid with the CT image. The sliced co-registration images were shown in Figure 30c with various depths of 1.434, 2.390, 3.346, 4.302, and 5.258 mm. The USF, CT, overlapped, and background were labeled in green, blue, red, and gray, respectively.

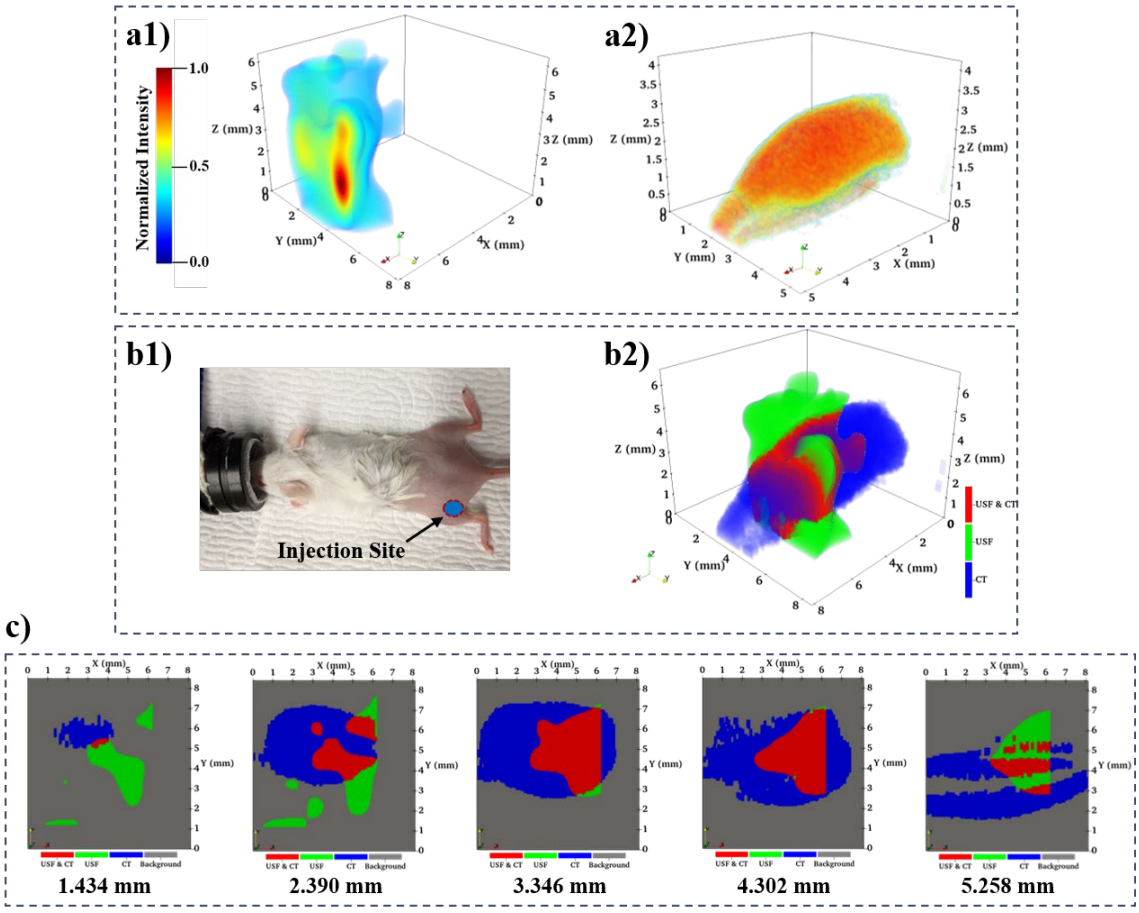

Figure 30. *In vivo* USF and CT imaging. The *in vivo* 3-D a1) USF image and a2) CT image. The intensity was normalized and represented in the color code. b1) The photo of a BALB/c mouse with half-shaved body. The blue dot represented the location where the local injection was conducted. b2) A 3-D co-registration of USF image (represented in green) and CT image (represented in blue). The overlap between the two imaging modalities was

shown in red. c) The X-Y plane sliced co-registration images at depth of 1.434, 2.390, 3.346, 4.302, and 5.258 mm. Number of replicates n = 3.

4. Discussion

4.1 AuNP-ICG-PNIPAM Synthesis Methods

Different approaches were conducted to encapsulate or attach AuNPs to PNIPAM nanogel. First, a seed method by synthesizing the gold nanoparticle first and then growing the polymer on the surface of AuNP was conducted, and the resulted AuNP-PNIPAM apparatus had single AuNPs per nanogel and uniform size distribution [74–77]. The second approach was to synthesize PNIPAM nanogel first and then graft PNIPAM nanogel onto the AuNPs surface during AuNP synthesis via thiol group [78–80]. The above-mentioned methods synthesized a single AuNP encapsulated PNIPAM nanogel. This work described a synthesis method that not only encapsulated ICG dyes but also entrapped multiple AuNPs in a single PNIPAM nanogel. This is desired since we can conduct dual modality imaging using ICG dye for USF and AuNPs for CT.

4.2 Physical Property of AuNP and AuNP-ICG-PNIPAM

The synthesized AuNP showed to have a homogenous size distribution based on the DLS and TEM results with a polydispersity index of 0.147 ± 0.026. As reported in the literature, the size and concentration of AuNP has effects on the CT attenuation [71,81]. Smaller-sized AuNP tends to have a higher CT attenuation compared to larger size AuNP in the same concentration. Also, higher concentration of AuNP leads to higher CT attenuation for same-sized AuNP. Therefore, this work synthesized AuNPs with a size of 24.2 ± 0.2 nm

and later concentrating AuNP-ICG-PNIPAM was conducted to increase the concentration of AuNP. Concentrated AuNP solution was used to synthesize the AuNP-ICG-PNIPAM to increase the quantity of AuNP encapsulated per PNIPAM nanogel. Results showed that The AuNP-ICG-PNIPAM synthesized with concentrated AuNP solution had a higher AuNP quantity encapsulated in the nanogel (Appendix B). As shown in Figure 27b1, after encapsulating AuNPs, the nanogel still remained the desired thermo-responsiveness for USF imaging (i.e. reducing size and increasing fluorescence intensity as temperature increased). In addition, the size of the nanogel was inversely related to the emitted fluorescence intensity. According to the absorption spectra, AuNP had an absorption peak at 520 nm, which was consistent with the literature [82], and ICG-PNIPAM had an absorption at 770 nm, which was also consistent with a previously published article [73]. After encapsulating AuNP into ICG-PNIPAM, the synthesized AuNP-ICG-PNIPAM was shown to have two absorption peaks at both 520 and 770 nm. The emission spectrum of AuNP-ICG-PNIPAM was also similar to the previously published emission spectrum of ICG-PNIPAM nanogel [73], which indicated that AuNP did affect the emission spectrum of nanogel. Additional switch-ON/OFF tests confirmed that the AuNP-ICG-PNIPAM nanogel was stable enough for repeated switch-ON/OFF, which was advantageous for imaging applications.

4.3 Ex vivo and in vivo Dual Modality Imaging: CT and USF

The *ex vivo* CT imaging of the AuNP solution confirmed that synthesized AuNP had strong CT attenuation and had CT contrast to the porcine tissue. This indicated that after injecting AuNP solution into the body, we would be able to identify the AuNPs. The CT imaging of

AuNP-ICG-PNIPAM further confirmed that after encapsulating AuNP into nanogel, the synthesized nanogel had enough CT contrast to the porcine and could be used for *in vivo* imaging. The comparison between a tube filled with water and a tube filled with AuNP-ICG-PNIPAM further confirmed that the AuNP-ICG-PNIPAM inside the tube had CT attenuation. In addition, we successfully conducted USF imaging with the AuNP-ICG-PNIPAM tube model and proved that AuNP-ICG-PNIPAM can be used for CT and USF dual modality imaging.

The *in vivo* CT and USF imaging were conducted successfully via a local intramuscular injection, and 3-D CT and USF images were constructed for comparison. As shown in Figure 30b2, after co-registering the CT image with the USF image, there was overlap between the two imaging modalities, while USF tended to have a spread along the axial direction and CT tended to have a spread along the lateral direction. It is known that USF imaging has a non-ideal axial imaging resolution due to the inherent nonuniform shape of the ultrasound focus. The large spatial spread of CT image might be caused by the low CT attenuation intensity of the AuNP-ICG-PNIPAM nanogel. This issue can be improved by further increasing the concentration of AuNP solution during nanogel synthesis.

4.4 Potential Improvements and Future Applications

Although we have proved that AuNP-ICG-PNIPAM can be used for CT and USF dual modality imaging, several improvements can be implemented to improve the image quality in the future. First, although AuNP-ICG-PNIPAM showed outstanding CT attenuation intensity compared to tissue, a stronger CT attenuation was desired so that we could easily

separate contrast agents from soft and hard tissues. It is known that a higher concentration of AuNP results in a higher CT attenuation intensity. Therefore, a higher concentration of AuNP solution can be used during nanogel synthesis. As we can see from the TEM image, each nanogel still had plenty of space for additional AuNPs. Furthermore, AuNPs can be attached to the monomer first via chemical linkers and then synthesized to form the nanogel. In this way, the quantity of encapsulated AuNPs can be dramatically increased to increase the CT attenuation. Second, the viscosity of AuNP-ICG-PNIPAM was high according to visual observation. The viscosity issue can be simply solved by diluting the AuNP-ICG-PNIPAM nanogel before utilizing it. However, this requires a high concentration of AuNPs in each nanogel to ensure enough CT attenuation after dilution.

Future applications of AuNP-ICG-PNIPAM nanogel include biomarkers and targeted *in vivo* dual modality imaging. As shown in the tube model, AuNP-ICG-PNIPAM nanogel can be sealed within a carrier and implanted into the body as a biomarker. Both CT and USF imaging can be conducted to track the seed. Further, *in vivo* dual modality imaging can be conducted in desired organs or tumors via passive targeting and accumulating.

5. Conclusion

This study has formulated a novel AuNP-ICG-PNIPAM nanogel structure for CT and USF dual modality imaging. The synthesized AuNPs were evenly distributed with a size of 24.2 ± 0.2 nm. After encapsulating AuNPs into PNIPAM nanogel, the thermal-responsive feature and emission peaks were not affected and showed two emission peaks at 604 nm and 800 nm. As the temperature increased from 30 ˚C to 46 ˚C, the hydrodynamic size of

AuNP-ICG-PNIPAM decreased from 122.5 ± 20.8 nm to 51.7 ± 2.6 nm. Furthermore, the stability of the AuNP-ICG-PNIPAM was confirmed with a 5-cycle switch-ON/OFF test. The AuNPs had stronger CT attenuation compared to the CT attenuation of porcine tissue, and the AuNP-ICG-PNIPAM nanogel also showed a CT contrast to the porcine tissue. In addition, TEM images confirmed that increasing the concentration of AuNP solution during nanogel synthesis led to an increased quantity of AuNPs inside a single nanogel. The *in vivo* USF and CT dual modality imaging was successfully conducted on the thigh of mice, and 3-D USF and CT images were constructed. A co-registration of USF and CT images was conducted, and 62.38 % volume of the USF image was overlapped with the CT image. Future applications of the AuNP-ICG-PNIPAM nanogel led to potential biomarkers and *in vivo* organ/tumor targeted dual modality imaging. In addition, this nanogel was not only the first contrast agent apparatus designed for CT and USF dual modality imaging, but also showed the potential of encapsulating various ingredients in the PNIPAM nanogel and was used for various applications such as multi-color imaging, multi-modal imaging, and imaging guided drug delivery.

Chapter 6

Conclusions and Future Work

This study advanced the USF contrast agents via improving the existing ICG-PNIPAM nanogel, developing novel liposomal microparticles and nanoparticles, and exploring dual-modality imaging using CT and USF imaging. First, we controlled the size of the ICG-PNIPAM nanogel by adjusting the quantity of SDS. We conducted characterizations, such as fluorescence profile, stability, spectra, and size. Results showed that size had minimal effects on stability and spectra, but various-sized ICG-PNIPAM nanogels had different fluorescence profiles. In addition, we applied different-sized ICG-PNIPAM nanogels for *in vivo* USF imaging and showed accumulation in either the spleen for the larger-sized nanogel or the liver for the smaller-sized nanogel. ICG-loaded liposomal microparticles were first formulated and characterized with a narrower fully switched-ON temperature range, an NIR emission peak at 836 nm, and excellent biocompatibility for USF imaging. We demonstrated the capability for both *ex vivo* and *in vivo* USF imaging. Furthermore, we accomplished surface decoration with PEGylated chains and folate targeting groups with nanometer-sized liposomes. We evaluated the potential to use liposome nanoparticles for USF-guided and ultrasound-assisted release. Last, we synthesized AuNP-ICG-PNIPAM nanogels and conducted dual-modality imaging with CT and USF. The results showed that AuNPs had high CT contrast to tissue and *in vivo* CT/USF imaging with AuNP-ICG-PNIPAM nanogel was conducted successfully.

Currently, only ICG has been loaded into the PNIPAM. Nanogel loaded with dyes can be used for multicolor imaging to identify targets via multi-colors. Liposomes, one of the most

promising biocompatible particles for *in vivo* applications, has great potential for tumor-targeted USF imaging. Although there is still a challenge in stability during USF imaging with liposomes, membrane composition modifications, such as adding different lipids and optimizing lipid ratios, and structure changes, such as using lipid nanoparticles instead of liposomes and core/shell structure liposomes, can be done to overcome this issue. We suspect that biological factors such as proteins might contribute to the instability of the liposomes. Therefore, mixing liposome with plasma is an option to test the effect of proteins on liposomes. In addition, liposome might be a great candidate for a USF imaging-guided and ultrasound-assisted drug delivery carrier. The demonstration of the dual-modality imaging capability of AuNP-ICG-PNIPAM nanogel showed great potential to combine USF imaging with other imaging modalities. There is a complementary relationship between each modality for disease diagnosis, lesion tracking, and molecular imaging studies. Further depth-study on CT modality can be conducted to learn CT imaging depth limitation.

In conclusion, we strongly believe that contrast agents play a critical role in advancing USF imaging and that USF imaging has great potential to be used for centimeters-deep tissue imaging to overcome the tissue-scattering challenge in fluorescence imaging. Potential USF imaging guided drug delivery systems and multi-modality imaging can be achieved with the help of innovative contrast agents in the future.

Appendix A – Cell Culture

1. Medium Preparation

The DMEM medium was used to culture cell lines of BxPC-3, U87, and 3T3 fibroblast. 1 vol. % penicillin-streptomycin antibiotic (ATCC, USA) was added into the medium and the prepared DMEM stock medium was stored at 4 ˚C. Before using the medium for cell culture, 10 vol. % fetal bovine serum (FBS) was added into the stock medium. The ready-to-use medium was stored at 4 ˚C.

2. Medium Change and Cell Passage

The cell culture was conducted in a T-75 flask (Thermal Scientific, USA). First, medium was removed from the flask and 3 mL PBS (pH 7.4) was added into the flask to wash the cell with gentle swirling. For medium change, PBS was removed, and new cell medium (8 mL) was added into the flask. For cell passage, after removing PBS, 3 mL trypsin (ATTC, USA) was added into the flask. The flask was placed in an incubator for 3 minutes or until the cell detached. 3 mL medium was then added into the flask to dilute the trypsin. Cells were then transferred into a 15 mL centrifuge tube and centrifuged for 5 minutes at 200 xg. At the same time, fresh medium was dispersed into new T-75 flasks. After centrifugation, the supernatant was removed, and the cell pellet was resuspended in 1mL medium. Appropriate volume of resuspended cells was aliquoted to fresh prepared flasks. Finally, the flask was placed into an incubator. The culture medium was changed every 2 days.

3. Tumor Cell Implantation

The procedure was the same as cell passage until centrifuge. After centrifugation, 1 mL medium was used to suspend the cell pellet. Cell counter (Bio-Rad Laboratories, USA) was used to measure cell concentration and adjust the volume of cell solution to have a 3×10^6 cells/mL cell concentration. Then, the cell solution was transferred to a cryogenic storage vial and transported to the mice facility. Athymic Nude-Foxn1nu mutant mice (6 weeks, female) were used. A 1 mL syringe with 27-gauge needle was used during inoculation. 100 μL cell culture was injected into the thigh of mice subcutaneously.

4. Frozen and Recover Cell

The Procedure was the same as cell passage until centrifuge. After centrifuging, 1 mL solution (90 vol. % medium and 10 vol% dimethyl sulfoxide (DMSO)) was used to resuspend the cell pellet. Then, the cell solution was transferred into a cryogenic storage vial. Next, the vial was placed into a cell freezing box and the cell was frozen at -80 ˚C fridge overnight. In the end, the vial was stored in a liquid nitrogen tank for long-term storage.

To recover cells, the cryogenic storage vial was taken out from the liquid nitrogen tank and placed into an incubator with the temperature set to 37 ˚C for 5 minutes. At the same time, 8 mL medium was added into a T-75 flask. Cell solution was then transferred from the vial to the freshly prepared T-75 flask and incubated at 37 ˚C. The next day, the cell medium needs to be changed.

Appendix B – AuNP-ICG-PNIPAM Synthesized with Different Concentrations of AuNP

Figure 31 shows AuNP-ICG-PNIPAM nanogels synthesized with a 5x concentrated AuNP solution and AuNP-ICG-PNIPAM nanogels synthesized with the original concentration of AuNP solution. The AuNP-ICG-PNIPAM synthesized with a 5x concentrated AuNP solution has a larger quantity of AuNPs loaded into the nanogel compared to that of the AuNP-ICG-PNIPAM synthesized with the original concentration of AuNP solution.

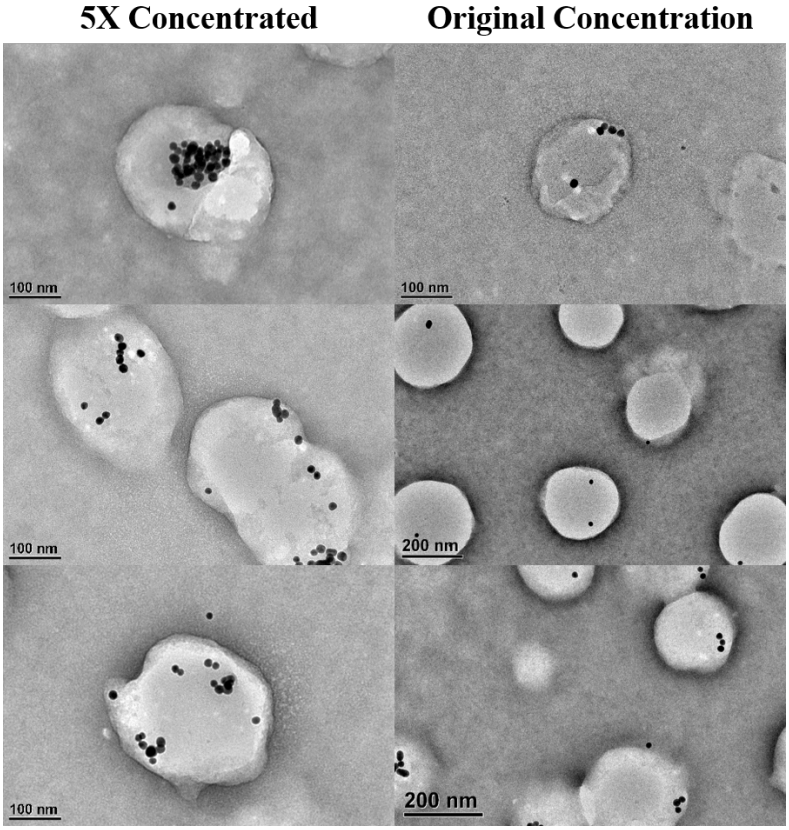

Figure 31. AuNP-ICG-PNIPAM synthesized using 5x concentrated AuNP solution and original concentration of AuNP solution.

Appendix C – Fluorescence Microscopic images and TEM images of ICG-liposomes

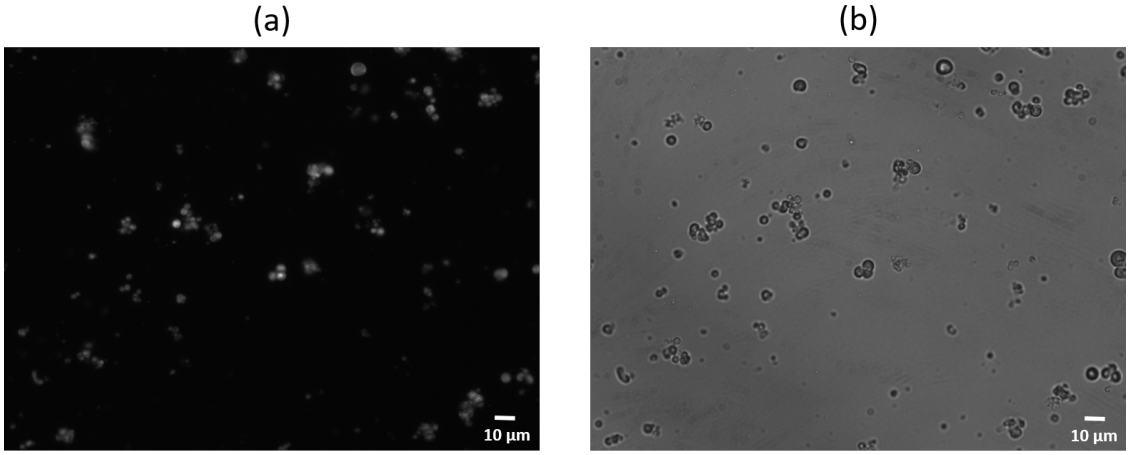

Figure 32. ICG-liposome size measured with the fluorescence microscope. a) Fluorescence image with 3 s exposure time. b) White image with 100 ms exposure time. Both images used a 30x objective lens.

We used a fluorescence microscope to further confirm the size of the ICG-liposome. The sample was diluted and observed under a microscope (Eclipse Ti, Nikon, Japan). Using an exposure time of 100 ms, a white light source image was captured with a 30x objective lens. A fluorescence image was acquired with a 30x objective lens using an exposure time of 3 s. An 808 nm laser (Dragon Lasers, China) with a 785/62-25 nm band-pass filter (Semrock Inc., USA) was used as the light source, and three 830 long-pass emission filters were applied to a CCD camera.

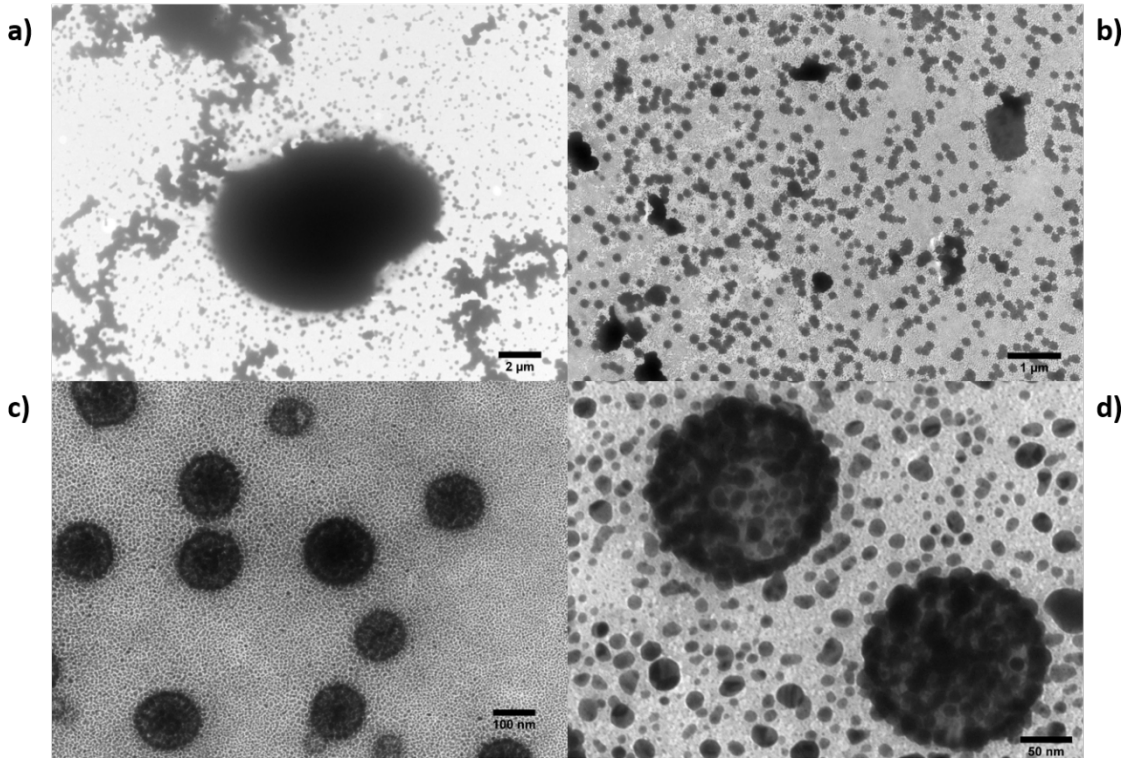

Figure 33. TEM images of the ICG-liposome at different scales a) 2 µm, b) 1 µm, c) 100 nm, and d) 50 nm.

The TEM (H-7500, Hitachi, Japan) was utilized to measure the size of the ICG-liposome. We used a voltage of 40 kV during imaging and prepared the sample with a Formvar film on 200 square mesh copper. The range of the particle size was from nanometers to micrometers. In Figure 33a, the clustered particles had an average size of 10.11 µm. Figure 33b shows a group of particles that had an average size of 254 nm with a standard deviation of 196 nm. Smaller particles were also found with an average size of 136 ± 19.56 nm and 167 ± 2.64 nm in Figure 33c and Figure 33d, respectively.

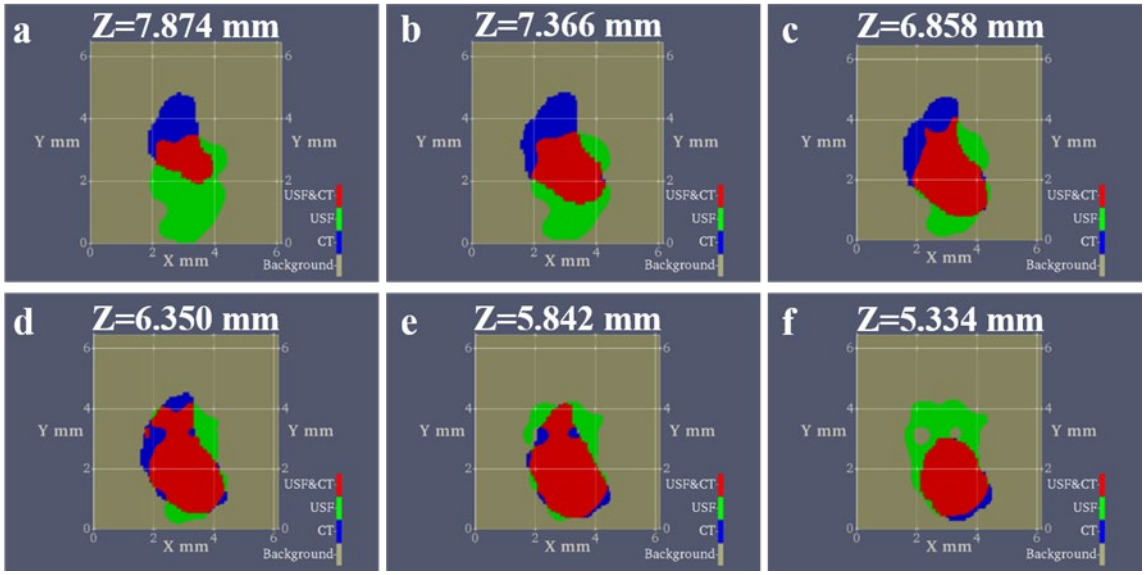

Figure 34. XY-plane slices of tumor model

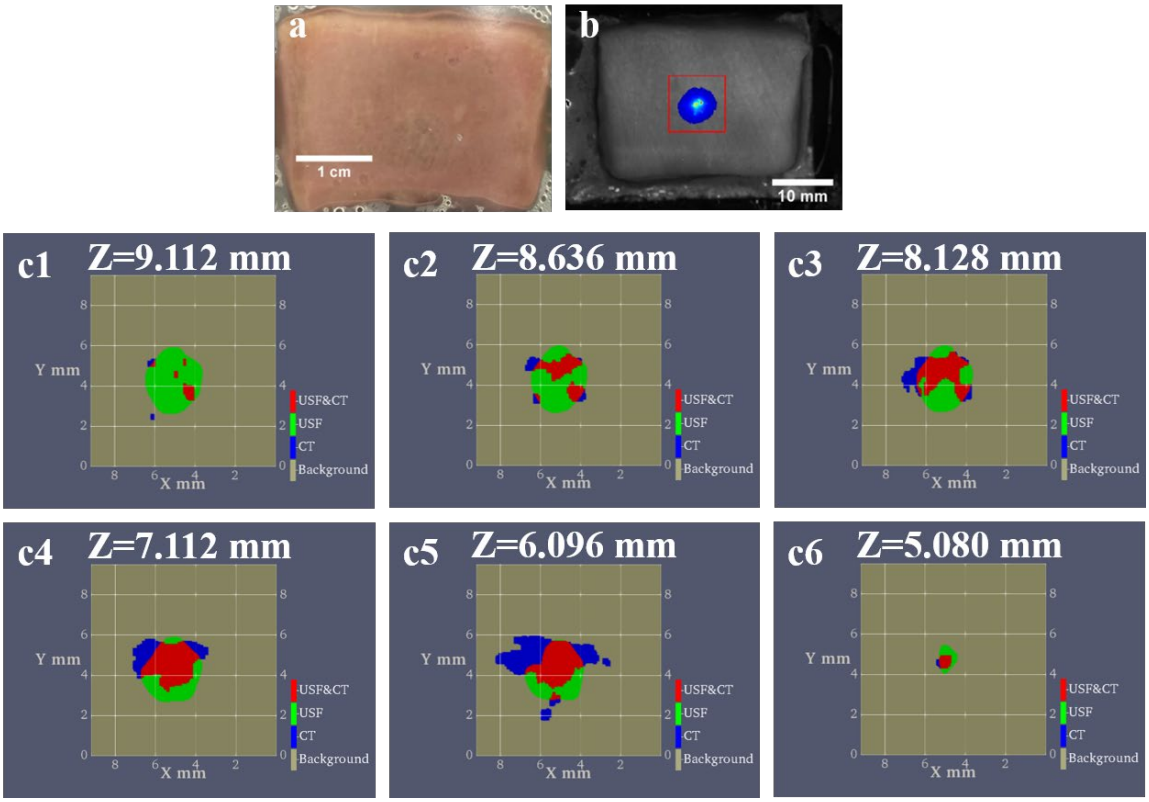

Figure 35. XY-plane slices of porcine muscle tissue model

A fluorescence image was acquired after a local injection of the mixed contrast agent into porcine muscle tissue with a thickness of 1.2 cm (Figure 36b); the red square represents the scanning area on a horizontal plane (XY-plane). The XY-plane of USF and CT overlaid images at different depths sliced from (Figure 13b) are shown in Figure 36c1-6. The green, blue, and red areas represent the USF image, the CT image, and the overlaid image of both the USF and the CT images, respectively. The XY-plane slices of the overlaid USF and CT image (Figure 13e) in the tumor model at various depths are listed in Figure 34a-f.

Appendix E – Test of ICG-liposome Thermo-sensitivity Inside the Liver

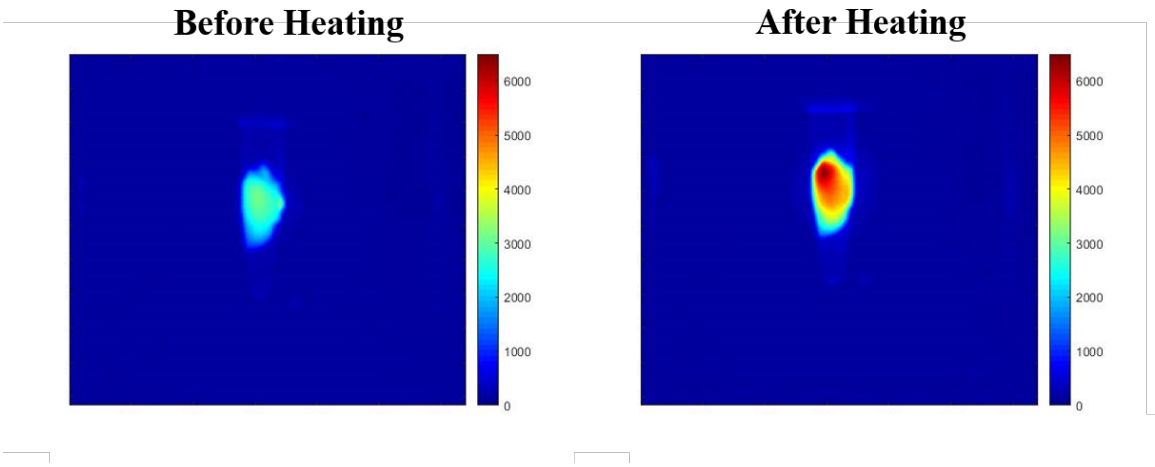

Figure 36. After a 15 min IV injection of the ICG-liposome, a partial right lobe of the liver was dissected out and put in a vial. Fluorescence image was taken under the EM-CCD before and after heating in a water bath.

The thermal sensitivity of the ICG-liposome within the liver was examined. A partial right lobe of the liver was put in a vial and imaged under the EM-CCD camera. Fluorescence images were taken at room temperature (Before Heating) first, then the vial was immersed in hot water to raise the liver temperature above the second LCST, fully switching on the ICG-liposome (After Heating) before the fluorescence image was taken.

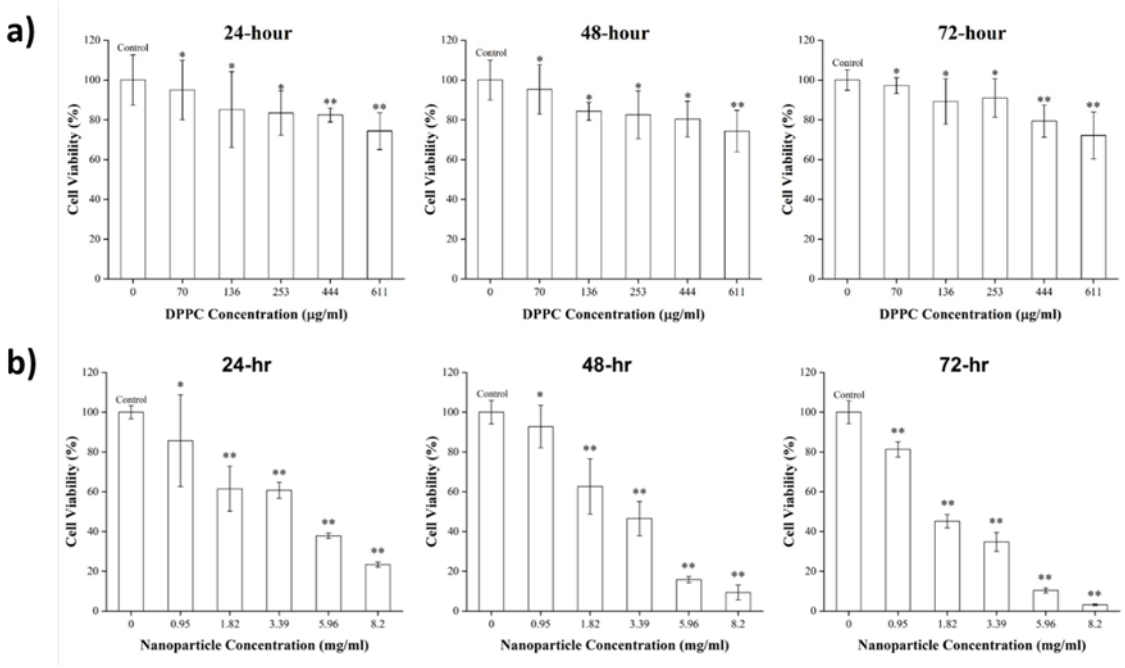

Figure 37. Cell viability test via the MTT method with the 3T3 mouse fibroblast cell line. a) ICG-liposome b) ICG-PNIPAM. The number of replicates was n = 5 (*The p-value is greater than 0.05 with respect to the control group; **the p-value is less than 0.05 with respect to the control group).

The cell viability test of both ICG-liposome and ICG-PNIPAM is shown in Figure 37. The concentrations of contrast agents used for the cell viability test were determined by the final concentration of particles inside the mouse for *in vivo* study. According to Figure 37, the ICG-liposome is safer to be used for *in vivo* studies compared to the ICG-PNIPAM.

References

[1] Wu F, Bhansali SG, Law WC, Bergey EJ, Prasad PN, Morris ME. Fluorescence imaging of the lymph node uptake of proteins in mice after subcutaneous injection: molecular weight dependence. Pharm Res 2012;29:1843–53. https://doi.org/10.1007/s11095-012-0708-6.

[2] Dasgupta A, Biancacci I, Kiessling F, Lammers T. Imaging-assisted anticancer nanotherapy. Theranostics 2020;10:956–67. https://doi.org/10.7150/thno.38288.

[3] Zhang L, Yin T, Li B, Zheng R, Qiu C, Lam KS, et al. Size-Modulable Nanoprobe for High-Performance Ultrasound Imaging and Drug Delivery against Cancer. ACS Nano 2018;12:3449–60. https://doi.org/10.1021/acsnano.8b00076.

[4] Wang P, Fan Y, Lu L, Liu L, Fan L, Zhao M, et al. NIR-II nanoprobes in-vivo assembly to improve image-guided surgery for metastatic ovarian cancer. Nat Commun 2018;9:1–10. https://doi.org/10.1038/s41467-018-05113-8.

[5] van Keulen S, Nishio N, Fakurnejad S, Birkeland A, Martin BA, Lu G, et al. The clinical application of fluorescence-guided surgery in head and neck cancer. J Nucl Med 2019;60:758–63. https://doi.org/10.2967/jnumed.118.222810.

[6] Nakaseko Y, Ishizawa T, Saiura A. Fluorescence-guided surgery for liver tumors. J Surg Oncol 2018;118:324–31. https://doi.org/10.1002/jso.25128.

[7] Hu Z, Fang C, Li B, Zhang Z, Cao C, Cai M, et al. First-in-human liver-tumour surgery guided by multispectral fluorescence imaging in the visible and near-infrared-I/II windows. Nat Biomed Eng 2020;4:259–71. https://doi.org/10.1038/s41551-019-0494-0.

[8] Gao M, Yu F, Lv C, Choo J, Chen L. Fluorescent chemical probes for accurate tumor

diagnosis and targeting therapy. Chem Soc Rev 2017;46:2237–71. https://doi.org/10.1039/c6cs00908e.

[9] Zhang M, Liu J, Wang G. Highly Biocompatible Nanoparticles of Au@Fluorescent Polymers as Novel Contrast Agent for in Vivo Bimodality NIR Fluorescence/CT Imaging. Contrast Media Mol Imaging 2019;2019. https://doi.org/10.1155/2019/8085039.

[10] Wang S, Fan Y, Li D, Sun C, Lei Z, Lu L, et al. Anti-quenching NIR-II molecular fluorophores for in vivo high-contrast imaging and pH sensing. Nat Commun 2019;10. https://doi.org/10.1038/s41467-019-09043-x.

[11] Tang JH, Sun Y, Gong ZL, Li ZY, Zhou Z, Wang H, et al. Temperature-Responsive Fluorescent Organoplatinum(II) Metallacycles. J Am Chem Soc 2018;140:7723–9. https://doi.org/10.1021/jacs.8b04452.

[12] Nakasha K, Fukuhara G. Aggregation-Induced Emission-Based Polymer Materials: Ratiometric Fluorescence Responses Controlled by Hydrostatic Pressure. ACS Appl Polym Mater 2020;2:2303–10. https://doi.org/10.1021/acsapm.0c00272.

[13] Sheng Z, Li Y, Hu D, Min T, Gao D, Ni J-S, et al. Centimeter-Deep NIR-II Fluorescence Imaging with Nontoxic AIE Probes in Nonhuman Primates. Research 2020;2020:1–14. https://doi.org/10.34133/2020/4074593.

[14] Gschwend PM, Niedbalka D, Gerken LRH, Herrmann IK, Pratsinis SE. Simultaneous Nanothermometry and Deep-Tissue Imaging. Adv Sci 2020;7:1–6. https://doi.org/10.1002/advs.202000370.

[15] Chen G, Shen J, Ohulchanskyy TY, Patel NJ, Kutikov A, Li Z, et al. Nanoparticles with E ffi cient Upconversion for High-Contrast Deep Tissue Bioimaging. ACS

Nano 2012:8280–7.

[16] Dang X, Bardhan NM, Qi J, Gu L, Eze NA, Lin CW, et al. Deep-tissue optical imaging of near cellular-sized features. Sci Rep 2019;9:1–12. https://doi.org/10.1038/s41598-019-39502-w.

[17] Cheng B, Bandi V, Wei MY, Pei Y, D'Souza F, Nguyen KT, et al. High-resolution ultrasound-switchable fluorescence imaging in centimeter-deep tissue phantoms with high signal-to-noise ratio and high sensitivity via novel contrast agents. PLoS One 2016;11:1–16. https://doi.org/10.1371/journal.pone.0165963.

[18] Yu S, Wang Z, Yao T, Yuan B. Near-infrared temperature-switchable fluorescence nanoparticles. Quant Imaging Med Surg 2021;11:1010–22. https://doi.org/10.21037/QIMS-20-797.

[19] Pei Y, Wei MY, Cheng B, Liu Y, Xie Z, Nguyen K, et al. High resolution imaging beyond the acoustic diffraction limit in deep tissue via ultrasound-switchable NIR fluorescence. Sci Rep 2014;4:4690. https://doi.org/10.1038/srep04690.

[20] Yu S, Cheng B, Yao T, Xu C, Nguyen KT, Hong Y, et al. New generation ICG-based contrast agents for ultrasound-switchable fluorescence imaging. Sci Rep 2016;6:1–10. https://doi.org/10.1038/srep35942.

[21] Yao T, Yu S, Liu Y, Yuan B. In vivo ultrasound-switchable fluorescence imaging. Sci Rep 2019;9:1–13.

[22] Cooperstein MA, Canavan HE. Assessment of cytotoxicity of (N -isopropyl Assessment of cytotoxicity of (N -isopropyl acrylamide) and Poly (N -isopropyl acrylamide) - coated surfaces. Biointerphases 2013;8:19–21.

[23] Yuan B, Uchiyama S, Liu Y, Nguyen KT, Alexandrakis G. High-resolution imaging

in a deep turbid medium based on an ultrasound-switchable fluorescence technique. Appl Phys Lett 2012;101. https://doi.org/10.1063/1.4737211.

[24] Yu S, Yao T, Liu Y, Yuan B. In vivo ultrasound-switchable fluorescence imaging using a camera-based system. Biomed Opt Express 2020;11:1517. https://doi.org/10.1364/boe.385996.

[25] Danaei M, Dehghankhold M, Ataei S, Hasanzadeh Davarani F, Javanmard R, Dokhani A, et al. Impact of particle size and polydispersity index on the clinical applications of lipidic nanocarrier systems. Pharmaceutics 2018;10:1–17. https://doi.org/10.3390/pharmaceutics10020057.

[26] Andersson M, Maunu SL. Structural Studies of Poly(N-isopropylacrylamide) Microgels: Effect of SDS Surfactant Concentration in the Microgel Synthesis. J Polym Sci B Polym Phys 2006;44:3305–14. https://doi.org/10.1002/polb.

[27] Almarhaby AM, Lees JE, Bugby SL, Alqahtani MS, Jambi LK, McKnight WR, et al. Characterisation of a near-infrared (NIR) fluorescence imaging systems intended for hybrid gamma-NIR fluorescence image guided surgery. J Instrum 2019;14. https://doi.org/10.1088/1748-0221/14/07/P07007.

[28] Dewhirst MW, Viglianti LB, Lora-Michiels M, Hoopes PJ, Hanson M. Thermal Dose Requirement for Tissue Effect: Experimental and Clinical Findings. Proc SPIE Int Soc Opt Eng 2003;37:338–48. https://doi.org/10.1117/12.476637.

[29] Kato Y, Ozawa S, Miyamoto C, Maehata Y, Suzuki A, Maeda T, et al. Acidic extracellular microenvironment and cancer. Cancer Cell Int 2013;13:1–8. https://doi.org/10.1186/1475-2867-13-89.

[30] Acharya S, Sahoo SK. PLGA nanoparticles containing various anticancer agents and

tumour delivery by EPR effect. Adv Drug Deliv Rev 2011;63:170–83. https://doi.org/10.1016/j.addr.2010.10.008.

[31] Zhang Q, Morgan SP, Mather ML. Nanoscale Ultrasound-Switchable FRET-Based Liposomes for Near-Infrared Fluorescence Imaging in Optically Turbid Media. Small 2017;13:1–12. https://doi.org/10.1002/smll.201602895.

[32] Liu Y, Feshitan JA, Wei MY, Borden MA, Yuan B. Ultrasound-modulated fluorescence based on donor-acceptor-labeled microbubbles. J Biomed Opt 2015;20:036012. https://doi.org/10.1117/1.JBO.20.3.

[33] Cheng MHY, Harmatys KM, Charron D, Chen juan, Zheng G. Stable J-aggregation of an aza-BODIPY-lipid in a liposome for optical cancer imaging. Angew Chemie Int Ed 2019. https://doi.org/10.1002/anie.201907754.

[34] Tansi FL, Rüger R, Rabenhold M, Steiniger F, Fahr A, Kaiser WA, et al. Liposomal encapsulation of a near-infrared fluorophore enhances fluorescence quenching and reliable whole body optical imaging upon activation in vivo. Small 2013;9:3659–69. https://doi.org/10.1002/smll.201203211.

[35] Frangioni J V. In vivo near-infrared fluorescence imaging. Curr Opin Chem Biol 2003;7:626–34. https://doi.org/10.1016/j.cbpa.2003.08.007.

[36] Yao T, Liu Y, Ren L, Yuan B. Improving sensitivity and imaging depth of ultrasound-switchable fluorescence via an EMCCD-gain-controlled system and a liposome-based contrast agent. Quant Imaing Med Surg 2020;20:1–12. https://doi.org/10.21037/qims-20-796.

[37] Wadajkar AS, Koppolu B, Rahimi M, Nguyen KT. Cytotoxic evaluation of N-isopropylacrylamide monomers and temperature-sensitive poly(N-

isopropylacrylamide) nanoparticles. J Nanoparticle Res 2009;11:1375–82. https://doi.org/10.1007/s11051-008-9526-5.

[38] Cheng B, Bandi V, Yu S, D'Souza F, Nguyen KT, Hong Y, et al. The mechanisms and biomedical applications of an NIR BODIPY-based switchable fluorescent probe. Int J Mol Sci 2017;18:384. https://doi.org/10.3390/ijms18020384.

[39] Wu D, Chen L, Lee W, Ko G, Yin J, Yoon J. Recent progress in the development of organic dye based near-infrared fluorescence probes for metal ions. Coord Chem Rev 2018;354:74–97. https://doi.org/10.1016/j.ccr.2017.06.011.

[40] Chen H, He W, Low PS, Cheng J-X, Park K, Kim S, et al. Fast release of lipophilic agents from circulating PEG-PDLLA micelles revealed by in vivo Förster resonance energy transfer imaging. Langmuir 2008;24:5213–7. https://doi.org/10.1021/la703570m.

[41] Zhang X, Bloch S, Akers W, Achilefu S. Near-infrared Molecular Probes for In Vivo Imaging. Curr Protoc Cytom 2012;60:12–27. https://doi.org/10.1038/jid.2014.371.

[42] Kimelberg HK. Protein-liposome interactions and their relevance to the structure and function of cell membranes. Mol Cell Biochem 1976;10:171–90. https://doi.org/10.1007/BF01731688.

[43] Logan JW, Moya FR. Animal-derived surfactants for the treatment and prevention of neonatal respiratory distress syndrome: Summary of clinical trials. Ther Clin Risk Manag 2009;5:251–60.

[44] Sheng Z, Hu D, Xue M, He M, Gong P, Cai L. Indocyanine Green Nanoparticles for Theranostic Applications. Nano-Micro Lett 2013;5:145–50.

https://doi.org/10.1007/bf03353743.

[45] Moghimi SM, Hunter AC, Murray JC. Long-Circulating and Target-Specific Nanoparticles : Theory to Practice. Pharmacol Rev 2001;53:283–318.

[46] Longmire M, Choyke PL, Kobayashi H. Clearance properties of nano-sized particles and molecules as imaging agents: considerations and caveats. Nanomedicine 2008;3:703.

[47] Bahmani B, Lytle CY, Walker AM, Gupta S, Vullev VI, Anvari B. Effects of nanoencapsulation and PEGylation on biodistribution of indocyanine green in healthy mice: Quantitative fluorescence imaging and analysis of organs. Int J Nanomedicine 2013;8:1609–20. https://doi.org/10.2147/IJN.S42511.

[48] Kohane DS. Microparticles and nanoparticles for drug delivery. Biotechnol Bioeng 2007;96:203–9. https://doi.org/10.1002/bit.21301.

[49] Liu Y, Yao T, Cai W, Yu S, Hong Y, Nguyen KT, et al. A Biocompatible and Near-Infrared Liposome for In Vivo Ultrasound-Switchable Fluorescence Imaging. Adv Healthc Mater 2020;9:1–10. https://doi.org/10.1002/adhm.201901457.

[50] Du Y, Liang X, Li Y, Sun T, Jin Z, Xue H, et al. Nuclear and Fluorescent Labeled PD-1-Liposome-DOX-64Cu/IRDye800CW Allows Improved Breast Tumor Targeted Imaging and Therapy. Mol Pharm 2017;14:3978–86. https://doi.org/10.1021/acs.molpharmaceut.7b00649.

[51] Belhadj Z, Ying M, Cao X, Hu X, Zhan C, Wei X, et al. Design of Y-shaped targeting material for liposome-based multifunctional glioblastoma-targeted drug delivery. J Control Release 2017;255:132–41. https://doi.org/10.1016/j.jconrel.2017.04.006.

[52] Hossann M, Hirschberger J, Schmidt R, Baumgartner C, Zimmermann K, Baer S, et al. A Heat-Activated Drug-Delivery Platform Based on Phosphatidyl-(oligo)-glycerol Nanocarrier for Effective Cancer Treatment. Adv NanoBiomed Res 2021;2000089:2000089. https://doi.org/10.1002/anbr.202000089.

[53] Barenholz Y. Liposome application: Problems and prospects. Curr Opin Colloid Interface Sci 2001;6:66–77. https://doi.org/10.1016/S1359-0294(00)00090-X.

[54] Ahmed SE, Martins AM, Husseini GA. The use of ultrasound to release chemotherapeutic drugs from micelles and liposomes. J Drug Target 2015;23:16–42. https://doi.org/10.3109/1061186X.2014.954119.

[55] Zylberberg C, Matosevic S. Pharmaceutical liposomal drug delivery: a review of new delivery systems and a look at the regulatory landscape. Drug Deliv 2016;23:3319–29. https://doi.org/10.1080/10717544.2016.1177136.

[56] Awad NS, Paul V, Mahmoud MS, Al Sawaftah NM, Kawak PS, Al Sayah MH, et al. Effect of Pegylation and Targeting Moieties on the Ultrasound-Mediated Drug Release from Liposomes. ACS Biomater Sci Eng 2020;6:48–57. https://doi.org/10.1021/acsbiomaterials.8b01301.

[57] Kono K, Takashima M, Yuba E, Harada A, Hiramatsu Y, Kitagawa H, et al. Multifunctional liposomes having target specificity, temperature-triggered release, and near-infrared fluorescence imaging for tumor-specific chemotherapy. J Control Release 2015;216:69–77. https://doi.org/10.1016/j.jconrel.2015.08.005.

[58] Lu Y, Aimetti AA, Langer R, Gu Z. Bioresponsive materials. Nat Rev Mater 2016;2. https://doi.org/10.1038/natrevmats.2016.75.

[59] Nkanga CI, Bapolisi AM, Okafor NI, Krause RWM. General Perception of

Liposomes: Formation, Manufacturing and Applications. Liposomes Adv. Perspect., IntechOpen; 2019.

[60] Maruyama K. Intracellular targeting delivery of liposomal drugs to solid tumors based on EPR effects. Adv Drug Deliv Rev 2011;63:161–9. https://doi.org/10.1016/j.addr.2010.09.003.

[61] Bachmann MF, Jennings GT. Vaccine delivery: A matter of size, geometry, kinetics and molecular patterns. Nat Rev Immunol 2010;10:787–96. https://doi.org/10.1038/nri2868.

[62] Yoshioka H. Surface modification of haemoglobin-containing liposomes with polyethylene glycol prevents liposome aggregation in blood plasma. Biomaterials 1991;12:861–4. https://doi.org/10.1016/0142-9612(91)90075-L.

[63] Gabizon AA. Liposome circulation time and tumor targeting: implications for cancer chemotherapy. Adv Drug Deliv Rev 1995;16:285–94. https://doi.org/10.1016/0169-409X(95)00030-B.

[64] Maitani Y, Aso Y, Yamada A, Yoshioka S. Effect of sugars on storage stability of lyophilized liposome/DNA complexes with high transfection efficiency. Int J Pharm 2008;356:69–75. https://doi.org/10.1016/j.ijpharm.2007.12.033.

[65] Zhong Y, Ma Z, Wang F, Wang X, Yang Y, Liu Y, et al. In vivo molecular imaging for immunotherapy using ultra-bright near-infrared-IIb rare-earth nanoparticles. Nat Biotechnol 2019;37:1322–31. https://doi.org/10.1038/s41587-019-0262-4.

[66] Blanco-Colino R, Espin-Basany E. Intraoperative use of ICG fluorescence imaging to reduce the risk of anastomotic leakage in colorectal surgery: a systematic review and meta-analysis. Tech Coloproctol 2018;22:15–23.

https://doi.org/10.1007/s10151-017-1731-8.

[67] Baiocchi GL, Diana M, Boni L. Indocyanine green-based fluorescence imaging in visceral and hepatobiliary and pancreatic surgery: State of the art and future directions. World J Gastroenterol 2018;24:2921–30. https://doi.org/10.3748/wjg.v24.i27.2921.

[68] Mahan MM, Doiron AL. Gold Nanoparticles as X-Ray, CT, and Multimodal Imaging Contrast Agents: Formulation, Targeting, and Methodology. J Nanomater 2018;2018. https://doi.org/10.1155/2018/5837276.

[69] Khademi S, Sarkar S, Shakeri-Zadeh A, Attaran N, Kharrazi S, Ay MR, et al. Targeted gold nanoparticles enable molecular CT imaging of head and neck cancer: An in vivo study. Int J Biochem Cell Biol 2019;114:105554. https://doi.org/10.1016/j.biocel.2019.06.002.

[70] Ashton JR, Gottlin EB, Patz EF, West JL, Badea CT. A comparative analysis of EGFR-targeting antibodies for gold nanoparticle CT imaging of lung cancer. PLoS One 2018;13:1–20. https://doi.org/10.1371/journal.pone.0206950.

[71] Dong YC, Hajfathalian M, Maidment PSN, Hsu JC, Naha PC, Si-Mohamed S, et al. Effect of Gold Nanoparticle Size on Their Properties as Contrast Agents for Computed Tomography. Sci Rep 2019;9:1–13. https://doi.org/10.1038/s41598-019-50332-8.

[72] Kimling J, Maier M, Okenve B, Kotaidis V, Ballot H, Plech A. Turkevich method for gold nanoparticle synthesis revisited. J Phys Chem B 2006;110:15700–7. https://doi.org/10.1021/jp061667w.

[73] Liu R, Yao T, Liu Y, Yu S, Ren L, Hong Y, et al. Temperature-sensitive polymeric

nanogels encapsulating with β-cyclodextrin and ICG complex for high-resolution deep-tissue ultrasound-switchable fluorescence imaging. Nano Res 2020;13:1–11. https://doi.org/10.1007/s12274-020-2752-6.

[74] Yang Y, Wang X, Liao G, Liu X, Chen Q, Li H, et al. iRGD-decorated red shift emissive carbon nanodots for tumor targeting fluorescence imaging. J Colloid Interface Sci 2018;509:515–21. https://doi.org/10.1016/j.jcis.2017.09.007.

[75] Vogel N, Fernández-López C, Pérez-Juste J, Liz-Marzán LM, Landfester K, Weiss CK. Max Planck Institute for Polymer Research, Ackermannweg 10, 55128 Mainz, Germany Departamento de Química Física, Universidade de Vigo, 36310 Vigo, Spain. Langmuir 2012;28:8985–93.

[76] Feng C, Shen Z, Li Y, Gu L, Zhang Y, Lu G, et al. PNIPAM-b-(PEA-g-PDMAEA) double-hydrophilic graft copolymer: Synthesis and its application for preparation of gold nanoparticles in aqueous media. J Polym Sci Part A Polym Chem 2009;47:1811–24. https://doi.org/10.1002/pola.23282.

[77] Carregal-Romero S, Buurma NJ, Pérez-Juste J, Liz-Marzán LM, Hervés P. Catalysis by Au@pNIPAM nanocomposites: Effect of the cross-linking density. Chem Mater 2010;22:3051–9. https://doi.org/10.1021/cm903261b.

[78] Shan J, Chen J, Nuopponen M, Tenhu H. Two phase transitions of poly(N-isopropylacrylamide) brushes bound to gold nanoparticles. Langmuir 2004;20:4671–6. https://doi.org/10.1021/la0363938.

[79] Jones ST, Walsh-Korb Z, Barrow SJ, Henderson SL, Del Barrio J, Scherman OA. The Importance of Excess Poly(N-isopropylacrylamide) for the Aggregation of Poly(N-isopropylacrylamide)-Coated Gold Nanoparticles. ACS Nano

2016;10:3158–65. https://doi.org/10.1021/acsnano.5b04083.

[80] Budhlall BM, Marquez M, Velev OD. Microwave, photo- And thermally responsive PNIPAm-gold nanoparticle microgels. Langmuir 2008;24:11959–66. https://doi.org/10.1021/la8019556.

[81] Chenjie X, Tung GA, Shouheng S. Size and concentration effect of gold nanoparticles on X-ray attenuation as measured on computed tomography. Chem Mater 2008;20:4167–9. https://doi.org/10.1021/cm8008418.

[82] He YQ, Liu SP, Kong L, Liu ZF. A study on the sizes and concentrations of gold nanoparticles by spectra of absorption, resonance Rayleigh scattering and resonance non-linear scattering. Spectrochim Acta - Part A Mol Biomol Spectrosc 2005;61:2861–6. https://doi.org/10.1016/j.saa.2004.10.035.

Figures 1, 2, 18, and 26 were created with BioRender.com.

Biographical Information

Yang Liu received his Bachelor of Science degree in Environmental Studies at the University of Nebraska-Lincoln in 2012. He continued his study in Environmental Engineering with a Master of Science degree at the University of Cincinnati under the supervision of Dr. Mingming Lu, where he focused on novel *in situ* biodiesel production from waste coffee grounds from 2012 to 2015. Then, he joined Virginia Commonwealth University to study for his second Master of Science degree in Chemical and Life Science major in Dr. Stephen Fong's lab from 2015 to 2017. He investigated the construction of photoelectrochemical cells with a BBY membrane and the production of enzymes using a plasmid introduced into *E. coli* bacteria.

He joined Dr. Baohong Yuan's research group in 2017 and majored in Biomedical Engineering at the joint program of the University of Texas at Arlington and the University of Texas Southwestern Medical Center. His research is mainly focused on improving existing contrast agents and formulating novel contrast agents for ultrasound-switchable fluorescence imaging. He also explored potential *in vivo* dual modality imaging using CT and USF. His expertise includes polymeric and liposomal nanoparticle formulation and characterization, ultrasound and fluorescence imaging, and cell culture and animal models. He has co-authored eight peer-reviewed journal articles, served as a reviewer for three journals, and filed one patent. Based on his research work, Yang was awarded the Greater Cincinnati Earth Coalition Student Environmental Award in 2014 and the Potvin Award for Outstanding Biomedical Engineering Student in 2020.